Remote Sensing of Martian Sedimentary Deposits and Lunar Pyroclastic Deposits

by

Kristen Alicia Bennett

A Dissertation Presented in Partial Fulfillment
of the Requirements for the Degree
Doctor of Philosophy

Approved July 2016 by the
Graduate Supervisory Committee:

James Bell, Chair
Amanda Clarke
Kelin Whipple
Philip Christensen
Mark Robinson

ARIZONA STATE UNIVERSITY

August 2016

ABSTRACT

On Mars, sedimentary deposits reveal a complex history of water- and wind-related geologic processes. Central mounds – kilometer-scale stacks of sediment located within craters – occur across Mars, but the specific processes responsible for mound formation and subsequent modification are still uncertain. A survey of central mounds within large craters was conducted. Mound locations, mound offsets within their host craters, and relative mound heights were used to address various mound formation hypotheses. The results suggest that mound sediments once filled their host craters and were later eroded into the features observed today. Mounds offsets from the center of their host crater imply that wind caused the erosion of central mounds. An in depth study of a single central mound (Mt. Sharp within Gale crater) was also conducted. Thermal Emission Imaging System Visible Imaging Subsystem (THEMIS-VIS) mosaics in grayscale and false color were used to characterize the morphology and color variations in and around Gale crater. One result of this study is that dunes within Gale crater vary in false color composites from blue to purple, and that these color differences may be due to changes in dust cover, grain size, and/or composition. To further investigate dune fields on Mars, albedo variations at eight dune fields were studied based on the hypothesis that a dune's ripple migration rate is correlated to its albedo. This study concluded that a dune's minimum albedo does not have a simple correlation with its ripple migration rate. Instead, dust devils remove dust on slow-moving and immobile dunes, whereas saltating sand caused by strong winds removes dust on faster-moving dunes.

On the Moon, explosive volcanic deposits within Oppenheimer crater that were emplaced ballistically were investigated. Lunar Reconnaissance Orbiter (LRO) Diviner Radiometer mid-infrared data, LRO Camera images, and Chandrayaan-1 orbiter Moon Mineralogy Mapper near-infrared spectra were used to test the hypothesis that the pyroclastic deposits in Oppenheimer crater were emplaced via Vulcanian activity by constraining their composition and mineralogy. The mineralogy and iron-content of the pyroclastic deposits vary significantly (including examples of potentially very high iron compositions), which indicates variability in eruption style. These results suggest that localized lunar pyroclastic deposits may have a more complex origin and mode of emplacement than previously thought.

ACKNOWLEDGMENTS

I have so much gratitude for my advisor, Jim Bell, and my dissertation committee for guiding me through this process. I would also like to thank SESE, from the students to the administration to the faculty. This department works hard to be the best it can be, and I have grown as a person during my time here as a result of the many collaborations and insightful discussions I have had with wonderful people. Thanks to all of the colleagues and friends who supported me and kept me grounded over the years, including Lauren Edgar, Kelsey Young, Allie Rutledge, Briony Horgan, Nathan Williams, Becky Smith, Andy Ryan, Michael Veto, and everyone involved with Caliente. Many thanks to Michael for the STEM conversations, to Michelle for being the best, to my father for his unwavering support, and especially to my mother (who beat me to a doctorate degree by only a few years) for the inspiration. Finally, I would like to thank my fiancé, Brett, who has been with me for every step of my journey through graduate school. My time here, and my life, are better for having met you.

TABLE OF CONTENTS

CHAPTER Page

LIST OF TABLES

LIST OF FIGURES

Figure Page

CHAPTER 1

INTRODUCTION

Remote sensing of planetary surfaces using orbiters is one of the primary ways to study other planetary bodies. Robotic planetary exploration began with lunar missions in the late 1950s. The first planetary missions were either flybys or hard impactors. Since then, planetary missions have become increasingly more sophisticated: spacecraft have orbited and soft landed on planets, moons, asteroids, and comets and rovers have been sent to both the Moon and Mars. After New Horizons reached Pluto in 2015, every major class of planetary body in the solar system has been visited by a planetary mission. The past 20 years have seen a golden era of planetary exploration. Six different space agencies have sent flyby missions, orbiters, landers or rovers to the Moon. The United States alone has successfully sent six orbiters, four rovers, and four landers to Mars. With the wealth of data being obtained, researchers have been able to address key questions in the field of planetary science. This dissertation utilizes orbital and landed data to investigate sedimentary materials on Mars (Chapters 2-4) and the Moon (Chapter 5). On Mars, I investigate ancient sedimentary deposits in the form of central mounds within craters and contemporary sedimentary materials in the form of sand dunes. On the Moon I investigate volcaniclastic deposits that were a result of explosive lunar volcanism.

Currently, Mars is a cold, dry planet. The main geologic force on Mars today is wind, with sand dunes being one of the most observably changing features on the surface (Bridges *et al.*, 2010). However, ancient Mars was surely wetter, as evidenced by the many fluvial and lacustrine features observed in the southern highlands (e.g. Carr &

Clow, 1981; Craddock & Maxwell, 1993; Malin & Edgett, 2000; Jakosky & Phillips, 2001). Many questions still remain: Was ancient Mars warm and wet or cold and wet? When and how long did the wet period on Mars last? How wet did it really get? What were the primary geologic forces acting during this time? All of these questions have implications for the search for past life on Mars. A warm and wet environment that persisted for an extended period of time greatly increases the potential for life, and certain geologic processes are more conducive to fostering and preserving evidence of life.

One way to answer these questions is to investigate the ancient rock record. In the past 20 years of space exploration we have come to realize that Mars contains many examples of ancient sedimentary deposits (*e.g.* Malin & Edgett, 2000). These deposits exist as layers in the bottoms of basins, as deltas emerging from the ends of channels, and a variety of mantling layers of materials. In Chapters 2 and 3 I investigate a subset of martian sedimentary deposits: central mounds. Central mounds, which are kilometer-scale stacks of sediment located within craters, occur across Mars but the specific processes responsible for mound formation and subsequent modification are still uncertain (Malin & Edgett, 2000). Process-specific models estimate formation times that range from tens to hundreds of Myr (Fergason & Christensen, 2008; Andrews-Hanna *et al.*, 2010), and crater counting at one mound implies that it formed during the Noachian-Hesperian boundary (Thomson *et al*., 2011). Since these interior crater deposits occur globally, mound formation mechanisms could be representative of a global process that was active throughout an extended period of early martian history. The deposits are hypothesized to have been created by either subaerial or subaqueous processes through

one of two general formation mechanisms. The first (prevailing) hypothesis suggests that after their host craters were formed, sediment filled the entire crater and was later eroded into the morphologies we observe today (*e.g.*, Malin & Edgett, 2000). Alternatively, a competing hypothesis suggests that the mounds formed in place and the sediment never extended to the crater walls (*e.g.*, Kite *et al.*, 2013).

Gale crater, the landing site for the Mars Science Laboratory (MSL) *Curiosity* rover and the focus of Chapter 3, is an example of a crater containing a central mound. Gale's mound, formally known as Aeolis Mons but informally referred to as Mt. Sharp, rises ~ 5 km above the crater floor and contains layered sediments that could preserve a record of early martian climate and habitability (*e.g.*, Anderson & Bell, 2010; Milliken *et al.*, 2010; Thomson *et al*., 2011). *Curiosity* is currently investigating the basal units of that central mound and has already provided evidence that liquid water was present on the crater floor at some time in Gale crater's history, and that the environment at that time would have been habitable (*e.g.,* Grotzinger *et al.*, 2013; Williams *et al.*, 2013). In order to place new discoveries at Gale crater into a global context, however, it is necessary to understand how Mt. Sharp relates to the entire population of central mounds.

In **Chapter 2** I conducted a survey of central mounds within large (> 25 km diameter) impact craters on Mars. I use mound locations, mound offsets within their host craters, and relative mound heights to address and extend various mound formation hypotheses. The results of this survey support the hypothesis that mound sediments once filled their host craters and were later eroded into the features observed today. The majority of mounds are located near the boundaries of previously identified large-scale sedimentary deposits. I discuss the implications of the hypothesis that central mounds are

part of previously more extensive sedimentary units that filled and overtopped underlying impact craters. My study also revealed that most mounds are offset from the center of their host crater in the same direction as the present regional winds (*e.g.*, the mounds in Arabia Terra are offset towards the western portion of their craters). I propose that this implies that wind has been the dominant agent causing the erosion of central mounds.

In **Chapter 3** I present an in depth study of a single central mound (Mt. Sharp within Gale crater). I used Thermal Emission Imaging System Visible Imaging Subsystem (THEMIS-VIS) mosaics in grayscale and in false color to characterize the morphology and color variations in and around Gale crater. In contrast to Mars Reconnaissance Orbiter Context Camera (CTX) mosaics that primarily show albedo differences due to dust cover (such as wind tails) the THEMIS-VIS band 3 grayscale mosaic reveals more details about the morphology, including different textures, due to the images being acquired at later local times. Several sedimentary deposits are located in the region surrounding Gale crater, which implies that the geologic processes that created sedimentary deposits within Gale crater likely also contributed to sedimentary deposits outside the crater as well.

In **Chapter 4** I investigate current sedimentary materials on Mars: sand dunes. Aeolian activity is the primary geologic agent currently influencing the surface of Mars. Now that high resolution cameras have been orbiting Mars for decades, evidence of aeolian activity in the form of mobile dunes has been identified (*e.g.*, Bridges *et al*., 2011; Silvestro *et al.*, 2010; 2013). Analyzing these mobile dunes provides one of the very few sources of information about local wind regimes. In this chapter, I test the competing hypotheses that variations in a dune's albedo can be related to its ripple migration rate

and that dust is removed from the surface of a dune by dust devils. On Mars, where the atmospheric pressure is low, dust is removed from the surface of a dune by saltating sand. Therefore, more active dunes should remove dust more efficiently than less active dunes. A dune's albedo was found to be low in the first half of the Mars year (L_s = 0-180º) and high in the second half (L_s = 180-360º), during the dusty season. I find that a dune's minimum albedo does not have a simple correlation with its ripple migration rate. Instead, I propose that dust devils remove dust on slow-moving and immobile dunes, whereas saltating sand caused by strong winds removes dust on faster dunes. I also propose that albedo variations on a single dune field can reveal insight into the local wind regime.

The Moon is our nearest neighbor in the solar system and it provides a useful test bed for solar system science. It is the only planetary body humans have visited and one of the only planetary bodies from which we have returned samples. Any knowledge gained about the Moon from field work, returned samples, and remote sensing can help us to understand the solar system as a whole. Information about the Moon is relevant to one planetary body in particular: the Earth. The current prevailing hypothesis is that the Moon formed after a large body collided with the Earth. Therefore, the Moon and the Earth likely share some of the same source materials and learning about one body provides information about the other.

In **Chapter 5** I analyze volcaniclastic materials at the lunar surface that were emplaced by explosive volcanism, using many of the same kinds of remote sensing tools and skills that I developed and/or used for my Mars research summarized above. Volcanic glassy to crystalline beads brought back in the Apollo samples were found to be

sourced from more than 400 km below the surface (Shearer and Papike, 1993). Lunar pyroclastic deposits emplaced via fire fountaining contain materials directly sourced from the lunar interior. Their primitive composition may help to constrain the composition and geophysical evolution of the lunar magma ocean and the lunar mantle (Delano, 1986; Shearer and Papike, 1993). Pyroclastic glass beads returned as Apollo samples have surface coatings that indicate that they formed in volatile-rich eruptions, and recent reanalysis of the Apollo 17 glass beads revealed a small fraction of melt inclusions with water content as high as presumed by some for the Earth's mantle (Hauri *et al.*, 2011). The abundance and source of these volatiles may have major implications for the interior structure, composition, and origin of the Moon (Hauri *et al.*, 2015).

Lunar pyroclastic deposits are generally divided into small localized (< 1000 km^2 in area) and large regional (> 1000 km^2 in area) deposits (*e.g.,* Gaddis *et al*., 2003). Localized deposits are thought to form as a result of intermittently, violently, explosive Vulcanian eruptions under low effusion rates, in contrast to the higher-effusion rate, Hawaiian-style fire fountaining inferred to form larger regional deposits. The regional deposits are inferred to be deeply sourced and therefore their composition could be representative of the lunar interior.

In **Chapter 5**, I also analyze the mineralogy and composition of a group of localized pyroclastic deposits within Oppenheimer crater, a crater in the South Pole Aitken Basin. I use data from two orbiters, Lunar Reconnaissance Orbiter (LRO) and Chandrayaan-1. LRO is a NASA mission that launched in 2009 and is still currently orbiting the Moon. Chandrayaan-1 is an Indian Space Research Organization (ISRO) mission that orbited the Moon from 2008 to 2009. From LRO, I use visible images from

the Lunar Reconnaissance Orbiter Camera and thermal-infrared data from the Diviner Lunar Radiometer Experiment. From Chandrayaan-1 I use Moon Mineralogy Mapper near-infrared spectra. This work shows the benefits of combining multiple datasets from instruments on the same spacecraft as well as from missions created by different countries to address a scientific question. I find that the mineralogy of the pyroclastics varies both across the Oppenheimer deposits as a whole and within individual deposits. I propose that this variability in mineralogy indicates variability in eruption style, and that it cannot be explained by a simple Vulcanian eruption model. These results suggest that localized lunar pyroclastic deposits may have a more complex origin and mode of emplacement than previously thought.

In **Chapter 6** I summarize the major results and conclusions of the work presented in this thesis.

CHAPTER 2

A GLOBAL SURVEY OF MARTIAN CENTRAL MOUNDS: CENTRAL MOUNDS AS REMNANTS OF PREVIOUSLY MORE EXTENSIVE LARGE-SCALE SEDIMENTARY DEPOSITS

Bennett, K. A., & Bell, J. F., III. (2016). A global survey of martian central mounds: Central mounds as remnants of previously more extensive large-scale sedimentary deposits. *Icarus*, *264*, 331–341. http://doi.org/10.1016/j.icarus.2015.09.041

We conducted a survey of central mounds within large (> 25 km diameter) impact craters on Mars. I use mound locations, mound offsets within their host craters, and relative mound heights to address and extend various mound formation hypotheses. The results of this survey support the hypothesis that mound sediments once filled their host craters and were later eroded into the features observed today. The majority of mounds are located near the boundaries of previously identified large-scale sedimentary deposits. I discuss the implications of the hypothesis that central mounds are part of previously more extensive sedimentary units that filled and overtopped underlying impact craters. In this scenario, as erosion of the sedimentary unit occurred, the sediment within impact craters was preserved slightly longer than the overlying sediment because it was sheltered by the crater walls. My study also reveals that most mounds are offset from the center of their host crater in the same direction as the present regional winds (*e.g.*, the mounds in Arabia Terra are offset towards the western portion of their craters). I propose that this implies that wind has been the dominant agent causing the erosion of central mounds.

2.1 Introduction

Craters that contain central mounds of sedimentary deposits occur across the martian surface (Malin & Edgett, 2000), but the specific processes responsible for mound formation and subsequent modification are still uncertain. Process-specific models estimate formation times that range from tens to hundreds of Myr (Fergason & Christensen, 2008; Andrews-Hanna *et al.*, 2010) and crater counting at one mound implies that it formed during the Noachian-Hesperian boundary (Thomson *et al*., 2011). Since these interior crater deposits occur globally, mound formation mechanisms could be representative of a global process that was active throughout an extended period of early martian history.

Gale crater, the landing site for the Mars Science Laboratory (MSL) *Curiosity* rover, is an example of a crater containing a central mound. Gale's mound, Mt. Sharp, rises ~ 5 km above the crater floor and contains layered sediment that could preserve a record of early martian climate and habitability (Anderson & Bell, 2010; Milliken *et al.*, 2010; Thomson *et al*., 2011). *Curiosity* is currently investigating the basal units of that central mound and has already provided evidence that liquid water was present on the crater floor at some time in Gale crater's history and that the environment at that time would have been habitable (*e.g.,* Grotzinger *et al.*, 2013; Williams *et al.*, 2013). In order to place new discoveries at Gale crater into a global context, however, it is necessary to understand how Mt. Sharp relates to the entire population of central mounds.

A central mound is distinct from a central peak. Central peaks are formed from the rebound that occurs during an impact (*e.g.,* Pike, 1980; Melosh, 1989). In contrast, a

central mound is formed from sediment that is deposited in a crater some time after the impact. Central mounds are found in craters of varying sizes, are not always located in the center of their host crater, and at times rise higher than the crater walls (Malin & Edgett, 2000). The deposits are hypothesized to have been created by either subaerial or subaqueous processes through one of two general formation mechanisms. The first (prevailing) hypothesis suggests that after their craters were formed, sediment filled the entire crater and was later eroded into the morphologies observed today (Malin & Edgett, 2000). Alternatively, a competing hypothesis suggests that the mounds formed in place and the sediment never extended to the crater walls (Kite *et al.*, 2013).

Previously proposed specific methods of mound formation include ice-related, aeolian, explosive volcanic, impact, alluvial, deltaic, lacustrine, and submarine processes (Andrews-Hanna *et al*., 2010; Cabrol & Grin, 1999; Fergason & Christensen, 2008; Kite *et al.*, 2013; Malin & Edgett, 2000; Rossi *et al*., 2008; Thomson *et al*., 2011). For example, in one ice-related formation model (Fergason & Christensen, 2008), mound features in Arabia Terra were created from airfall dust that was cemented by frost induced by obliquity changes. Sediment continued to fill the entire crater and be cemented over millions of years until a change in the atmospheric environment caused the cemented material to begin to erode. In contrast, an example of an aeolian hypothesis (Kite *et al.,* 2013) proposes that slope winds from the crater lead to net accumulation of indurated material in the center of the crater.

Previous surveys of central mounds have either been part of a broader survey of sedimentary deposits on Mars (Malin & Edgett, 2000) or have been limited to small areas (Fergason & Christensen, 2008) or large craters (>100 km in diameter; Zabrusky *et al.*

2012). This work presents a new global survey focusing specifically on central mounds in craters larger than 25 km in diameter, with the goals of identifying any global or local trends relating to the height, offset, or aerographic location of the mounds. I use these metrics to assess hypotheses for the formation and subsequent alteration of these features, as well as to place Mt. Sharp in Gale crater in a global context.

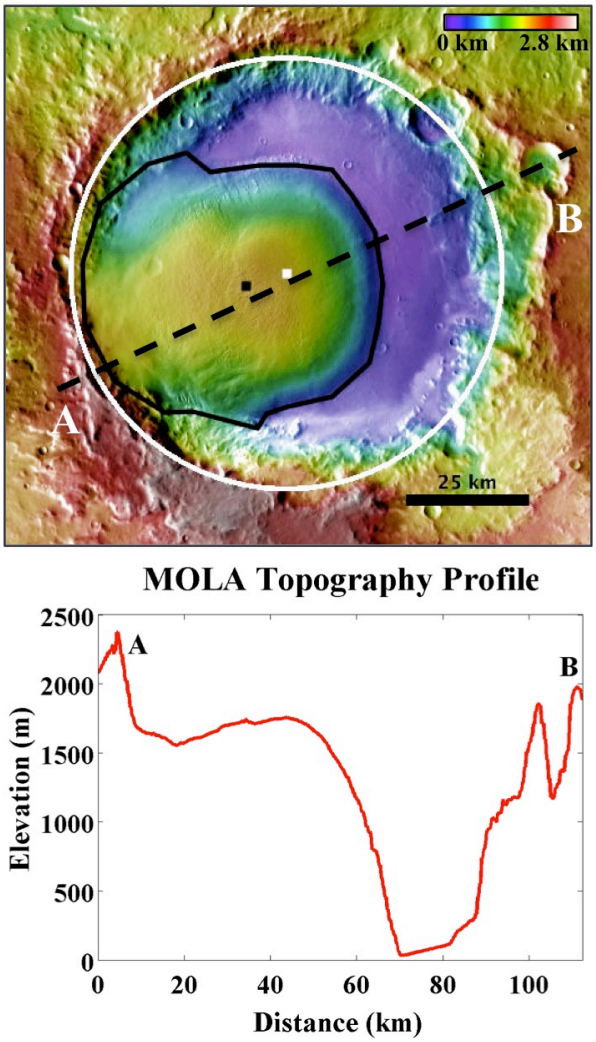

Figure 2.1 Identifying mounds and their offsets. (top) Obtaining mound offset from an unnamed crater in Arabia Terra at 23.5°E and 3°S. The dashed line shows the location of the MOLA profile. The white circle and dot are approximated as the crater and its center. The black polygonal outline traces the topographic edge of the mound. The center of the mound (black dot) is the average latitude and average longitude of the mound outline. (bottom) MOLA elevation profile of the crater and its mound.

2.2 Methods and Datasets

To identify and characterize central mounds I used a combination of visible, thermal, and topographic elevation datasets. My search area was limited to within ±60° latitude and to craters larger than 25 km in diameter, to avoid the potentially confounding effects of high latitude surface or ground ice features, to keep the sample size of my survey population tractable, and to stay above the resolution limits of all the orbital data sets to be employed. I do not include sedimentary mounds within canyons in this study, to avoid potential differences in formation mechanisms that could result from the different settings. To be classified as a central mound in my study, an interior crater deposit must be rounded (as opposed to a typically sharp or jagged central peak) and the height of the mound above the crater floor must be greater than 20% of the height of the rim above the crater floor.

I used global Mars Global Surveyor Mars Orbiter Laser Altimeter (MOLA) (Smith *et al.*, 2001) topography maps and Mars Odyssey orbiter Thermal Emission Imaging Spectrometer (THEMIS; Christensen *et al.*, 2004) daytime infrared temperature maps to identify potential mound features. To judge whether each feature met my criteria, I constructed elevation profiles of each crater and also examined Mars Reconnaissance Orbiter Context Camera (CTX; Malin *et al.*, 2007) and High Resolution Imaging Science Experiment (HiRISE; Delamere *et al.*, 2010) visible images.

For features identified as mounds, I found the distance between the center of the crater and the center of the mound to determine the offset. Using the Geographic Information System software tool JMARS (Christensen *et al.*, 2009), each crater containing a mound was fit (by eye) by a circle, and I recorded the center latitude and

longitude of this circle as the center of the crater. To find the center of each mound, I created polygon shapefiles marking the topographic edge of each mound and defined the center as the average latitude and average longitude of these polygons (Figure 2.1). I also obtained the area of each mound from these shapefiles and normalized this value by dividing it by the host crater area. I measured the highest elevation of the mound and the elevation of the bottom of each mound by finding the minimum and maximum elevation within these shapefiles. Consequently, the bottom of the mound is defined as the elevation where the break in slope occurred between the steep edge of the mound and the (typically) flat crater floor. Some craters (such as Gale) also exhibit large differences in elevation along their rims. Therefore, I found the highest and lowest elevation (excluding incised channels) of each crater rim. I also found the lowest elevation of the crater floor (excluding more recent impact craters that struck the crater floor). I calculated the crater rim height by finding the difference in the elevation between the highest and lowest rims and the crater floor. Finally, I compared the height of each mound with the height of its host crater's rim to determine how many mounds rise above their host crater walls.

We then use the data collected in my survey of central mounds to test various hypotheses regarding mound formation mechanisms. As I am testing hypotheses for many different geologic processes, detailed modeling of each process lies outside the scope of this study. Instead, here I primarily present my survey of central mounds and compare their characteristics to models and datasets already published in the literature. In Section 4.3 below, I use a synthesis of my new global survey results to propose a model for central mound formation that can be further tested with future data and analysis methods.

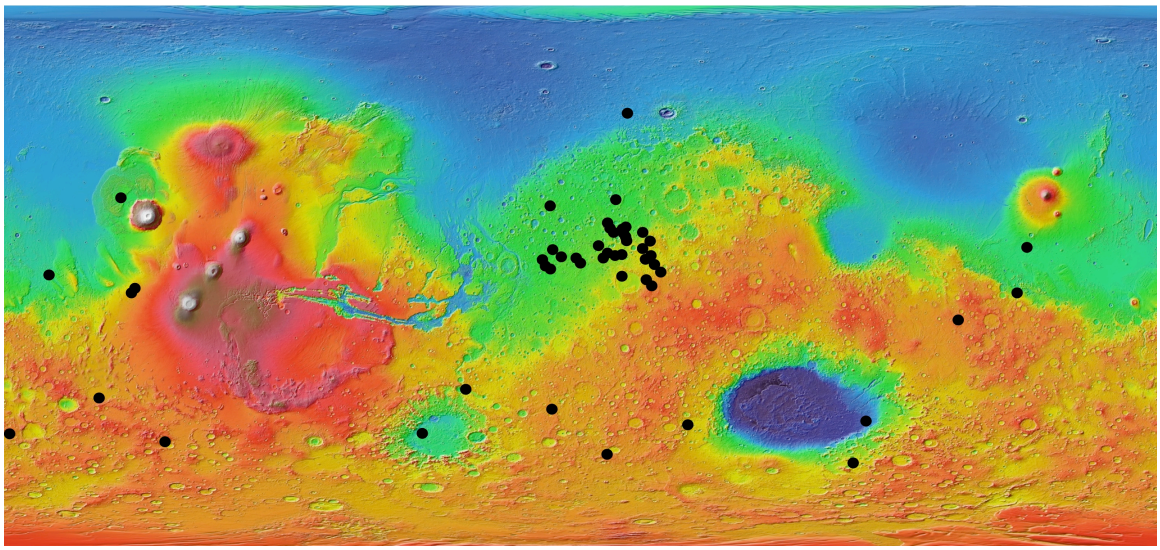

Figure 2.2 Global survey of craters containing central mounds. Background: Colorized global MOLA elevation map (red/white=high, green/blue=low), centered on 0° latitude, 0° longitude.

2.3 Results

2.3.1 Global Survey

Our global survey identified 50 features that met my criteria to be categorized as a central mound (Figure 2.2; Appendix A). I found 33 such mounds in the northern hemisphere and 17 in the southern hemisphere. Western Arabia Terra (from 10°S to 30°N and 20°W to 30°E) contains 32 mounds, which is more than 60% of the total population I identified. There are 36 mounds that are located within 20° of the equator.

2.3.2 Central Mound Height, Area, and Offset

Figure 2.3 shows how each mound's height compares to its host crater's highest (red points) and lowest (blue points) rim height. Points above the black line are mounds that rise above the crater rim. There are 32 mounds (out of 50) that rise above the crater's lowest rim height, but there are only two mounds that rise above the entire crater rim: Nicholson crater and an unnamed crater in Arabia Terra centered at 24.8°E and 3.6°N. Central mounds in my survey take up an average of 40±20% of their host crater floor. Mounds within Arabia Terra are slightly larger than average (50±20%) , while the remaining mounds take up only 20±10% of their host crater floor.

The majority of central mounds are offset from the center of their host crater, but the overall population of mounds does not appear to be offset in a particular direction (Figure 2.4). However, almost all the mounds in Arabia Terra (blue triangles) are offset to the western side of their host crater (E-W offset = 20±10% of normalized crater radius west, N-S offset = 0±20%). The remaining mounds (red squares) are not offset in a particular direction (E-W offset = 0±20%, N-S offset = 0± 20%).

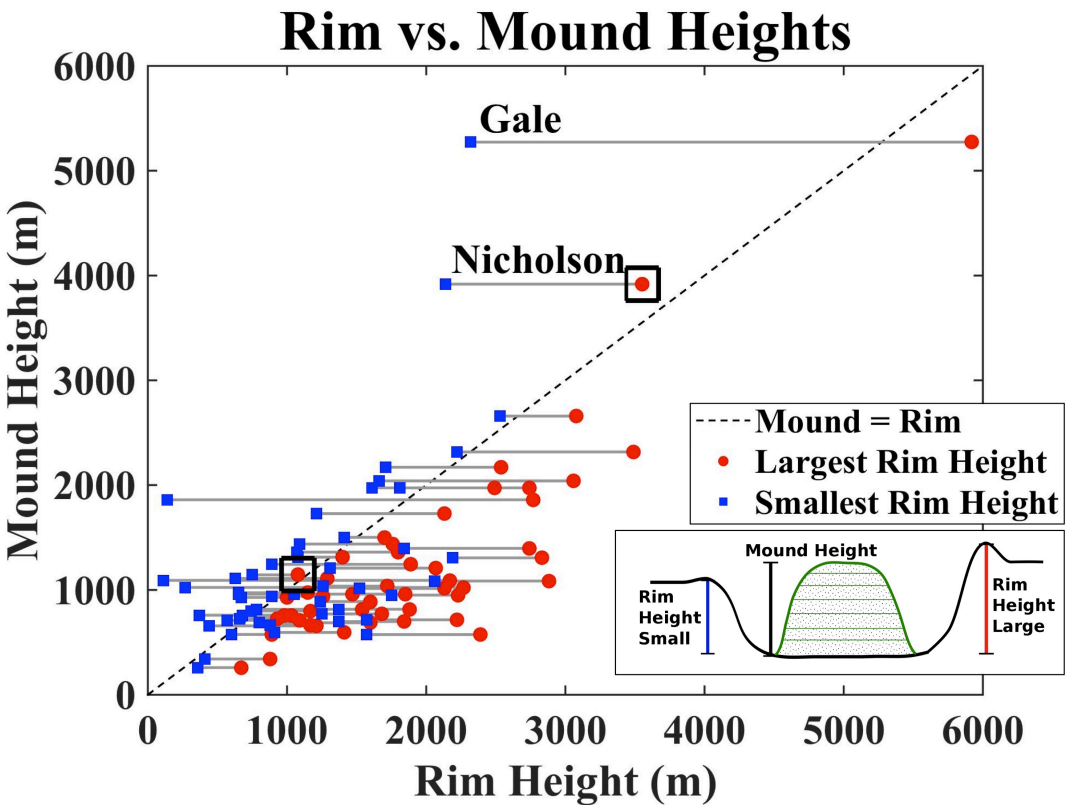

Figure 2.3 Plot comparing each mound's height to the largest (red) and smallest (blue) height of its host crater rim. The points for each crater's highest and lowest rim height are connected by grey lines. These grey lines indicate the difference in height between the highest and lowest parts of each crater rim. The 1:1 line shows where a mound and its crater rim would be equal heights. Points above this line, like Gale, represent mounds that are taller than their crater rim. This figure shows that there are 32 mounds that are taller than the lowest part of their crater rim, but only two mounds (in black boxes; Nicholson and an unnamed crater in Arabia Terra centered at 24.8° E and 3.6° N) that are taller than the highest part of its crater rim.

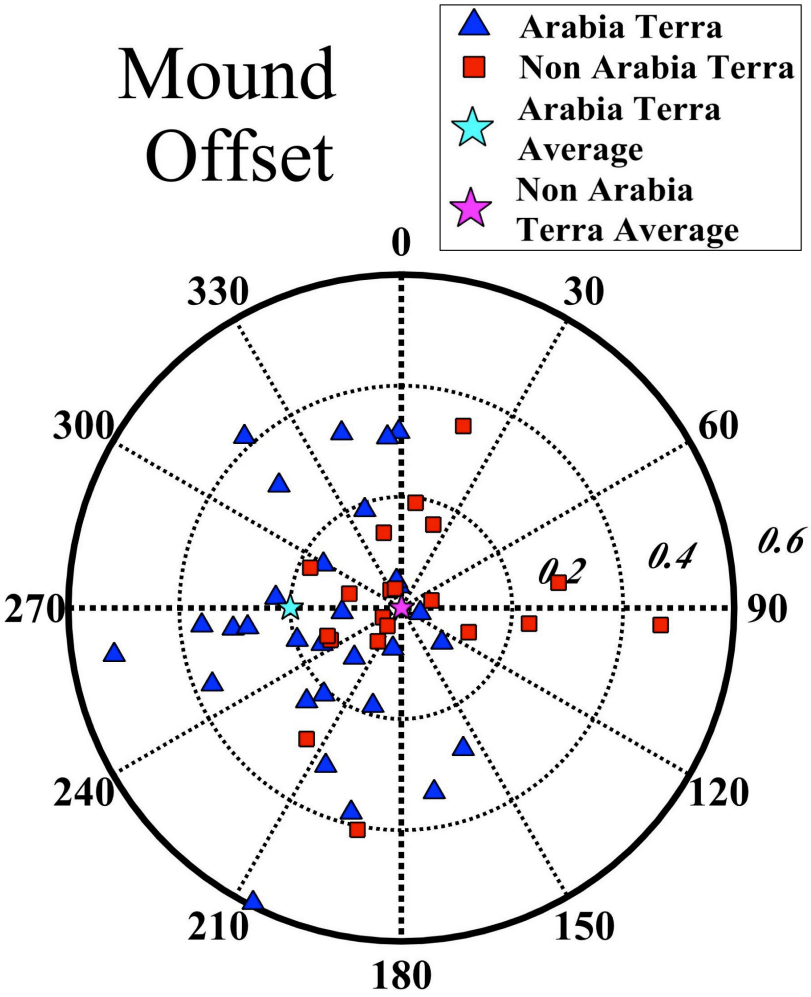

Figure 2.4 Plot showing the offset of each mound from its crater center. The distance from the center is normalized by the crater radius. Blue triangles represent mounds located in Western Arabia Terra. Red squares represent all other mounds.

2.4 Interpretation and Discussion

We use these results to test several hypotheses regarding the formation mechanism of central mounds. First, I compare the location of central mounds to other global features, then I consider the geologic agents for the deposition and erosion of sediments, and finally I discuss Gale crater in a global context.

2.4.1 Location of Central Mounds

Figure 2.5 shows the distribution of central mounds along with six labeled previously identified large-scale sedimentary deposits (Arabia Terra, Medusae Fossae Formation, Argyre, Hellas, the Electris deposits, and the South Polar Pitted Terrain; Tanaka, 2000). These sedimentary deposits were originally identified as potential relict ice and dust deposits based on their erosional morphologies, which are indicative of fine grained material (Tanaka, 2000). I do not discuss the south polar pitted terrain as it lies outside my survey area. Roughly 40 mounds occur inside or within several hundred kilometers of the borders of these deposits. Fewer than half of these (18) occur within the borders and more than half (22) lie on the edge or outside of the deposits. I hypothesize that the large-scale sedimentary deposits were once more extensive, and that central mounds are remnants of this unit. As the sedimentary deposit was eroded back, material within craters was eroded more slowly than the overlying unit and formed features that I identify as central mounds. Previous work suggests that both the Arabia Terra deposits and Medusae Fossae Formation were once more extensive (Zabrusky *et al.*, 2012; Bradley *et al.*, 2002). The occurrence of mounds of sedimentary origin within craters near

the boundary of large-scale sedimentary deposits is indeed consistent with the hypothesis that these deposits were once more extensive.

The majority of mounds are located near the Arabia Terra deposits. This could potentially be because Arabia Terra is the largest sedimentary deposit identified, and thus there is a larger area for sediment to infill craters. Alternatively, the large number of central mounds in Arabia Terra could be related to the fact that the Arabia Terra deposit is the only large-scale sedimentary deposit that is located in the southern highlands where there are an abundance of craters to fill. The Medusae Fossae Formation is located across the north/south dichotomy and in the northern lowlands. There are fewer craters in this area for the sedimentary deposit to fill. The Argyre and Hellas Basins each contain one central mound at the boundary of the large-scale sedimentary deposit. These deposits cover almost the entire area of each basin's floor, which could imply that Hellas and Argyre are just starting to experience erosion or that deposition is still occurring. The Electris deposits are smaller in area than the rest of the deposits, which could explain the lack of central mounds in that area.

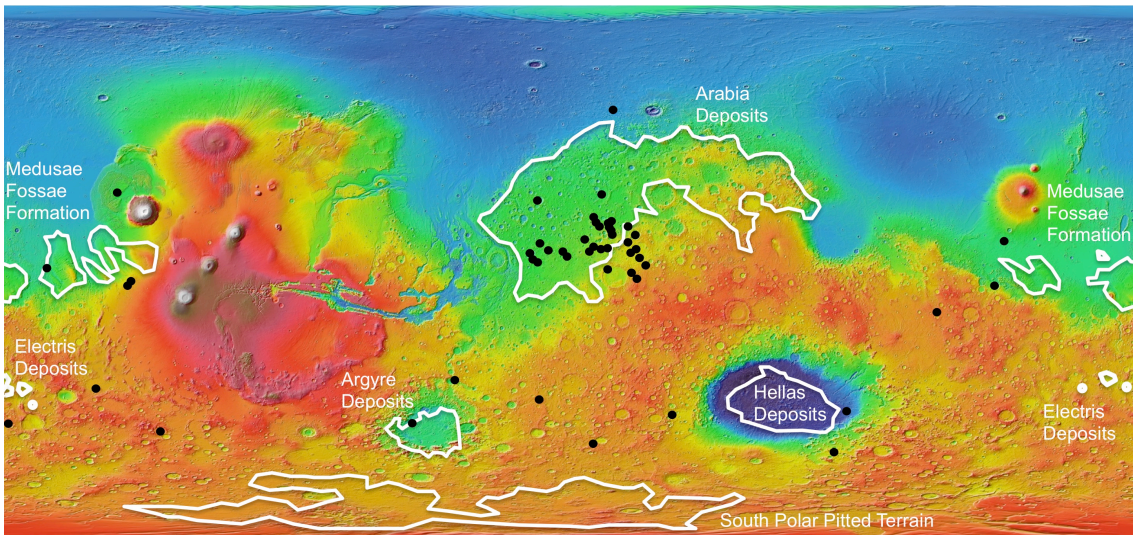

Figure 2.5 The location of central mounds identified in this study compared to the outline of large-scale sedimentary deposits identified in Tanaka (2000).

2.4.2 Geologic Agents

2.4.2.1 Deposition

Many studies have addressed possible formation mechanisms for central mounds (*i.e.,* Fergason & Christensen, 2008; Kite *et al.*, 2013; Malin & Edgett, 2000; Zabrusky *et al*., 2012). Since I hypothesize that mound sediment is a remnant of a previously more extensive sedimentary unit, I will consider this as a constraint for mound formation mechanisms and use this section to discuss the implications of such a constraint. I will also consider an alternative formation mechanism in which mounds are associated with a large sedimentary unit, but not necessarily a continuous part of that unit.

In the scenario that mounds are remnants of a previously more extensive unit, any model for the deposition of mound material must also account for the deposition of the larger parent unit of the mound. In a subaqueous scenario, geologic agents that act locally (such as rivers, deltas, or crater lakes) likely cannot be solely responsible for both intra- and inter-crater deposits. These processes could have acted locally on individual mounds, but they likely are not the primary geologic agent responsible for depositing mound material. For example, a lake within a crater in Arabia Terra could have deposited sedimentary material within the crater, but it could not have deposited the sedimentary material observed in the plains outside of the crater that make up the large-scale Arabia Terra deposits. In order to accommodate such vast areas of the large-scale sedimentary deposits and the varied ranges of elevation of all central mounds, a subaqueous process that is the primary depositional agent of these deposits would need to be submarine. To deposit the material of all the central mounds in my survey (*i.e.,* to deposit materials at the central mound with the highest elevation), there would need to have been a global

ocean with a surface elevation of ~ + 3 km (relative to today's datum), from which only the Tharsis volcanoes emerged. For example, Figure 2.6 shows the extent of a hypothesized global ocean with a surface level at +2 km, which is the elevation of the highest mound within Arabia Terra. However, I judge this submarine scenario to be implausible for a variety of reasons. For example, where did that much water come from and where is it now? Estimates of martian degassing obtained from meteorites can account for some of the water (one high estimate calculates a depth of 200 m globally; McSween & Harvey, 1993), but even high estimates cannot supply a global ocean at this elevation. In addition, a global ocean would have needed a surface level at +2 to +3 km, whereas the shoreline hypothesized by Parker *et al.* (1989) was estimated to have an average elevation of -3 to -4 km (Head *et al.* 1999).

An alternative aqueous depositional setting that would not necessarily require a global ocean is groundwater upwelling resulting in playa deposits. Andrews-Hanna *et al.* (2010) developed a model of groundwater upwelling in order to explain the evidence of playa features observed in Meridiani Planum. Zabrusky *et al.* (2012) demonstrated that Meridiani-like sedimentary deposits exist across Arabia Terra, providing further support that groundwater upwelling could have created the sedimentary deposits in this area. While this mechanism could potentially have created the central mounds and the large sedimentary deposit in Arabia Terra, it is less likely that other central mounds across Mars were deposited through groundwater upwelling. Indeed, Andrews-Hanna *et al.* (2007) showed that the Meridiani-Arabia area is a preferred locus for groundwater upwelling to occur on Mars.

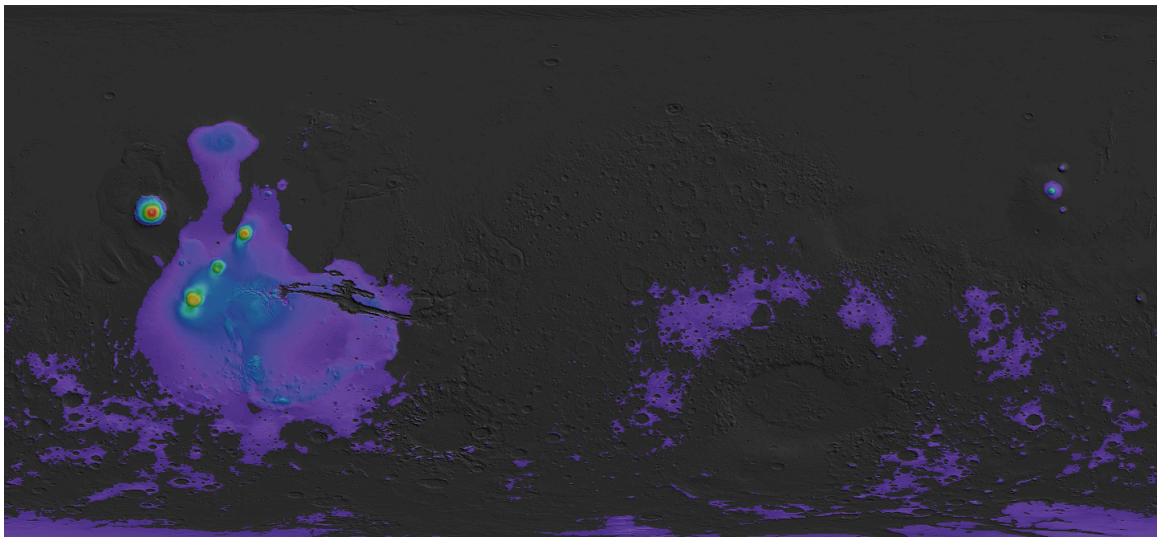

Figure 2.6 Grey shaded topography represents the surface of Mars that would be covered by a global ocean with a surface elevation equal to the elevation of the highest elevation central mound in Arabia Terra (~ +2 km). The highest elevation mound is at +3 km.

Next, I investigate whether impact ejecta could be the primary source of materials in central mounds. At least three mounds are covered by visible ejecta blankets (*i.e.,* Figure 2.8). Since I observe ejecta at the top of some mounds, and because impact cratering is a primary geologic process on Mars, it is likely that impact ejecta contributed to mound growth at multiple times during mound formation. However, impact ejecta cannot be the primary component of all mounds because ejecta is not likely to create the laterally-extensive, continuous and at times rhythmic layers observed in many of the mounds (Malin & Edgett, 2000).

Kerber *et al.* (2012, 2013) modeled the distribution of ash from 16 martian volcanoes hypothesized to exhibit explosive activity. These studies found that ash dispersal was concentrated around the Tharsis volcanoes, in the Cerberus plains to the east of Tharsis, across northern Arabia Terra, and around the South Pole. These studies concluded that several of the large-scale sedimentary deposits (specifically, the Medusae Fossae Formation, Arabia Terra, and the Electris Deposits) could primarily consist of pyroclastic material. While there are significant accumulations of ash within the Arabia Terra deposit and the Medusae Fossae Formation, only five mounds (one near Tharsis [218° E, 24.5° N]; three near the Medusae Fossae Formation [223.3° E, 4.3° S], [221.2° E, 5.3° S], [195.9° E, 0° N]; one near Arabia Terra [16.4° E, 52.5° N]) are in locations modeled to receive more than 200 meters of ash. The mounds identified in this survey are taller than 200 meters (many are a kilometer high or more). Therefore, while ash could have contributed to the growth of central mounds, it appears unlikely to have been the primary component of all mounds based on existing pyroclastic ejecta modeling. There is one possible exception, however: the ash dispersal modeling work of Kerber *et al.* (2012,

2013) shows that the craters hosting central mounds near the Medusae Fossae Formation could have received enough ash to form significant intracrater deposits. These results (along with previous observations that the Medusae Fossae Formation is extremely friable and has likely already been significantly eroded; *e.g.,* Bradley *et al.*, 2002) imply that with an explosive volcanic origin, the Medusae Fossae Formation could have been previously more extensive and that several central mounds could contain Medusae Fossae Formation material.

These results have additional significance. Since I hypothesize that central mounds are part of previously more extensive sedimentary units, if ash dispersal cannot explain the central mounds, it cannot explain the large-scale regional sedimentary deposits either. Specifically, modeling showed that the ash dispersal in Arabia Terra could mostly account for the sediment in the large-scale sedimentary deposit in that area (Kerber, 2013). However, the majority of the ash was distributed in northwestern Arabia Terra, while the 32 mounds are located in southwest Arabia Terra. If the regional sedimentary deposit was once previously more extensive and included the area where the central mounds are located, these results could imply that the Arabia Terra large-scale deposits are not pyroclastic in origin. Alternately, perhaps the modeling predictions do not reflect the actual distribution of deposited pyroclastic materials based on the distribution of remaining central mounds.

Fergason & Christensen (2008) proposed that the most likely mechanism of formation for a subset of mounds in Arabia Terra is air fall dust that is cemented by ice during periods of high obliquity. Here, I compare my population of central mounds to high northern latitude crater mound features previously identified by Conway *et al.*

(2012). These ice-associated crater mounds are hypothesized to be either eroded ice and dust deposits or remnants of a past, more extensive, polar cap. Figure 2.7 shows the mound inside high latitude Korolev crater next to the Arabia Terra mound within Henry crater. These two mounds are morphologically similar. The elevation profiles show the mounds both have steep sides and a flat top. Conway *et al.* (2012) shows that many of the high northern latitude mounds are offset to the western side of the crater, and my study shows the same result for the Arabia Terra mounds. While these observations may be more closely related to the erosion of central mounds than to their deposition, it is still useful to note their similarities. Indeed, the fact that there are similarities between the high northern latitude mounds and the Arabia Terra mounds means that an ice-related formation mechanism (*i.e.*, Fergason & Christensen, 2008) potentially remains valid for the mounds in Arabia Terra, and possibly for the global population.

The hypothesis that the high northern latitude mounds are remnants of a past, more extensive polar cap is analogous to my hypothesis that central mounds are remnants of past, more extensive sedimentary deposits. However, the low latitude central mounds are not likely to be remnants of a past polar cap. This is because the creation of the Tharsis province in the mid-Noachian stabilized Mars and prevented extended periods of polar wander (*e.g.,* Melosh, 1980; Matsuyama et al., 2007). Instead, low latitude central mounds could result from a regional ice and dust deposit that was emplaced during one or more periods of past high obliquity. As the obliquity and climate changed, the dusty ice would have begun to be eroded and the ice itself could have been sublimated away. At some point in this process, Arabia Terra could have become a location of dust accumulation. The features I observe as mounds could then be layers of dust and ice that

were once more laterally extensive, but have since begun to be eroded back. Addition of more recent layers of dust could be preventing the ice from sublimating in the current thin atmosphere, and also preventing me from observing its albedo or spectral signatures. Alternatively, the ice could have sublimated away after each period of high obliquity so the features observed today consist of layers of indurated dust and no ice.

Conway *et al.* (2012) proposed that many of the high latitude mounds were not extensions of a polar cap or other ice-related deposits, but instead were the result of microclimates preferentially causing the deposition of ice within craters. Here I discuss the possibility that central mounds may be associated with a large sedimentary unit, but are not necessarily part of that unit. Conway *et al.* (2012) showed that deep craters beyond the edge of the polar cap exhibit lower temperatures than the surrounding plains. These lower temperatures cause more volatiles to be deposited as ice within the craters than the plains, and also prevent all of the ice from sublimating in the summer. This causes the craters to be a net sink for volatiles, and a mound incorporating those volatiles could be built up over many years (Conway *et al.*, 2012). This hypothesis could be modified to apply to the low latitude mounds, specifically the mounds in Arabia Terra. For example, during different past obliquities ice and dust could have been deposited across northern Arabia Terra, but the deposits might not have reached southern Arabia Terra. However, in some deep craters beyond the boundaries of the ice/dust deposits, microclimates caused by low temperatures within the craters could have enhanced the deposition of ice and prevented its sublimation during warmer periods. Over many years, or many obliquity cycles, sedimentary deposits and crater mounds in Arabia Terra could have been separately deposited as a result. One potential flaw in relating this hypothesis

to low latitude mounds, though, is that the high latitude mounds appear to have a high concentration of water ice (Conway *et al.*, 2012). Mounds that are predominantly ice should not persist at low latitudes to the present day. In order for such a scenario to work at low latitudes, then, the microclimates would also need to trap dust or some other sediment that would remain as residual mound material once the ice sublimated away.

The deposition of mound sediment is unlikely to be solely an aeolian process. Aeolian processes could have contributed to the deposition of materials in the crater (especially in ice/dust scenarios like those discussed above), but they likely did not act alone. Dry aeolian deposition would not have indurated the material or created the phyllosilicate and sulfate signatures observed near at least one central mound (Gale; Milliken *et al.,* 2010).

To summarize my discussion of the geologic agents that could have contributed to the primary deposition of mound sediment: widespread fluvial and subaqueous processes appear unlikely; groundwater upwelling could have created the Arabia Terra deposits, but likely did not contribute to other mounds; an explosive volcanism origin appears unlikely except near the Medusae Fossae Formation; ice-related processes (both air fall dust that is cemented by ice during periods of high obliquity and microclimate trapping of ice) are consistent with my results; aeolian processes likely contributed to the growth of mounds, but they likely did not solely create the deposits. Other geologic agents could have acted locally at individual mounds, but are not likely to have been the primary process responsible for depositing mound materials.

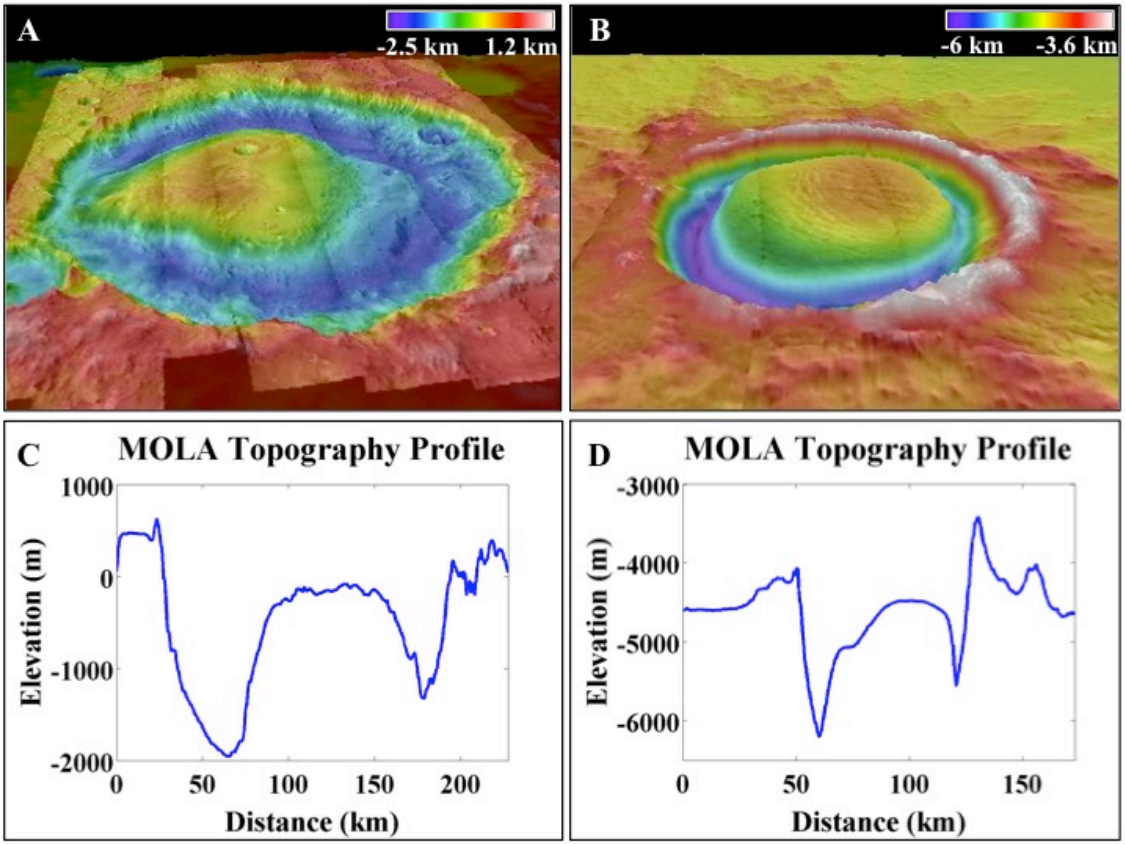

Figure 2.7 Similarities between equatorial mounds (Henry) and high latitude mounds (Korolev). CTX images overlain by colorized MOLA elevation for (A) Henry crater and (B) Korolev crater. MOLA elevation profiles across the center of each mound for (C) Henry crater and (D) Korolev crater.

2.4.2.2 Erosion

Perhaps the most compelling question about mounds is this: How could materials that are kilometers thick have been eroded and transported out of their parent craters? There are no outlet channels associated with mound-hosting craters, which makes it difficult for water and ice to transport sediments away. Rather, previous studies of central mounds and especially the large number of yardangs associated with mounds have led some to conclude that wind was the most likely contributor to the erosion of mounds (*e.g.,* Fergason & Christensen, 2008). The global study also supports wind as the primary agent of the erosion of central mounds. For example, the Arabia Terra mounds (60% of mounds in the survey) exhibit mound offsets towards the western side of their host craters. According to General Circulation Models (GCMs), the prevailing annual net wind direction in Arabia Terra is slightly south of west (*e.g.,* Fenton & Richardson, 2001). If this model represents the prevailing winds during mound formation, this implies that wind could have helped to preferentially erode sediment into mounds located on the western sides of craters. Preliminary results from wind modeling by Day *et al.* (2014) show that a unidirectional wind will erode filled martian craters into mounds that are offset in the same direction as the wind. These results imply that easterlies (as are expected in Arabia Terra) could have eroded mounds into the features that are observed now. This hypothesis predicts that the sedimentary deposit that sourced the Arabia Terra mounds should be located to the west of the mounds. Figure 2.5 shows that there is indeed a large part of the deposit that lies to the west of the mounds. My results in Arabia Terra are also consistent with the results of Conway *et al.* (2012) in the high northern latitudes, who found that mounds close to the polar cap where winds are stronger are

offset to the west, which matches the easterlies expected in this area (*e.g.,* Tanaka & Hayward, 2008; Howard, 2000).

In their mound formation modeling, Kite *et al.* (2013) invoke slope winds from the crater walls that lead to net accumulation of indurated mound material in the center of the crater. Such a model of in-place mound formation, where the sediment does not extend to the crater walls, does not match observations from my survey that reveal that the majority of mounds are offset from the center of their crater.

Wind as the primary geologic agent of erosion could explain why almost no mounds rise above the highest part of their host crater rim. Winds across the surrounding plains should erode the overlying sediment before eroding material below the crater rim, therefore any sediment rising above the rim would be subjected to preferential erosion. My study shows that many mounds rise above at least parts of their crater rims (Figure 2.3). However, only two mounds (in Nicholson crater and in an unnamed crater in Arabia Terra centered at 24.8°E and 3.6°N) rise higher than the tallest point on their crater rim (Figure 2.8). I interpret the highest point in Nicholson crater's mound as most likely part of a central peak, around which the mound formed. I interpret the highest point in the mound in the unnamed Arabia Terra crater as most likely part of a younger ejecta blanket from a nearby crater. The impact ejecta from the nearby crater does not make up the entire mound, however. At its thickest point in a location away from the mound, the ejecta blanket reaches 320 m above the surrounding plains. The mound's vertical relief is nearly 1150 m, though, so there must have been at least 800 m of mound material already in the crater before the ejecta blanket covered it. Therefore, this particular crater's actual mound material also does not appear to rise above its entire crater wall.

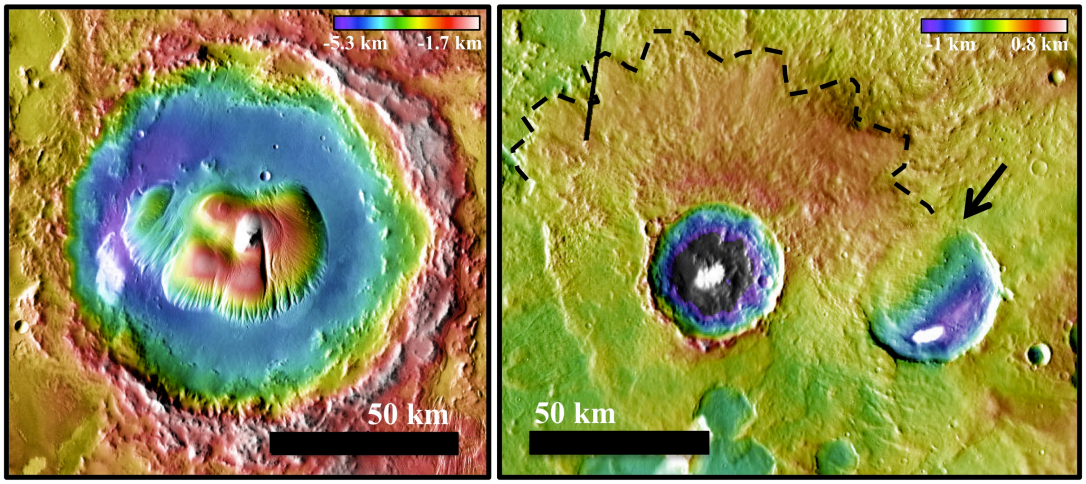

Figure 2.8 The two central mounds that rise above their crater rim. (left) Nicholson crater. (right) Mound in unnamed crater in Arabia Terra (black arrow). The crater to the left is younger, has no mound, and exhibits a visible ejecta blanket (outlined with the black dashed line) that partially covers the central mound in the crater to the right.

To summarize, I propose that wind erosion of mounds explains why there are no mounds that rise above the highest part of their parent crater rim. Wind erodes the overlying sediment first, and any sediment rising above the rim would be subjected to preferential erosion. Mounds that rise higher than their entire host crater rim are either due to a central peak rising above the mound and above the rim (as in Nicholson crater) or to impact ejecta that was emplaced on top of a pre-existing mound that was lower than the rim (as in the unnamed crater in Arabia Terra).

2.4.3 A Model for Central Mound Formation

Figure 2.9 outlines my favored cartoon model for martian central mound formation, based on previously-published models cited above and the results of my new global survey presented here. I propose that mound formation proceeded as follows: 1) Impact creates an "empty" crater. 2) Sediment fills the crater and covers the surrounding area (likely through ice cementation of air fall dust, but deposition of pyroclastic material is also possible in some cases). 3) The deposition of material ceases. 4) Wind erosion begins, and the overlying material is eroded. 5) Once the material above the crater rim has been eroded, material in the crater begins to be eroded by wind. 6) (Current) Continuing erosion of material in crater.

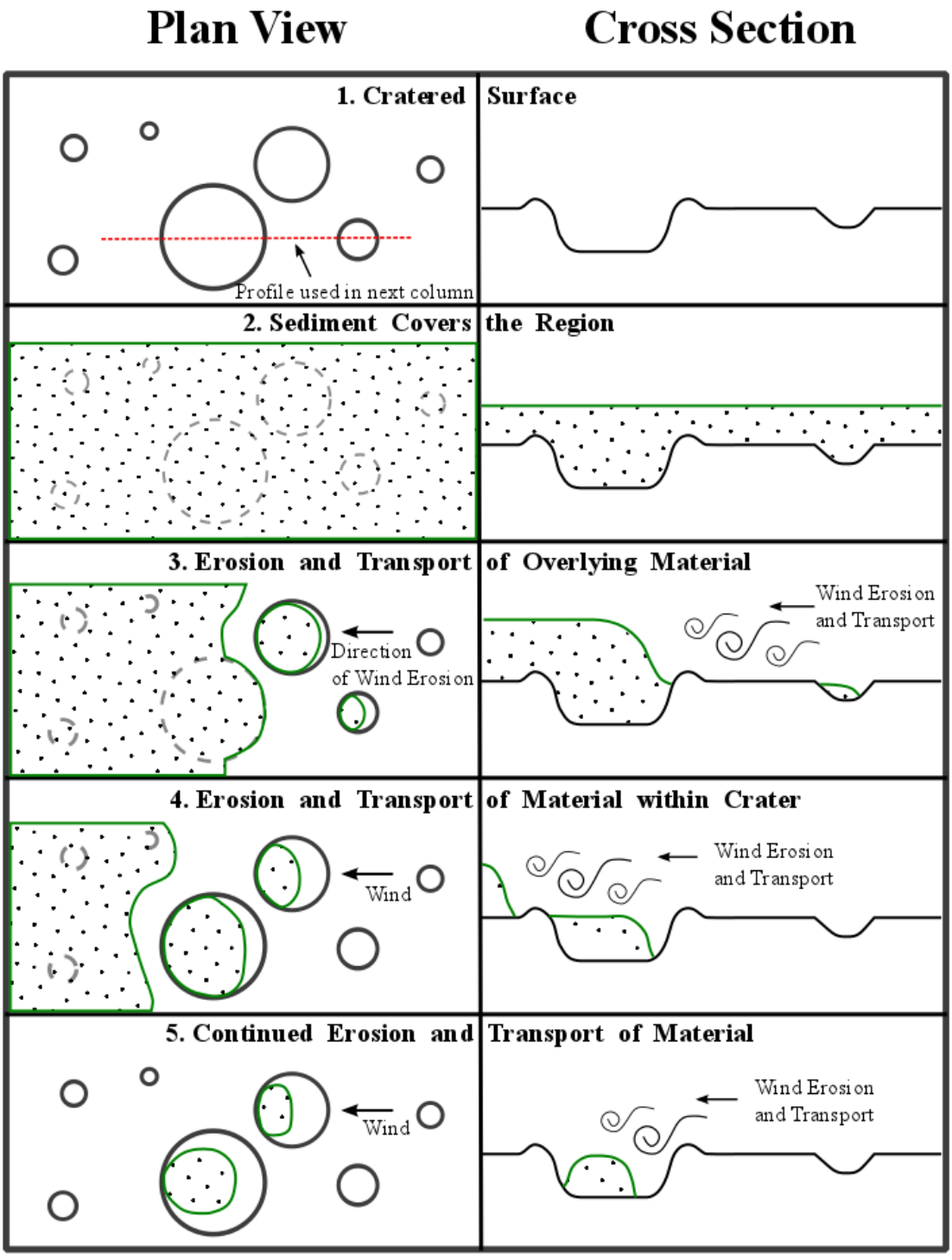

Figure 2.9 My favored cartoon model of martian central crater mound formation, based on previously-published models and the results of the new global mound survey described here.

2.4.4 Timescales

Several age estimates have previously been calculated for central mounds. Crater counting and superposition relationships suggest that the lower mound of Mt. Sharp was emplaced either during the Noachian/Hesperian transition or in the early Hesperian (Milliken *et al.*, 2010; Thomson *et al.*, 2011, Le Deit *et al.* 2013). The deposition of the upper mound and subsequent erosion of the entire mound must have then taken place at some point during the Hesperian and possibly the Amazonian epochs.

The north polar crater mounds are thought to be younger than 100 Ma, and some could be as young as 1-10 Ma depending on the magnitude of sedimentation rates at the poles (Garvin, 2000). Although these ice-related crater mound features are not included in my survey of central mounds, the polar mound results provide insight into mound-forming processes in general, and could indicate that mound-like features could have formed extremely recently in martian history.

Our study identified a central mound within a crater that impacted the aureole deposits located to the northwest of Olympus Mons. The aureole deposits are hypothesized to have formed around 3.4 Gy ago, however they are highly erodible. Craters on the aureole deposits are rapidly deconstructed, as shown by the anomalously low number of craters observed (Morris, 2007; Neukum *et al.*, 2004). This implies that the crater, and therefore its central mound, are relatively young.

Our study also identified several central mounds near the Medusae Fossae Formation, which is one of the youngest formations on Mars. The deposit is friable and easily weathered by wind, therefore it is thought that the Medusae Fossae Formation could have been much more extensive in the past (Bradley, 2002). Six craters containing

central mounds are located close to the Medusae Fossae Formation, including Gale and Nicholson. A section of Gale's central mound has previously been proposed to be a part of the Medusae Fossae Formation (Thomson *et al.*, 2011; Zimbelman & Scheidt, 2012). Nicholson, the two unnamed craters at the southeast edge of the Medusae Fossae Formation, and the unnamed crater on the flank of Olympus Mons have similar morphology to the Medusae Fossae Formation. This supports the hypothesis that these central mounds contain materials from the previously more extensive Medusae Fossae Formation. There are several implications I can draw from this potential relationship to central mounds. The Medusae Fossae Formation is thought to be one of the youngest geologic units on Mars with an age in the Amazonian or at the earliest, in the late Hesperian (Bradley, 2002; Watters *et al.*, 2007). If some central mounds have the same source as the Medusae Fossae Formation, this implies that either the period of mound formation is much more recent than previously thought, or the period of mound formation stretches through most of Martian history, from Noachian to Amazonian times. If central mounds were still being constructed during the Amazonian epoch, either the subsequent rate of erosion must have been high or the sediment was more easily erodible. The latter appears to be the case for the Medusae Fossae Formation.

2.4.5 Gale Crater

Mt. Sharp in Gale crater is an unusual central mound. It has the largest vertical relief of any mound and the 4th largest area. Most central mounds exhibit a consistent morphology throughout the mound, whereas Mt. Sharp has several distinct sections, or formations. Like most mounds, Mt. Sharp is located near the equator and is taller than the

lowest, but not the highest, part of its crater rim. The mound is offset to the north side of Gale crater, which is opposite the southern regional wind direction. The current wind regime would have eroded the central mound such that it would be offset to the south, not the north. Therefore, Mt. Sharp's northern offset was not likely caused by the current wind regime.

Our hypothesis for the global population of central mounds is that central mounds are part of a previously more extensive large-scale sedimentary unit. As a unique and complex central mound, Mt. Sharp may require a slightly more complex story. Gale Crater is located near the Medusae Fossae Formation. The upper mound of Mt. Sharp has been proposed to consist of Medusae Fossae Formation materials (Zimbelman & Scheidt, 2012). This supports the hypothesis that the upper mound of Mt. Sharp was deposited as part of a previously more extensive large-scale sedimentary unit. I suggest that the lower mound was deposited either through a local geologic process, such as lacustrine deposition, or through the more widespread process of ice and dust deposition during high obliquities. If the Arabia Terra deposits (located on the global dichotomy, just as Gale crater is) were created by ice and dust accumulation during periods of high obliquity, so too could Mt. Sharp's lower mound. However, recent results from the Mars Science Laboratory support the hypothesis that Gale crater contains lacustrine deposits (Grotzinger, 2013). Therefore, I propose a history of Gale crater similar to what was proposed in Thomson *et al.* (2011). 1) An impact created Gale crater. 2) Either a local process (such as lacustrine) or regional process (such as ice and dust accumulation) deposited the lower mound. 3) Deposition ceased and some erosion occurred (creating the erosional unconformity observed in the lower layers of Mt. Sharp by the Curiosity

rover). 4) The Medusae Fossae Formation (and therefore Mt. Sharp's upper mound) is emplaced. 5) Erosion of the Medusae Fossae Formation and of Mt. Sharp occurred.

2.5 Conclusions

Our survey of central mounds addressed many of the questions regarding their origin. A summary of my major results and implications is provided here:

1) Central mounds in large (> 25 km diameter) craters occur across Mars, but primarily in the cratered highlands. Over 60% of mounds are located in Arabia Terra.

2) The majority of central mounds are located near a large-scale sedimentary deposit. Therefore, in this study I discuss the implications of the hypothesis that central mounds are remnants of previously more extensive large-scale sedimentary deposits. With this constraint, I find that groundwater upwelling is a possible formation mechanism for the mounds in Arabia Terra, explosive volcanism is a possible formation mechanism for the mounds near the Medusae Fossae formation, and ice-related processes are a possible formation mechanism for most central mounds. I also discuss the possibility that central mounds could be related to the large-scale sedimentary deposits without being continuous with them, as a result of, for example, microclimates preferentially causing the deposition of ice within craters.

3) Most mounds are offset away from the center of their host crater. The mounds in Arabia Terra and near the north pole are offset to the western side of their host crater. These offsets correspond to the prevailing wind direction in those regions, which implies that wind is the primary eroding agent for the majority of central mounds.

4) Mounds may have formed throughout much of Mars' history, including recent time periods. Crater counting suggests that the lower mound in Gale crater was emplaced near the Noachian/Hesperian boundary. Some mounds are associated with geologically young or easily erodible terrain (Medusae Fossae Formation and Olympus Mons aureole deposits) that suggest mound formation in the Amazonian.

5) Mt. Sharp in Gale crater is a complex central mound that may require a more complicated model of emplacement than the rest of the global population of mounds. These results are consistent with previous studies that propose that Mt. Sharp's lower mound is lacustrine sediment and that the upper mound is Medusae Fossae Formation sediment, although I cannot yet rule out the possibility that part of the mound was formed from ice-related processes.

This study raised several more questions that I will continue to address. In the future I will investigate the morphology, mineralogy, and composition of individual mounds in order to further distinguish between different local and regional processes for mound origin and erosion.

CHAPTER 3

THEMIS-VIS COLOR AND MORPHOLOGIC INVESTIGATIONS AT GALE CRATER

Gale crater is the landing site of the Mars Science Laboratory rover, Curiosity. Here I present Thermal Emission Imaging System Visible Imaging Subsystem (THEMIS-VIS) mosaics in grayscale and in false color of Gale crater and its surrounding regions. I use these data products to characterize the regional morphology and color variations. I find that the northern crater floor (where the Curiosity rover is located) could be a different part of the local stratigraphy than the rest of the crater floor. Dunes within Gale crater vary in false color composites from blue to purple, and these color differences could be due to dust cover, grain size, and/or composition. The mound is primarily one color (pink/beige), but small blue patches on the mound represent deposits of presumably basaltic sand, which could be eroding out of the mound. Several sedimentary deposits are located in the region surrounding Gale crater, which implies that the geologic processes that created sedimentary deposits within Gale crater likely also contributed to sedimentary deposits outside the crater as well.

3.1 Introduction

The Mars Science Laboratory (MSL) rover *Curiosity* landing site is within Gale Crater, a ~150 km impact crater located near 5°S, 222°W. As the rover explores the northwest sector of the crater, additional studies that include the entire crater and surrounding terrain are needed to provide the regional context of the *Curiosity* landing

site. Studies characterizing the regional mineralogy, morphology, and albedo have previously been conducted to support the rover scale investigations. While visible color data products from the High Resolution Imaging Science Experiment (HiRISE; McEwen *et al.*, 2007, Delamere *et al.*, 2010) have been used to extensively study the landing ellipse, the small areal coverage of the color portions of these high resolution products have limited the ability to provide regional color context.

The Thermal Emission Imaging System (THEMIS; Christensen *et al.*, 2004) is a multispectral imager on the Mars Odyssey spacecraft with a ten-band mid-infrared uncooled microbolometer array and a five-band visible and near-infrared (NIR) interline transfer CCD imager. The visible/NIR camera, the Visible Imaging Subsystem (THEMIS-VIS), has a resolution of up to 18 m/pix and five filters with band centers located at 425, 540, 654, 749, and 860 nm, although the 860 nm band is contaminated by stray light, and is thus rarely acquired.

In this paper I present the first regional color mosaic of Gale crater using THEMIS-VIS images. Additionally, I present a grayscale mosaic of THEMIS-VIS band 3 (654 nm) radiance images. Using these regional mosaics I can interpret morphologic and color units within and surrounding Gale crater.

3.2 Background

THEMIS-VIS has not previously been extensively used to study the spectral properties of Gale crater. Typically, Mars Reconnaissance Orbiter High Resolution Imaging Science Experiment (HiRISE; Delamere *et al.*, 2007) and Context Camera (CTX; Malin *et al.*, 2007) images have been used for morphologic analyses. Both these

datasets have a higher resolution than THEMIS-VIS (~25 cm/pix and ~6 m/pix, respectively, compared to 18-72 m/pix; Delamere *et al.*, 2007, Malin *et al.*, 2007). However, Odyssey orbits Mars at a different local time than MRO. MRO's orbit is such that CTX and HiRISE images are taken in the midafternoon. For the first 14 years of the Odyssey mission, THEMIS-VIS images were taken in the late afternoon, but since mid-2015 they have been taken in the early morning due to a shift in the local time of the spacecraft's orbit. The longer shadows present during these times enhances the topographic relief of the scene and provides additional morphological information. Similarly, HiRISE (3 color bands, 6 m/pix) and the Compact Reconnaissance Imaging Spectrometer for Mars (CRISM, hyperspectral, ~18 m/pix; Murchie *et al.*, 2007) data are typically used for color observations of an area of interest. While THEMIS-VIS images do not provide the high spatial and spectral resolution of HiRISE and CRISM, respectively, it does provide similar spatial resolution as a CRISM targeted image while also covering a much larger area than HiRISE color images. Therefore, THEMIS-VIS is an ideal dataset for conducting morphological and multispectral investigations of large areas. Since my region of interest is a large crater (Gale crater, ~150 km in diameter), THEMIS-VIS is an ideal dataset for this study.

In previous work, it has been shown that color variations in THEMIS-VIS multispectral images correlate to the morphology. Bell et al. (2006) found that 633 out of 7923 THEMIS-VIS multispectral images met this "most interesting" criteria. The authors also divided these interesting images into several categories, such as color variations within layered terrain, wind and slope streaks, "blue" terrain (including sand dunes), and channels or valleys (Bell, 2008).

Gale crater was selected as the *Curiosity* rover's landing site partially because aqueous mineral signatures were identified from orbit and because of the 5 km tall pile of layered sediment in the center of the crater (Milliken *et al.,* 2010). Gale's central mound, Mt. Sharp, was first described as a sedimentary deposit by Malin and Edgett (2000), but its formation mechanism is still unknown. Central mounds are hypothesized to have been created by either subaerial or subaqueous processes through one of two general formation mechanisms. The prevailing hypothesis suggests that after their craters were formed, sediment filled the entire crater and was later eroded into the morphologies observed today (*i.e.*, Malin & Edgett, 2000; Bennett & Bell, 2016). Alternatively, the sediment could have been deposited as the features observed today without any significant erosion contributing to their mound shape (Kite *et al.*, 2013).

There have been many other studies utilizing orbital observations of Gale. Anderson & Bell (2010) conducted an overview study of Gale crater. The authors identified channels in the crater rim but no outlet channels, sinuous ridges and polygonal ridges on the crater floor, and layers that are traceable for more than 10 km in the central mound. Milliken *et al.* (2010) proposed that the layers in the central mound could represent a record of the changing paleoclimate of Mars. The authors used CRISM observations to identify hydrated minerals and suggested that the martian climate changed from a climate favorable to clay mineral formation to one that is more favorable to the formation of sulfates and salts. Thompson *et al.* (2011) used crater counts to constrain the timescale of deposition of the central mound's Lower formation to near the Early Hesperian/Late Noachian boundary. Lane and Christensen (2013) used thermal infrared spectra from THEMIS and the Mars Global Surveyor Thermal Emission

Spectrometer (Christensen *et al.*, 2001) to determine the olivine composition of basaltic dunes on the crater floor. Hobbs *et al.* (2010) characterized the various dune fields present on the floor of Gale crater and created a thermal inertia grain size map of the crater. The authors found that wind played and continues to play a major role in shaping the features in Gale crater. Le Diet *et al.* (2013) studied the morphology and stratigraphy of the sedimentary deposits within Gale crater and created a detailed geologic map to detangle the sequence of infilling of Gale crater. The authors propose that the central mound was created via airfall of fine grained sediment (dust, volcanic ash, or snow) and that a paleolake existed in Gale crater in a permafrost environment after the mound had already mostly formed. Grotzinger *et al.* (2014) used *Curiosity* rover data to show that there was once water present in Gale crater in the form of a fluvio-lacustrine environment.

3.3 Methods

Gale crater was selected as the MSL landing site in July 2011. At that time, the THEMIS team began targeting Gale and the surrounding area with the goal of acquiring full areal coverage of multi-spectral THEMIS-VIS observations at 36 m/pix resolution. In July 2011, there were 9 multi-spectral THEMIS-VIS images over Gale crater. As of June 2016, there are 115 multi-spectral images, which represents ~70% areal coverage of the target area and ~90% coverage of the crater interior.

The THEMIS team also aimed to acquire full areal coverage of Gale crater in Band 3 (red, 654nm) at 18 m/pix in order to produce a higher-resolution basemap at the same local time for the 36m/pix multi-spectral images. In April 2012, there were 129

Band 3 images of Gale Crater and the surrounding area, representing ~90% areal coverage. Then, prior to MSL's landing, a Band 3 contrast-stretched radiance mosaic of Gale Crater was generated using the images available at that time. The remaining gaps in Band 3 coverage were filled using CTX images resampled at 18m/pix. Although the CTX images were acquired at slightly earlier local times, they blended well with the THEMIS-VIS Band 3 images and helped to create a nearly seamless basemap of Gale Crater.

The methods of McConnochie *et al.* (2006) were used to calibrate each THEMIS-VIS image and the methods of Edwards *et al.* (2011) were used to create the Band 3 (red) and color mosaics. In both cases, the VIS images were first map-projected using the U.S. Geological Survey's Integrated Software for Imagers and Spectrometers 3 (ISIS3). For the Band 3 images, the radiance data was contrast stretched using a sigma stretching algorithm. For the multi-band images, bands 4/2/1 (749/540/425 nm) were linearly stretched and assigned to the RGB channels of a false-color image, respectively, following the same process used to generate the standard THEMIS-VIS multiband RGB products (Murray *et. al*, 2016). The images were then mosaicked using the mosaicking process and blending algorithms described by Edwards *et al.* (2011).

THEMIS-VIS images have been previously noted to contain artifacts as a result of stray light (McConnochie *et al.*, 2006). In this work I have reduced the effect of these artifacts by manually setting the values of the affected pixels to a null value and by not using severely affected images when multiple images were available over one area. Where many images exist (*e.g.*, over the MSL landing site and the central mound) I created smaller, local mosaics and I deleted almost all instances of instrument artifacts.

Band 3 is usually the least affected by stray light, which is why it is used for the single-band grayscale morphology mosaic.

To gain additional insight into the variations observed in the THEMIS-VIS mosaics, THEMIS-IR decorrelation-stretch (DCS) mosaics were also generated. *Lane and Christensen* (2013) previously used THEMIS DCS images using bands 8, 7, and 5 to examine the olivine composition of the basaltic dunes in Gale Crater. I expanded on that work using high-quality mosaics of multiple DCS band combinations. The DCS methods of Edwards *et al.* (2011) were used to perform the decorrelation stretches on high-quality 10-band THEMIS-IR images utilizing the standard THEMIS DCS band combinations of 8/7/5, 9/6/4 and 6/4/2. The individual images were then manually co-registered to reduce misalignments and the mosaicking methods of Edwards *et al.* (2011) were used to create seamless mosaics in all three DCS band combinations.

We also compare the THEMIS-VIS multispectral mosaic with a TES derived dust cover index. I created the TES dust index map by using the JMARS geographic information system (Christensen *et al.*, 2009) and a set of parameters for TES developed by Ruff & Christensen (2002) to estimate the amount of dust present on the surface.

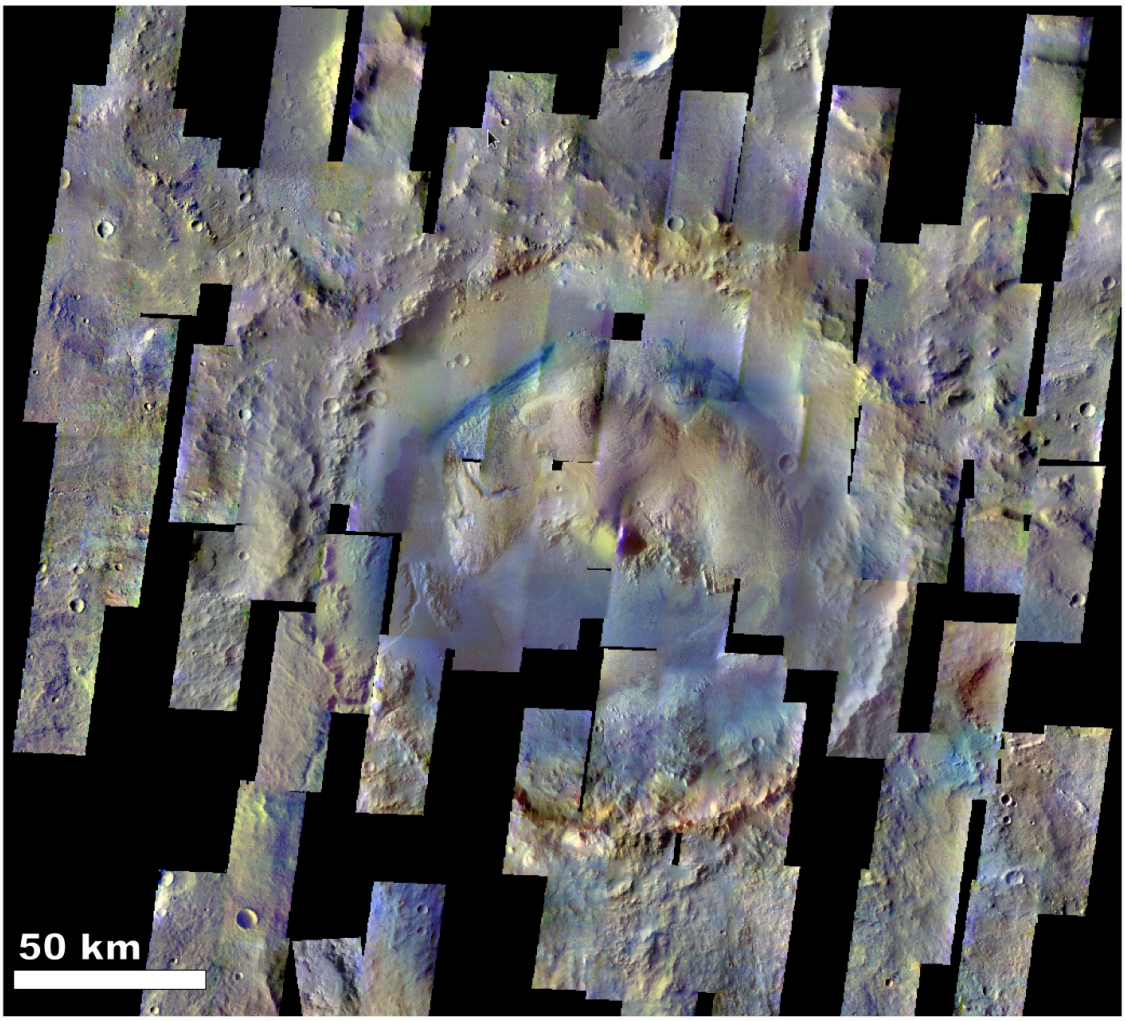

Figure 3.1 THEMIS-VIS band 4/2/1 color mosaic of Gale crater

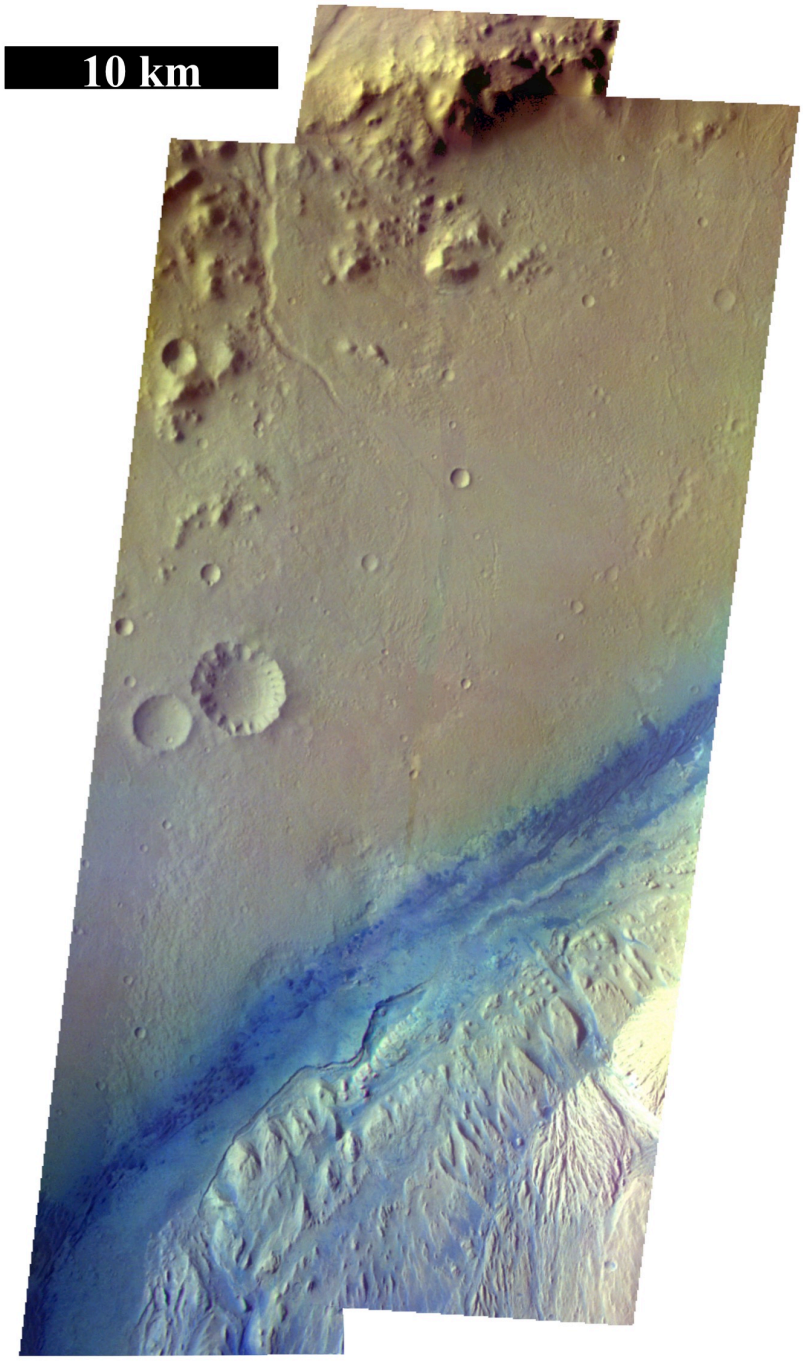

Figure 3.2 THEMIS-VIS color mosaic of MSL traverse area. This area has repeat coverage and most artifacts were removed without creating large gaps in the mosaic. (THEMIS-VIS images V52340002, V46072001, and V47183002)

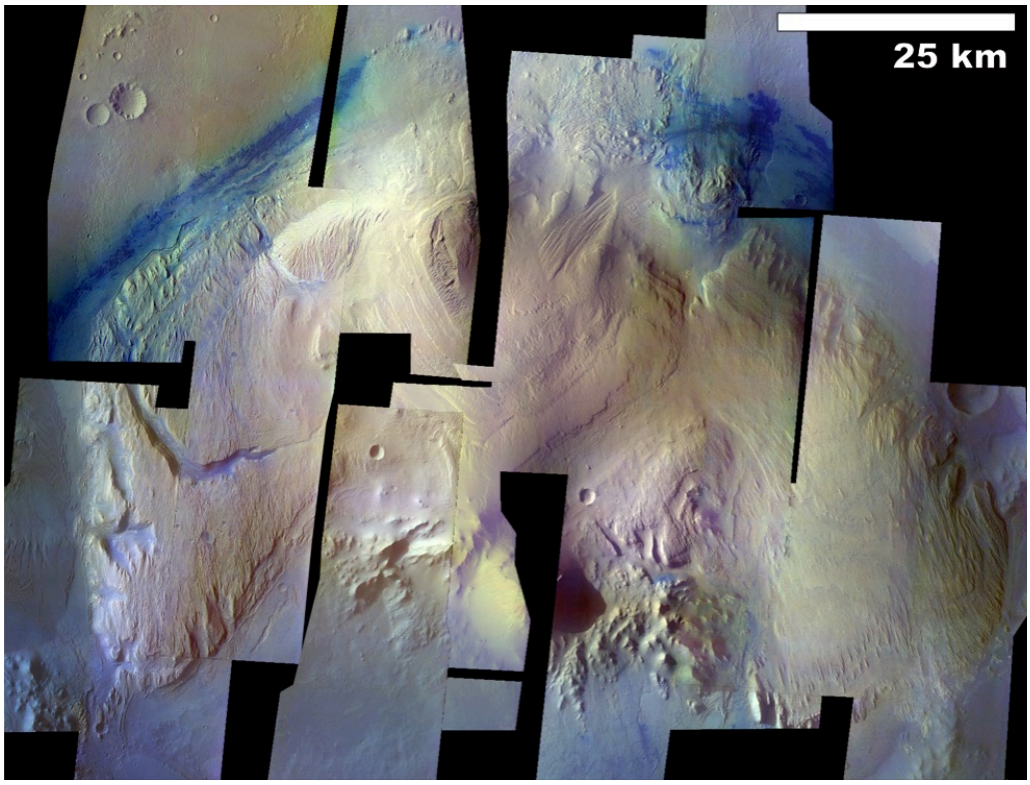

Figure 3.3 THEMIS-VIS color mosaic of Mt. Sharp. I removed most of the artifacts from this mosaic, which left many gaps.

3.4 Results

3.4.1 Regional Color Map

The THEMIS-VIS color mosaic of Gale crater and the surrounding area is shown in Figure 3.1. There are multiple false color units within the mosaic, including the gray crater exterior and the beige or light pink central mound. The largest color variations in the region occur in the dunes, which range from purple to blue.

The false color mosaic of the MSL traverse area (Figure 3.2) reveals that the mound is pink/white, the dunes are blue, the hematite ridge is white, crater wall is gold, and the fan is pink. There is also a color difference in the crater floor in the western portion of the mosaic. The crater floor transitions from white/yellow to darker pink across two units. The darker pink unit appears to be smoother and overlies the rough white/yellow unit.

The mound exhibits a mostly uniform color. Figure 3.3 shows that the mound is pink to beige (the residual green areas are likely artifacts due to stray light). This uniform color trend continues from the upper to the lower mound. In some locations, small blue patches are observed on the mound (Figure 3.4b). HiRISE images reveal that these are small accumulations of sand (Figure 3.4c and d).

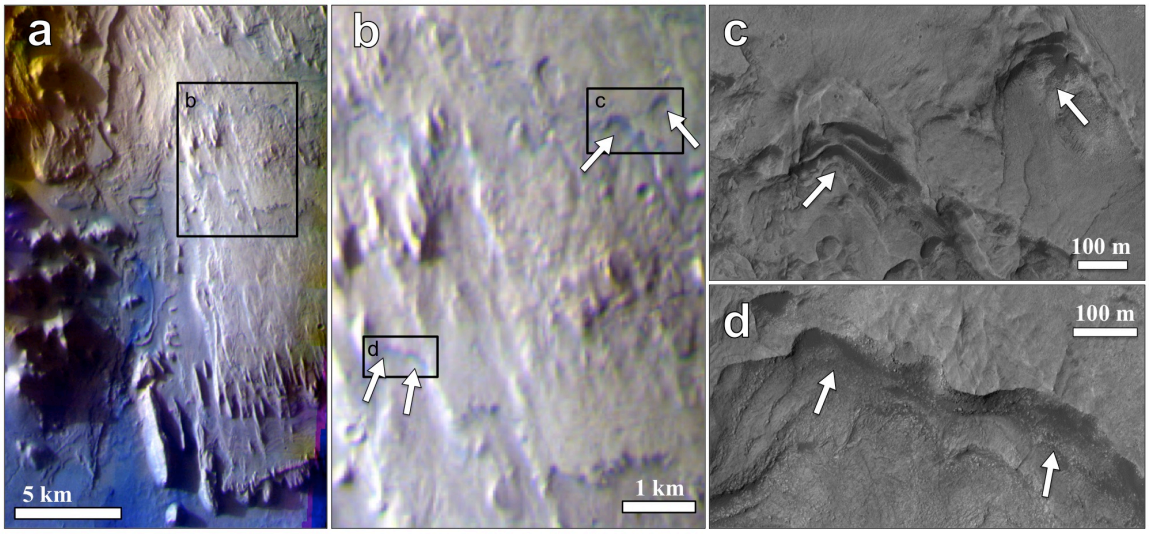

Figure 3.4 a) THEMIS-VIS image of the southwest part of the central mound. b) Subsection of the same THEMIS-VIS image with small blue patches on the mound highlighted. The arrows in (b) point to the same features as the arrows in (c) and (d). c) and d) HiRISE images showing sand patches on the central mound where THEMIS-VIS showed small blue patches. (THEMIS-VIS image V19603003 and HiRISE images PSP_001897_1745_RED and ESP_018999_1745_RED)

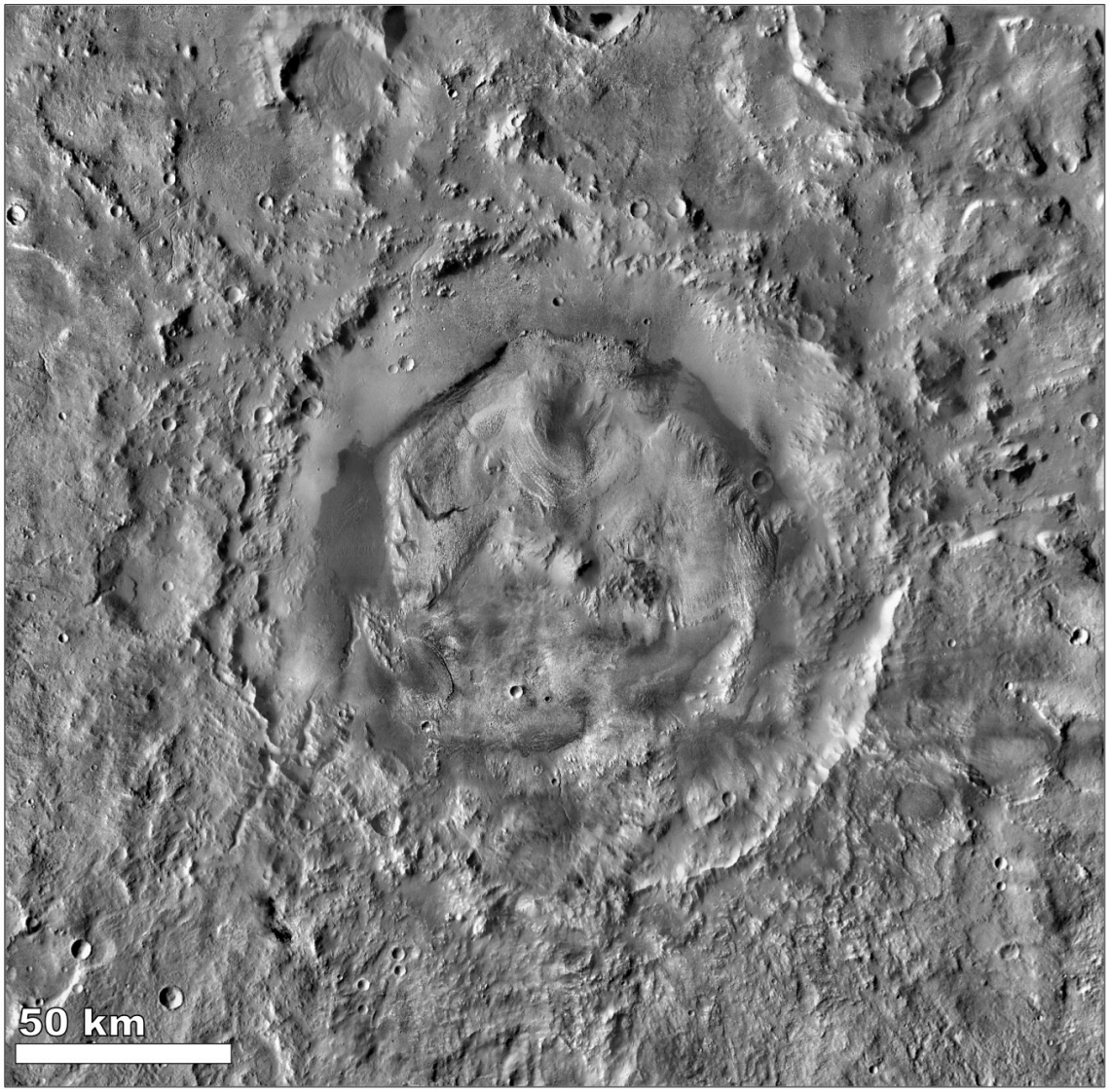

Figure 3.5 THEMIS-VIS band 3 mosaic of Gale crater

3.4.2 Regional morphology with THEMIS-VIS band 3 mosaic

The THEMIS-VIS Band 3 mosaic is shown in Figure 3.5. One of the most noticeable differences between the THEMIS-VIS mosaic and other visible mosaics (i.e. CTX as shown in Anderson & Bell, 2010 and Le Deit *et al.*, 2013) is the lack of an observable wind tail to the south of Gale in THEMIS-VIS Band 3 data.

Much of the crater interior has already been described using CTX images (i.e. Anderson & Bell, 2010 and Le Deit et al., 2013), especially the area around the MSL landing site. Figure 3.6 shows the northern part of the crater, including the MSL landing site. The enhanced morphology visible in THEMIS-VIS images due to the later local time shows that this northern part of the crater has a unique, rough texture and contains many lobate features and sinuous ridges. This morphology abruptly changes to a smooth texture both to the east and west (see arrows in Figure 3.6). THEMIS-VIS Band 3 is also valuable in the southern part of the crater (Figure 3.7). This area is within the low albedo wind tail and is very dark and difficult to resolve details in CTX mosaics. In the THEMIS-VIS grayscale mosaic of this area, many albedo and textural variations are observed.

Just as there are many sedimentary deposits within Gale crater, there are many examples of sedimentary deposits in the surrounding area. This mosaic covers more area than previous visible mosaics. In addition to previously described channel features, I identified instances of layered sedimentary deposits (Figure 3.8), additional channels (Figure 3.8), (with HiRISE images) small-scale fractures (Figure 3.9), and potential deltaic landforms (Figure 3.10).

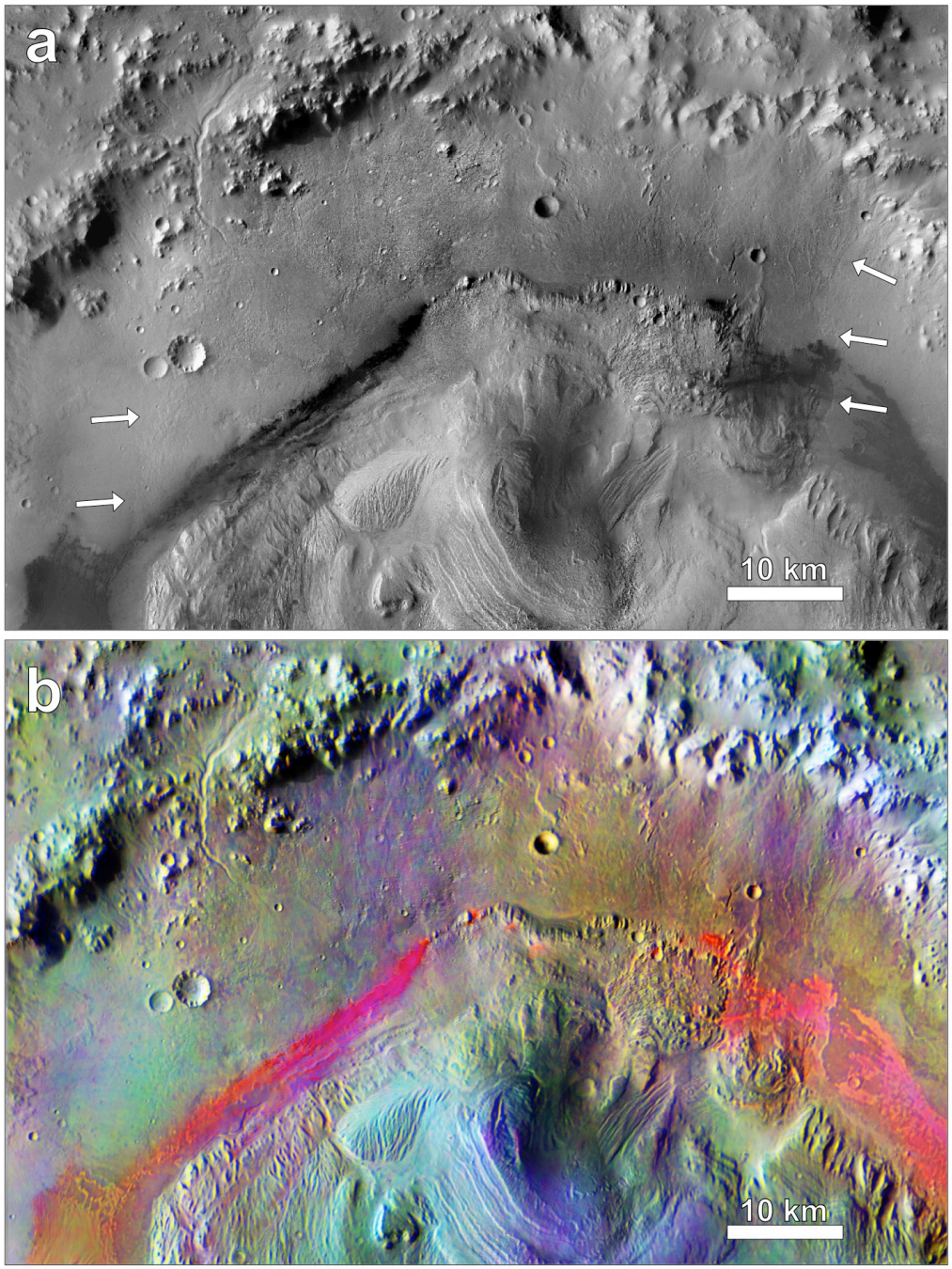

Figure 3.6 a) THEMIS-VIS band 3 mosaic of the northern portion of Gale crater. The arrows point to the contacts where the morphology transitions from rough (containing lobate features and sinuous ridges) to a smoother morphology. b) Figure 3.6a overlain by the THEMIS DCS mosaic bands 8/7/5.

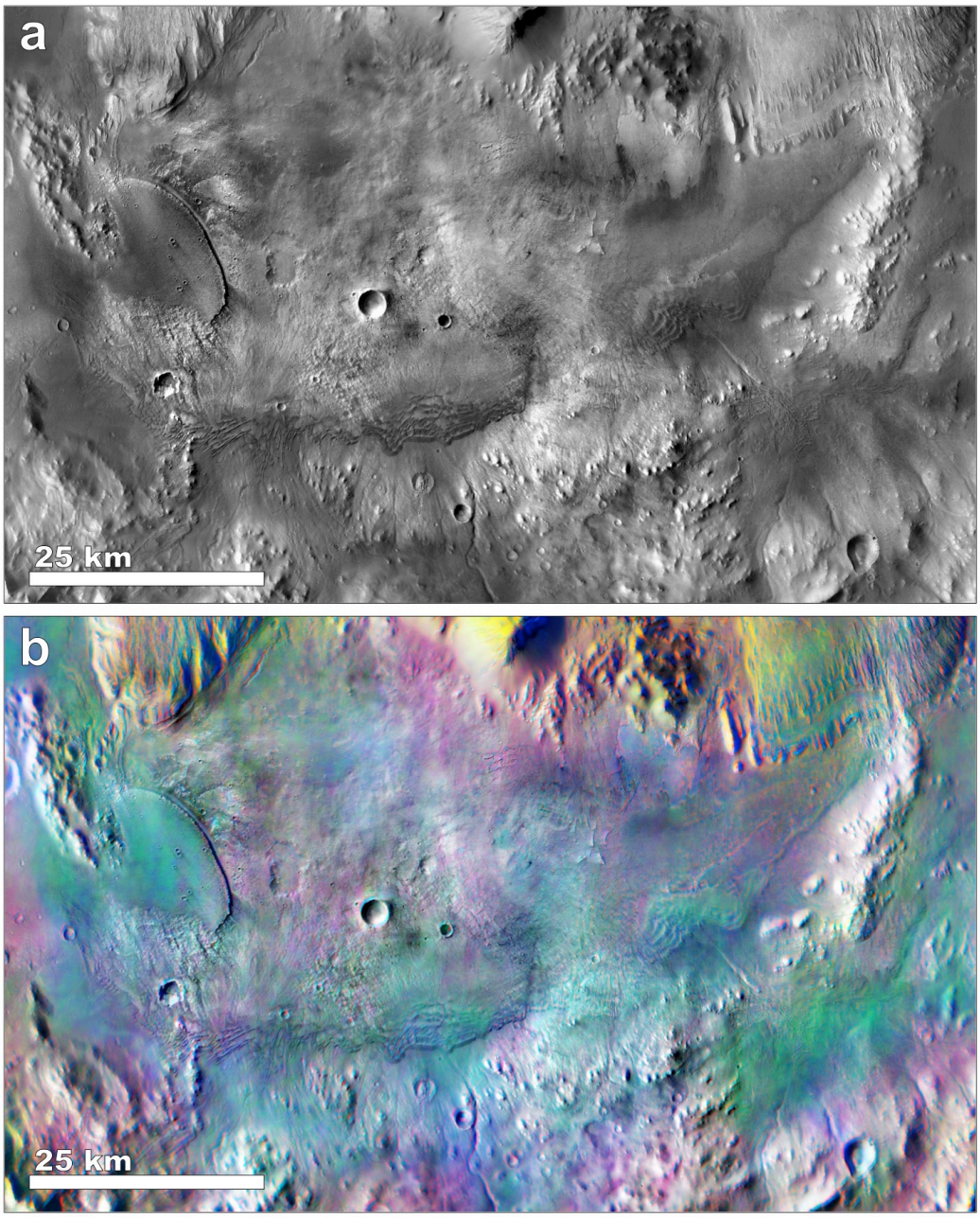

Figure 3.7 a) THEMIS-VIS Band 3 mosaic of the southern portion of Gale crater. THEMIS-VIS provides better contrast and details of this area than CTX due to longer shadows at the later local time. This area is dominated by sand and is a part of the low albedo wind tail that extends south of Gale crater. b) Figure 3.7a overlain by the THEMIS DCS mosaic bands 6/4/2.

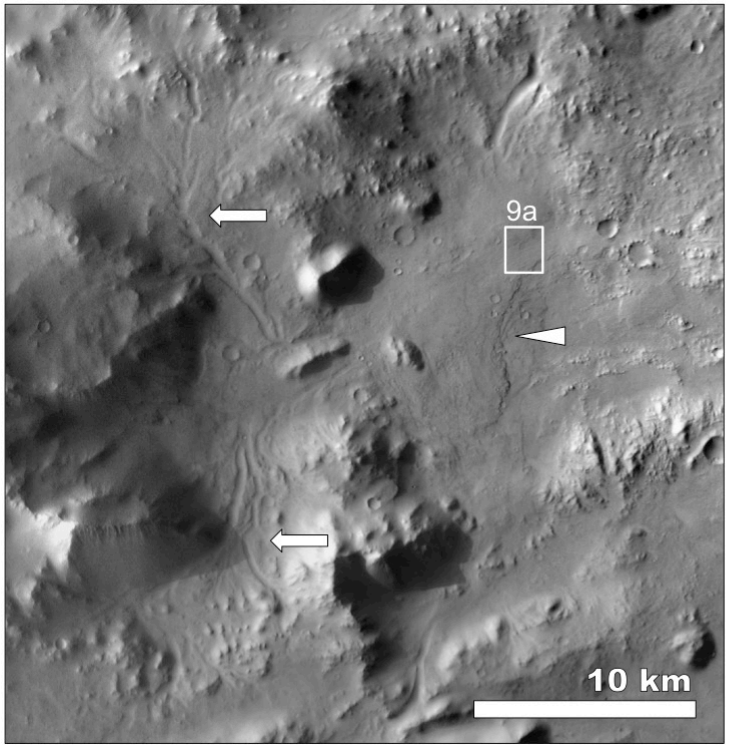

Figure 3.8 THEMIS-VIS band 3 of an area to the east of Gale crater. The arrows point to the largest channels in this area. The triangle points to layered sediment within a local depression. The box shows the location of Figure 3.9a.

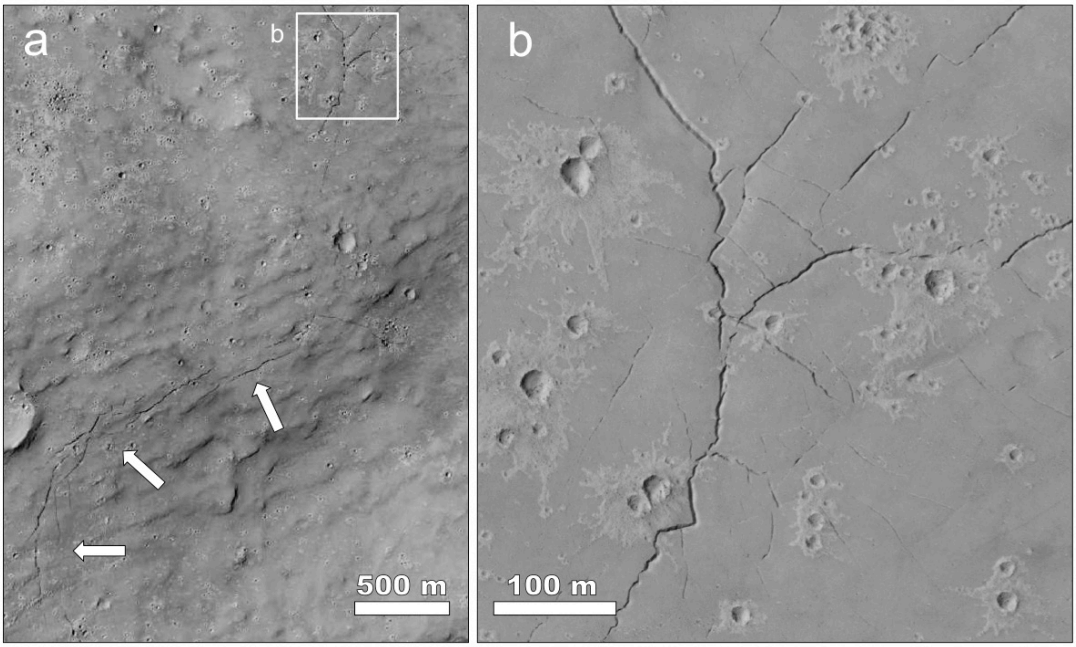

Figure 3.9 HiRISE image ESP_025447_1755_RED , see context in Figure 3.8. Examples of fractures or cracks and craters with unusual ejecta blankets that occur in this small area. Arrows highlight the location of an arcuate crack.

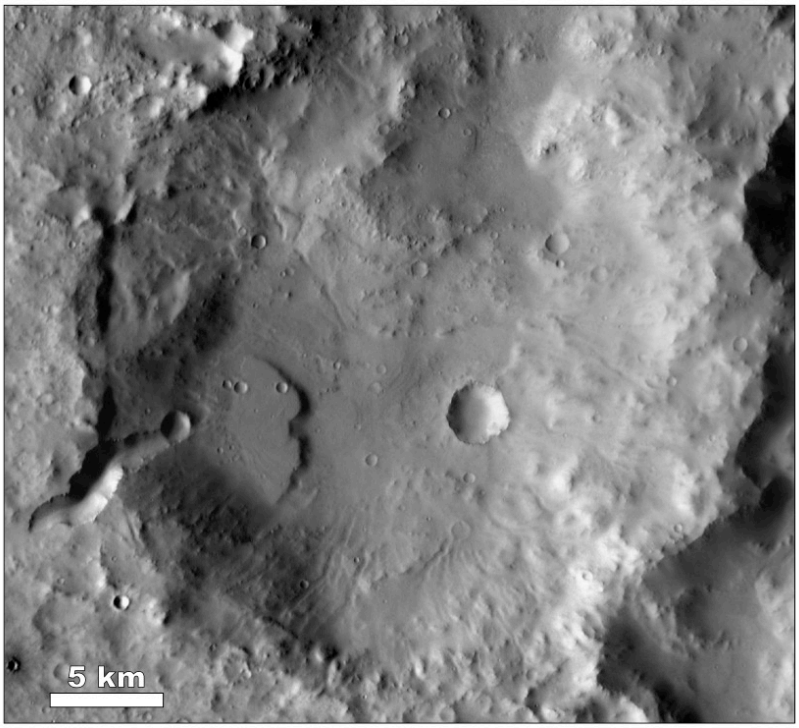

Figure 3.10 THEMIS-VIS Band 3 mosaic. A channel and deltaic feature in a crater located to the west of Gale crater.

3.4.3 THEMIS DCS mosaics

The THEMIS DCS mosaics of Gale crater and the surrounding region are shown in Figure 3.11. There are no major variations visible in the crater exterior in all three mosaics. The crater interior exhibits variations that differ between the three mosaics. The 9/6/4 DCS mosaic (Figure 3.11b) shows the least amount of variation. The major false color variation emphasizes differences between the mound (green) and the crater floor (pink). In the 8/7/5 DCS mosaic (Figure 3.11a) the dunes within Gale crater range from bright pink to gold and the upper and lower mounds exhibit different colors (blue and green, respectively). Figure 6b shows the 8/7/5 DCS mosaic overlain on the THEMIS-VIS band 3 grayscale mosaic in the northern part of Gale crater. Some morphology variations in the northern part of Gale crater match the variations observed in the DCS mosaic. The 6/4/2 DCS mosaic (Figure 3.11c) shows many variations within Gale crater. Dunes in this mosaic are blue toned, but range from cyan to purple to teal. The upper and lower mound are different colors (yellow and pink, respectively). Figure 3.7b shows the 6/4/2 DCS mosaic overlain on the THEMIS-VIS band 3 grayscale mosaic in the southern part of Gale crater. This figure shows that the southern portion of Gale crater exhibits many variations in albedo, morphology, and DCS colors.

3.4.4 TES dust cover

The TES dust cover index map is shown in Figure 3.12. The largest apparent variations of dust in Gale crater are primarily related to the wind tail that begins within the southern part of Gale crater and extends south beyond the crater wall. Areas within the wind tail generally have less dust cover than areas outside of the wind tail.

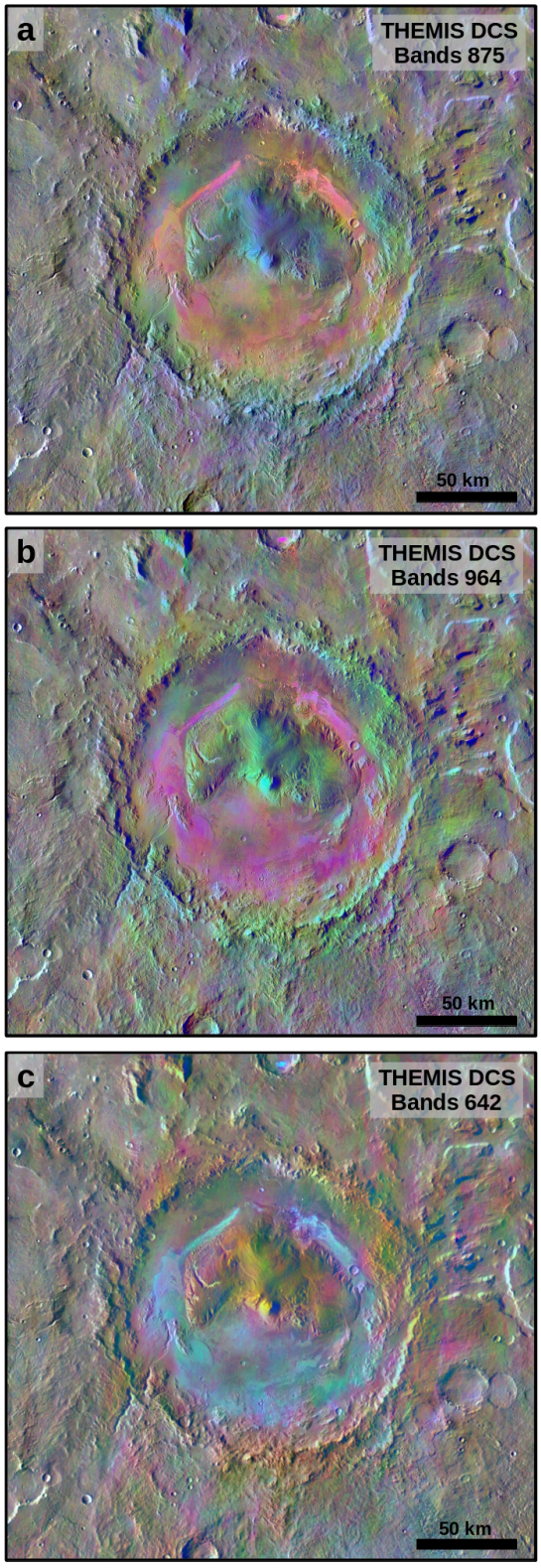

Figure 3.11 THEMIS decorrelation stretch mosaics of Gale crater. These mosaics emphasize spectral differences. a) Bands 8, 7, and 5 were projected as red, green and blue, respectively. Bands (b) 9/6/4 and (c) 6/4/2 were projected as red, green and blue, respectively.

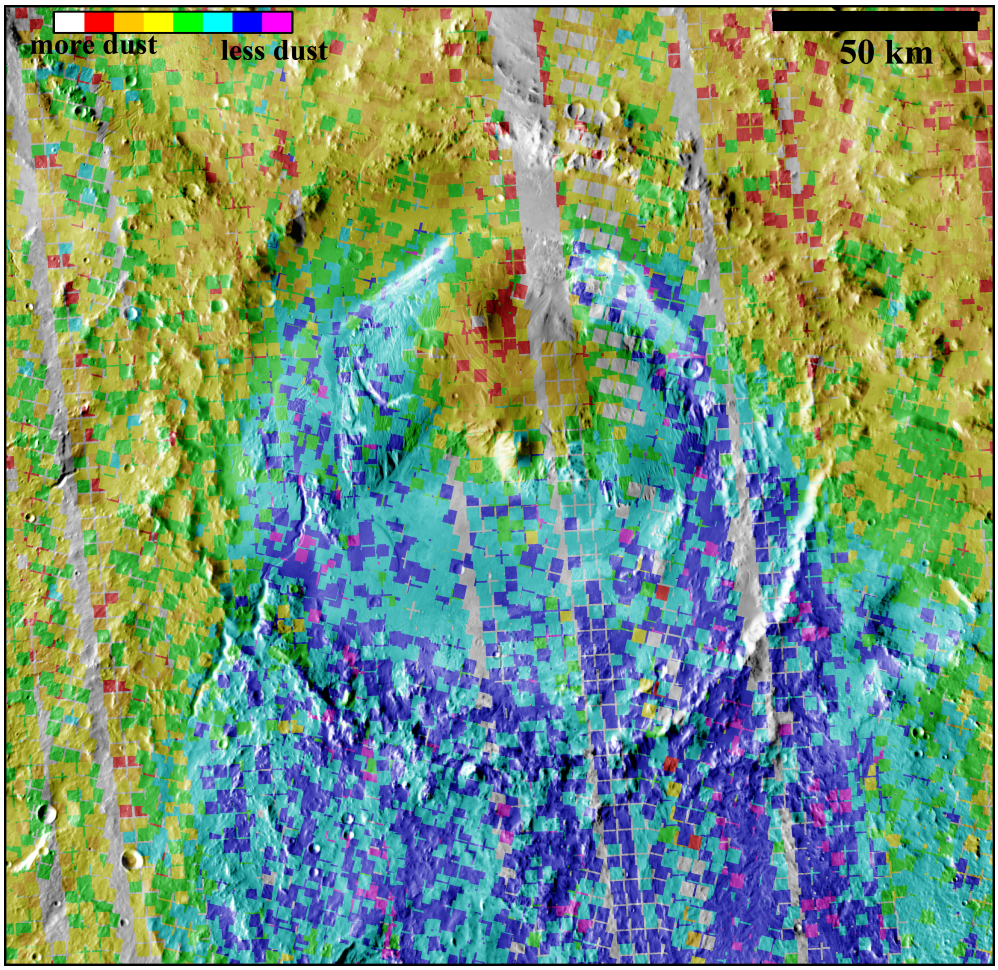

Figure 3.12 TES dust cover over THEMIS Day IR. (conducted in JMARS; Ruff & Christensen (2002))

3.5 Discussion

It is important to note that although I minimized the effects of instrument artifacts in the THEMIS-VIS color mosaicking process (Figures 3.1 to 3.3), they are still present. These artifacts primarily manifest as green or purple streaks along the left and right edges of image segments that went into the mosaic. I keep this in mind to avoid misinterpreting the color variations within the mosaic.

3.5.1 Crater Interior

Using THEMIS-VIS mosaics I can make observations and interpretations regarding the crater interior; specifically the crater floor, sand dunes, and central mound. Gale crater is a sedimentary environment, as demonstrated by the *Curiosity* rover images taken while driving through many distinct bedforms. While THEMIS-VIS cannot help at such a local scale, I can identify larger units that are different colors or textures to contribute to mapping the rest of the crater floor. One result from this study was that the color and texture of the crater floor near the MSL landing and traverse sites is unique to this area in the northern part of the crater. There are two sharp boundaries to the east and west of the MSL area where the texture changes from rough to smooth (Figure 3.6). There is also a color change (white/beige to dark pink) associated with the western boundary (Figure 3.2). I interpret these sharp boundaries to be the contact between different units. This is consistent with the geologic map of Gale crater presented in Le Deit *et al.* (2013). The authors include the western contact (Figure 3.6) in the geologic map of Gale crater as a boundary between two crater floor units. My mosaics show that the smooth, pink unit appears to overlie the rough, beige MSL area. This implies that

MSL is investigating a layer that is stratigraphically lower than the rest of the crater floor. The color variations in the 8/7/5 DCS mosaic (Figure 3.6b) also match this trend, with purple to green/yellow colors occurring primarily in the northern half of the crater and sharp color change at the eastern boundary. I observed that the area near MSL has a unique color and texture as compared to the rest of the crater floor, but I also note that much of the rest of the crater floor is covered by sand dunes and is not visible. The 6/4/2 THEMIS DCS mosaic addresses this point. In this mosaic the northern crater floor is green and pink while much of the southern crater floor is blue-toned basaltic sand. However, the southern crater floor exhibits local blue-toned variations (blue-purple-teal) in the 6/4/2 THEMIS DCS mosaic that match the albedo and morphology variations observed in the THEMIS-VIS band 3 grayscale mosaic (Figure 3.7b). The dunes that cover some of the southern crater floor contribute to the observed variations, but there are also likely variations due to the crater floor itself that are due to either the texture, grain size or composition.

In the THEMIS-VIS false color mosaic, sand dunes on the crater floor dunes vary from blue to purple. To some extent this is likely an artifact of the mosaicking process as the change from blue to purple tends to occur across image boundaries. However, other datasets also show differences between the dune fields within Gale crater. THEMIS DCS mosaics also show variations between the dunes near MSL and the sand sea to the west (Lane, 2013; Figure 3.11). In the 8/7/5 DCS mosaic, the MSL dunes are pink whereas the sand sea is gold, and in the 6/4/2 DCS mosaic the MSL dunes are cyan whereas the sand sea is purple. Thermal inertia values from Hobbs *et al.* (2010) also reveal a difference between the dunes near MSL and the sand sea to the west of the mound. Those authors

found that the dunes near MSL had a thermal inertia between 530 and 740 and categorized them as granule- to pebble-sized. The sand sea had thermal inertia between 330 and 430 and was categorized as coarse sand. The thermal inertia and grain size differences could also be reflected in the albedo variations between the dune fields. The albedo difference between the Bagnold dunes and the sand sea are not likely due to different levels of dust cover. The TES dust cover index (Figure 3.10) shows that the sand sea is within the wind tail, and therefore is less dusty than the Bagnold dunes. Dust increases the albedo (and makes features redder) of martian surfaces, so if dust cover is the cause of the albedo variations, the more dusty Bagnold dunes would have a higher albedo and would be more red/purple. However, I see that the opposite is true. The Bagnold dunes are bluer than the sand sea. Finally, the albedo variations could be related to differences in composition. The observed color variations between dune fields in the THEMIS DCS mosaics are consistent with this possibility.

This study has confirmed the results of previous studies in that the central mound, Mt. Sharp, is spectrally uniform at both THEMIS-VIS and THEMIS-IR wavelengths. The uniform color could be due to dust cover. However, the dust cover on the mound likely varies because the TES dust cover index (Figure 3.11) shows that the upper mound is more dusty than the lower mound. The 8/7/5 and 6/4/2 THEMIS DCS mosaics also exhibit color differences between the upper and lower mound, which implies there are thermophysical variations. The 9/6/4 THEMIS DCS mosaic does not exhibit a major difference between the upper and lower mound. Instead, this mosaic emphasizes the difference between the mound and the crater floor, which is likely due to a combination of different composition, grain size and dust cover. The crater floor is covered in basaltic

sand which contains large grains and less dust whereas the mound is likely fine grained and dust covered. One new result from this study is that the small blue color variations that occur in THEMIS-VIS color images on the mound (Figure 3.4) are due to small outcrops of sand. Sand could have been deposited on the mound from elsewhere, possibly transported upslope by diurnal winds. Alternatively, the sand could be eroding out of the mound and collecting in local topographic lows or in locations that are sheltered from the wind. Explosive volcanic deposits can exhibit these characteristics (fine grained, layered material, with sand-sized particles that weather out).

3.5.2 Crater Exterior

The plains surrounding Gale crater are gray in the THEMIS-VIS color mosaic (Figure 3.1). There are no major variations in color, but there are interesting morphologic variations. For example, using the THEMIS-VIS Band 3 grayscale mosaic I identified a potential fan-shaped deltaic feature, layered sedimentary deposits, channels, and small-scale fractures. The feature is located in a small crater to the west of Gale crater (Figure 3.10). The fan-shaped deposit and its channel are located in the southwest part of the crater, which corresponds to the same part of the crater where the largest channel (and corresponding fan/deltaic feature) is located in Gale crater (Anderson & Bell, 2010). This suggests that the same geologic processes affected both Gale crater and the smaller western crater and produced channels with sedimentary deposits on both crater floors.

Figures 3.8 and 3.9 show a layered sedimentary deposit in a topographic depression with channels leading into the depression and fractures cutting across a portion of the layered deposits. The fractures are formed in a mantling layer on top of the

layered sedimentary deposits. The mantling unit is apparent in Figure 3.9a, where linear features (likely part of the layered sedimentary deposit) are visible but muted by a mantling material. This mantle is only visible in a small area. This area contains many fractures and craters with unique ejecta blankets. The fractures were likely created when the underlying sedimentary deposit settled, and the mantling layer cracked from the resulting stress. The unique crater ejecta blankets were formed when a bolide punched through the mantling layer and ejected material on top of the mantling unit.

In general, I identified many sedimentary deposits and channels in the area surrounding Gale crater. These features suggest that the geologic processes that created the sedimentary deposits within Gale crater were not limited to the crater interior. Either sediment once filled and overtopped Gale crater, allowing the processes at work to affect the surrounding plains, or the geologic process preferentially affected local topographic lows, which is where most sedimentary deposits were identified. This could imply that central mound formation mechanisms that take place entirely within the crater (i.e. slope winds from the crater walls; Kite *et al.*, 2013) are not feasible. Alternatively, the sedimentary deposits in the area surrounding Gale crater could have resulted from a geologic process that occurred after the mound was formed. For example, Le Deit *et al.* (2013) proposed that a lake existed on Gale's crater floor after the mound was partially formed. Late staged water-related processes could have affected both the crater interior and exterior and deposited lacustrine materials within Gale and other sedimentary deposits in the area surrounding the crater.

3.5.3 Dust coverage

One question that arises regarding albedo measurements is whether THEMIS-VIS images (both Band 3 and multispectral) are directly correlated with dust cover. To address this, I used the TES dust cover index to constrain the amount of dust in and around Gale crater. Figure 3.11 shows that the primary variation in dust cover around Gale crater is related to the wind tail that begins within the crater and extends south of the crater. There is less dust within the wind tail. The THEMIS-VIS band 3 grayscale mosaic does not show any evidence of a wind tail. This is in contrast to other albedo products (such as CTX) that show the main albedo variations are related to dust and wind tails. When comparing the TES dust cover map to the THEMIS-VIS color mosaic, there are two major differences. First, in the THEMIS-VIS color mosaic (as in THEMIS-VIS band 3 grayscale mosaic) there is no noticeable wind tail. The area to the north of Gale crater is very similar in color to the area south of the crater although they exhibit different dust cover levels. Second, the northern crater floor is a different color (yellow/pink) than the southern crater floor (blue/purple). This could be related to dust cover. However, the upper mound has more dust cover than the lower mound, but they both exhibit similar colors in THEMIS-VIS. This implies that THEMIS-VIS color mosaics can be affected by dust cover, but is not directly controlled by it. THEMIS-VIS mosaics should not be used as a higher resolution proxy for the TES dust cover index.

3.6 Conclusions

In this study I have shown that THEMIS-VIS data products are useful for the characterization of regional color and morphology variations within Gale crater, as well

as providing context for finding locations to investigate further with higher resolution multi-spectral datasets (such as HiRISE + CRISM). In contrast to CTX mosaics that primarily show albedo differences due to dust cover, such as wind tails, the THEMIS-VIS band 3 grayscale mosaic reveals more details about the morphology, including different textures, due to the images being acquired at later local times. The combination of the higher resolution of the THEMIS-VIS band 3 grayscale mosaic with the thermophysical information from the THEMIS IR DCS mosaics is a powerful data product. Using the color and grayscale THEMIS-VIS mosaics as well as the THEMIS-IR DCS mosaics, I found that the crater floor near MSL may be a different part of the local stratigraphy than the rest of the crater floor. Also, dunes within Gale crater vary in false color composites from blue to purple, and these color differences may be due to dust cover, grain size, or composition. The mound is primarily one color (pink/beige) in the THEMIS-VIS color mosaic, but the upper and lower mound exhibit different levels of dust cover amounts and different colors in the THEMIS-IR DCS mosaics. Small blue patches on the mound represent deposits of presumably basaltic sand, which may be eroding out of the mound. Finally, I identified several sedimentary deposits in the region surrounding Gale crater, which implies that the geologic processes that created sedimentary deposits within Gale crater likely also contributed to sedimentary deposits outside the crater as well.

CHAPTER 4

THE ALBEDO OF MARTIAN DUNES: INSIGHTS INTO AEOLIAN ACTIVITY AND DUST DEVIL FORMATION

Wind is the primary geologic process currently active on the surface of Mars. Albedo variations at eight dune fields were tested based on the hypothesis that a dune's ripple migration rate is correlated to its albedo. On Mars, where the atmospheric pressure is low, dust is removed from the surface of a dune by saltating sand. Therefore, more active dunes should remove dust more efficiently than less active dunes. A dune's albedo was found to be low in the first half of the Mars year (L_s = 0-180º) and high in the second half (L_s = 180-360º) during the dusty season. Both fast- and slow-moving dunes exhibit low albedos, whereas dunes with intermediate speeds exhibit high albedos. A dune's minimum albedo does not have a simple correlation with its ripple migration rate. Instead, I propose that dust devils remove dust on slow-moving and immobile dunes, whereas saltating sand caused by strong winds removes dust on faster dunes. Albedo should not be used as a proxy for migration rate of dunes, as it may be difficult to distinguish between fast- and slow-moving dunes that have the same albedo. I also propose that albedo variations on a single dune field can reveal insight into the local wind regime.

4.1 Introduction

Aeolian activity is the primary geologic agent currently influencing the surface of Mars. Now that high resolution cameras have been orbiting Mars for decades, evidence

of aeolian activity in the form of mobile ripples and dunes has been identified (Bridges *et al.*, 2011; Silvestro *et al.*, 2010; 2013). Analyzing these mobile bedforms provides one of the very few sources of information about local wind regimes. I investigate an alternative method of tracking the estimated Lambert albedo (hereafter referred to simply as "albedo" for brevity) measurements of dune fields, which may yield information on dune activity and the local wind regime.

4.2 Background

Albedo has been used to study martian sediment transport since the first missions to Mars. Thomas *et al.* (1981) categorized wind streaks on Mars by their albedos, using the assumptions that dust is bright and some sedimentary materials (such as dunes) are dark. The authors speculated that bright wind streaks resulted from the preferential deposition of bright dust, while the dark streaks either resulted from preferential erosion of dust or deposition of dark materials (such as sand). Later studies began to quantify the albedos of bright dust and dark sand dunes. For example, Thomas *et al.* (1989) found the albedo of a dusty region in Arabia Terra to be roughly 0.28 and that the albedo of martian dunes ranged from 0.0903 to 0.127 (± .001). Ruff and Christensen (2002) measured the albedo of a bright region (likely dust covered) in Arabia Terra to be ~0.26 and a dark region (interpreted as an intracrater dune field) to be ~0.12.

The hypothesis that albedo could yield information on dune activity and the local wind regime has been previously proposed. Edgett *et al.* (1997) suggested transverse aeolian ridges (TARs) had higher albedos than large dark dune fields because they were inactive and covered in high albedo dust. This implies that the albedo of a dune can be

correlated to its migration rate. On Mars, sand particles are more easily transported by wind than dust particles. Threshold curves for the minimum wind speed required to move particles of different sizes on Mars, which has a mean atmospheric pressure of ~0.6% that of the Earth, show that sand-sized grains are the particles most easily set in motion (Iversen *et al.*, 1976). Clay and silt sized particles are more difficult to move due to interparticle cohesion, and wind that is strong enough to move such particles is thought to be infrequent on Mars (e.g., Pollack *et al.*, 1976). Dust, the clay-sized grains that settle on top of a dune field, will likely not be directly removed by wind. However, dust storms are frequent on Mars so there must be mechanisms to loft dust sized particles. Greeley (2002) showed that dust can be mobilized by sand saltation on Mars. Sand-sized particles will saltate in active dunes; as sand particles impact the surface, dust may become suspended. Dust that settles on the surface of sand dunes will be removed more efficiently on dunes with higher activity. Therefore, dunes that are migrating more rapidly would have a lower albedo than dunes migrating slowly.

Alternatively, albedo and dune migration rate could be decoupled. Dust devils are another proposed mechanism to mobilize dust on Mars (Ryan and Lucich, 1983; Verba *et al.*, 2010; Reiss *et al.*, 2014). Dust devils are vortices that form when there is an unstable, near-surface layer of relatively hot air that results from surface heating (e.g., Sinclair, 1969; Rennó *et al.*, 1998). The decreased pressure at the center of dust devils enables fine-grained (dust) particles to be lifted from the surface (e.g. Greeley, 2003). It is also possible for dust devils to saltate sand which would increase the number of lofted dust particles (Kok, 2010). Even though the albedo of the dune may decrease, neither the dune nor its superposed ripples would migrate because sand saltated by a dust devil does not

move in a consistent direction. Sullivan *et al.* (2008) investigated the rippled El Dorado sand deposit within Gusev Crater using data from the Mars Exploration Rover, Spirit, in which active dust devils were observed but sand ripples only moved once. Sullivan *et al.* (2008) stated that dust devils are responsible for clearing dust off dark sandy surfaces and keeping the albedo of dunes low while strong, infrequent winds cause ripples and dune migration. The albedo of a dune field reflects the frequency of dust devils and does not yield insight into bedform migration rates.

Chojnacki *et al*. (2015) used quantitative albedo values to study dunes within Endeavour crater in Meridiani Planum. The authors observed variations in albedo with time at the dune field and attributed this to deposition and removal of dust during dust storms. Recent studies such as Bridges *et al.* (2011) have started to directly estimate migration rates by observing sand ripple movement, enabling further research into martian dune migration. In this study, I test the competing hypotheses that variations in a dune's albedo can be related to its ripple migration rate and that dust is removed from the surface of a dune by dust devils.

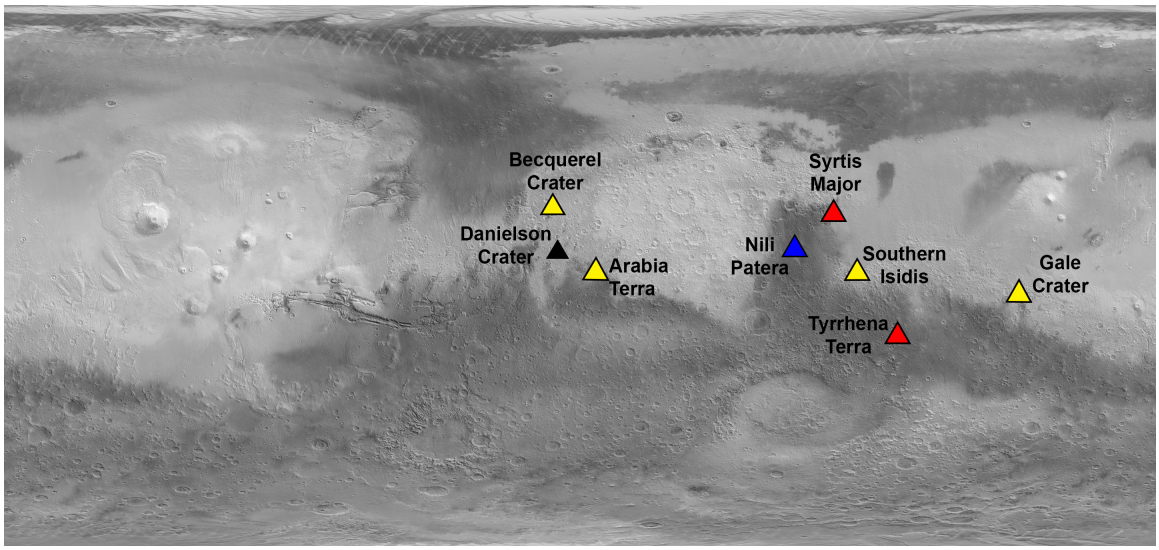

Figure 4.1 Location of each dune field used in this study. The colors correspond to the rate at which the dunes are migrating (For color interpretations, please refer to the online version of this manuscript). The blue triangle is a dune field moving faster than 1 m/ Earth year (Nili Patera). Yellow triangles are dunes moving less than 1 m/Earth year (Becquerel crater, Arabia Terra, Southern Isidis, Gale crater). Red triangles are dunes that are immobile (Syrtis Major, Tyrrhena Terra). The black triangle represents a dune field with an unknown migration rate (Danielson crater). (Background: Thermal Emission Spectrometer albedo over Mars Orbiter Laser Altimeter elevation; Christensen *et al.* 2001; Smith *et al.*, 2001)

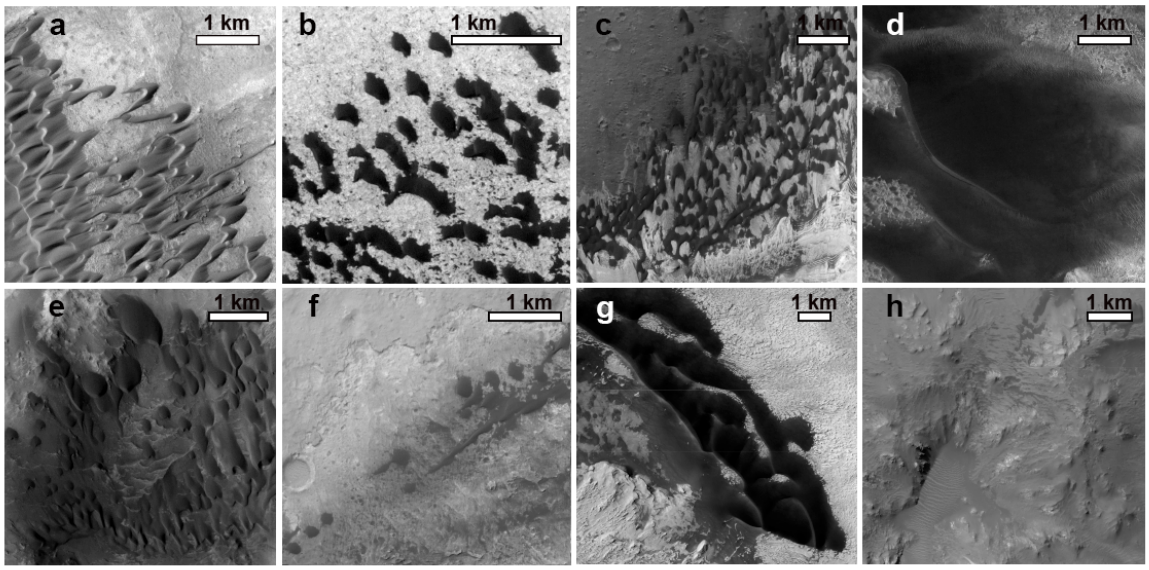

Figure 4.2 CTX images of each dune field in the study located in: a) Nili Patera, b) Arabia Terra, c) Becquerel crater, d) Syrtis Major, e) Southern Isidis, f) Gale crater, g) Danielson crater, h) Tyrrhena Terra.

4.3 Methods

We selected eight dune fields with various levels of activity that had been previously identified (located in Nili Patera, Arabia Terra, Becquerel crater, Syrtis Major, Southern Isidis, Gale crater, Danielson crater, Tyrrhena Terra; Bridges *et al*., 2011; Silvestro *et al*., 2010; 2013). Figure 4.1 shows the location of each dune field, Figure 4.2 shows a Mars Reconnaissance Orbiter Context Camera (Malin *et al.*, 2007; CTX) image of each dune field, and Table 4.1 lists the ripple migration rates of each dune field. Five of these dune fields have been shown to be active, two have not been observed to move, and one has yet to have a determined migration rate. The dunes within Nili Patera are some of the fastest-moving dunes thus far identified on Mars (Silvestro *et al*., 2010). The Bagnold dunes in Gale crater are the first active dunes on Mars to be visited by a rover (*Curiosity*). The Bagnold dunes are located at the base of a 5-km tall central mound, Mt. Sharp, which undoubtedly influences the wind dynamics affecting the dunes (e.g., Moores *et al.*, 2015). For direct comparison, dunes in Becquerel and Danielson craters, both of which also host a large stack of interior deposits, were included. The dunes in Danielson crater were the only dunes included in this study that were not analyzed by Bridges *et al.* (2011). There were no other dune fields located in mound hosting craters with known ripple migration rates. I selected this site because Danielson crater has good CTX coverage. I also included two dune fields that have not yet been observed to move (Syrtis Major and Tyrrhena Terra; Bridges *et al.*, 2011), and on which any dust entrainment from sand saltation impact has been minimal. The intracrater dunes in Syrtis Major have been consistently imaged for several years. Most other immobile dunes, including the study site in Tyrrhena Terra, do not have a wealth of data available. Dunes

that have not been observed to move are not necessarily immobile. An upper limit on their mobility can be estimated by postulating that these dunes have moved less than the spatial resolution of the camera in the amount of time between images. The images for the dunes in Syrtis Major and in Tyrrhena Terra were taken 1382 and 680 Earth days apart, respectively (Bridges *et al.*, 2011). If I assume that the High Resolution Imaging Science Experiment would be able to resolve a change ~0.5 m across (McEwen *et al.* 2010), I estimate that the ripples migrate less than ~0.13 and ~0.25 m/Earth year, respectively. These upper limit migration rates are included in Table 4.1.

We obtained CTX images taken over the eight study regions and then calculated the albedo values for each image using the calibration and projection procedures listed in Bell *et al.* (2013). Where possible, pixels were selected from the exact dunes used in earlier studies to detect their mobility (Nili Patera, Gale crater; Silvestro *et al.*, 2010; 2013). At the other sites, for each image I took an average of pixels from several dunes. I then analyzed how the albedo of each dune field varied with time (Figure 4.3).

As albedo measurements can be influenced by dust in the atmosphere, a first order atmospheric correction was performed on the data. There is always dust in the martian atmosphere (Lee & Clancy, 1990), and I did not attempt to remove all of its effects. Instead, I identified images that were taken when the atmosphere was particularly dusty. The albedo of bright terrain near each dune field was calculated. In order to determine whether an image was influenced by a dusty atmosphere, the albedo of the dunes was compared to the albedo of the nearby bright terrain, which should not brighten significantly when dust is deposited. This can be explained two ways: these bright terrains are either already covered in a thick layer of dust so that an additional layer of

dust would not affect their already-obscured albedo. Alternatively, these bright terrains are comprised of high albedo bedrock so that a layer of dust would not significantly change their albedo. Therefore, any large increase in albedo in this nearby terrain is likely due to increased dust in the atmosphere, rather than by dust deposited on the surface. I assumed that the lowest albedo value exhibited by the nearby terrain was the true albedo of the surface near the dunes. Any value that falls within a conservative estimate of the error (20%; Bell *et al.* 2013) is assumed to not be greatly affected by the atmosphere. Any points above this were likely affected by a dusty atmosphere. The points below the dashed line in Figure 4.4 represent images that did not need to be corrected. Values above the dashed line were interpreted to be images that were obtained during a dusty time and needed to be atmospherically corrected. I found the difference between each of these points and the dashed line to use in the correction. I then subtracted this value from the corresponding dune albedo to find the new "atmospherically corrected" albedo of the dune in each CTX image determined to have a particularly dusty atmosphere. This new albedo is not likely the true albedo of the dune at the time of the image, but I can place upper and lower limits on each point. The upper limit is the original albedo value and the lower limit is the albedo value of the assumed dust-free dune in each dune field.

This correction is only a first order estimate, intended to account for extremely dusty images. Identifying images that are greatly affected by the atmosphere prevents me from drawing conclusions based on incorrect data. However, since this first order correction introduces a potentially large error, I will not use any of the data points that required an atmospheric correction in any calculations. In all figures, I included error bars

on each atmospherically-corrected data point that extend from the upper and lower limits of each point.

Once I determined which images were greatly influenced by atmospheric dust, I investigated how the albedo at each site changed with time and how the albedo of fast moving dunes compared to that of slower moving dunes. I also used the albedo variations at several dunes to perform a first order estimate of how much dust is being deposited and removed. Wells (1984) estimated that a uniform coating of less than $1.5x10^{-5}$ g/cm^2 of dust raises the albedo by 0.01 if the initial albedo of the surface is between 0.1 and 0.3. This corresponds to a layer of dust ~0.15 microns thick assuming the bulk density of the dust is 1.0 g/cm^3 (Christensen, 1988).

In Syrtis Major, instead of calculating the decrease in albedo to estimate how much dust was removed I calculated the percent of a dune surface that was covered by dust devil tracks. First, I selected and counted all pixels within the region of interest (a large transverse dune) that had a low albedo. I then divided this value by the total number of pixels on that dune to find the fractional area that had been cleaned of dust. There is some uncertainty in what should be included as a dust devil track. For example, it is possible that the dust devil tracks that are moderate albedo instead of low albedo were not fully cleaned of dust, or that more dust settled on the dune after the first dust devils occurred so that perhaps the moderate albedo areas should not be included as dust-free areas. For this reason, I used two albedo estimates to cover a range of dust devil track interpretations.

Table 4.1 Information about the eight dunes in the study. Ripple migration rates are from Bridges *et al.* (2011) and Silvestro *et al.* (2013). Minimum albedo is from this study.

	Lat	Lon	Ripple Migration Rate (m/Earth year)	Minimum Albedo	CTX Images Used	Time Span (Earth Month/ Year)
Nili Patera	8.76	67.32	9.1	0.097 +/- 0.004	18	2/2007-5/2014
Crater in Southern Isidis	3.68	84.65	0.4-1.1	0.112 +/- 0.002	13	4/2010-1/2015
Crater in Arabia Terra	3.16	4.56	0.5	0.114 +/- 0.001	13	6/2007-9/2013
Bagnold Dunes, Gale crater	-4.74	137.28	0.66	0.119 +/- 0.001	16	10/2008-4/2014
Becquerel crater	21.4	351.80	0.3	0.099 +/- 0.002	10	10/2006-1/2012
Danielson crater	7.95	353.05	-	0.110 +/- 0.001	8	12/2006-4/2012
Crater in Syrtis Major	19.81	79.47	< 0.13	0.098 +/- 0.001	13	1/2007-7/2014
Crater in Tyrrhena Terra	-18.5	98.75	< 0.25	0.092 +/- 0.004	5	2/2008-5/2014

4.4 Results

Seven of the dune fields are located within craters, whereas the eighth (Nili Patera) is located in a caldera. Figure 4.3 shows the albedo measured for each dune field, uncorrected for atmospheric dust. The blue circles represent data taken during the first half of the Mars year (L_s = 0 - 180º, the aphelion season), and red squares are taken during the second half (L_s = 180 - 360º, the perihelion season). At Becquerel crater and Tyrrhena Terra, there were no observations taken during the second half of the martian year. In general, the data taken in the second half of the Mars year exhibits higher albedos, which is likely due to dust deposition, atmospheric dust, or water ice clouds. At some of the dune fields, the albedo returns to a low value during the first half of the martian year. The minimum albedo value of each site is listed in Table 4.1.

The albedos of bright terrain near each dune field (that were used to identify images taken when the atmosphere was dusty) are shown in Figure 4.4. Figure 4.5 shows the albedo of each dune field after these dusty images were identified. In Figure 4.5, several trends become apparent. In Nili Patera every high albedo observation was shown to be affected by atmospheric dust; unaffected albedos are consistently low. A similar trend occurred at the intracrater dunes in Syrtis Major. Also, the albedos of dunes in Southern Isidis and Arabia Terra varied on seasonal timescales. The albedo of the intracrater dunes in Southern Isidis increased in Mars year 30 and 32 and decreased in Mars year 31. The greatest temporal resolution in the data occurred over the intracrater dunes in Arabia Terra, which darkened at the beginning of Mars year 31. In contrast, the Bagnold dunes in Gale crater exhibited no clear increasing or decreasing trends with time.

We used the albedo variations in Figure 4.5 to estimate the amount of dust deposited and removed at several study sites, assuming the dust accumulations have the same bulk density (1.0 g/cm^3) used by Christensen (1988). At the dune field in Arabia Terra in Mars Year 31, the albedo rose from 0.114 ± 0.001 (L_s = 68°) to 0.158 ± 0.001 (L_s = 252°). This corresponds to a layer of between 0.63 and 0.69 microns of deposited dust. At the dunes in southern Isidis Planitia in Mars Year 32, the albedo increased from 0.118 ± 0.002 (120° L_s) to 0.163 ± 0.001 (248° L_s) which corresponds to a layer of dust between 0.63 and 0.72 microns thick. The typical diameter of martian airborne dust is thought to be 1-2 microns (e.g. Wolff *et al.*, 2003), so a layer of dust less than 1 micron thick implies that the layer does not completely cover the dune surfaces. This is consistent with the dust-covered dunes in these locations being darker than their surrounding terrain.

The albedo of the dunes in Arabia Terra decreased consistently from MY 30, L_s = 351° to MY 31, L_s = 68° after the dusty perihelion season. It is unclear what the initial post-dust storm albedo of the dune was, but the albedo decreased from 0.133 ± 0.001 to 0.114 ± 0.001 over a period of 165 Earth days, or 77° L_s. I calculate that a layer of dust between 0.26 and 0.32 microns was removed. This corresponds to a dust removal rate of a 0.0016-0.0019 micron layer per Earth day or a 0.0034-0.0042 micron layer per degree of Ls. Previously I found that there was a 0.63-0.69 micron layer of dust deposited on the dunes in a crater in Arabia Terra. At my estimated removal rate, and assuming this dust was deposited on a dust-free dune, I can calculate that it would take between 363 and 394 Earth days or roughly half a Mars year (a period of L_s between 164° and 185°) to remove this dust. However, this layer of dust was almost entirely removed over a period of 103°

L_s, from $L_s = 252°$ in MY 31 to $L_s = 355°$ in MY 31, indicating that dust removal rates, and thus the processes that drive them, are variable in time. This is consistent with previous work indicating that dust removal can occur episodically (e.g. Geissler *et al.*, 2010; 2016).

The dunes in southern Isidis are cleared of dust slightly slower than those in Arabia Terra. The albedo decreased from 0.135 ± 0.001 (MY 31, $L_s = 276°$) to 0.118 ± 0.001 (MY 32, $L_s = 19°$) over a period of 188 Earth days, or 103° L_s. This corresponds to a 0.23-0.029 micron layer of dust being removed at a rate of 0.0012-0.0015 microns per earth day or 0.002-0.003 microns per L_s.

The correlation of the albedo of each dune field and its ripple migration rate is shown in Figure 4.6 using the minimum albedo of each dune field. As several of the dune fields do not have sufficient data taken during the martian dusty season, using the range of data values or the highest albedo for each dune would not be an accurate comparison. Danielson crater is not included in this plot because the migration rate for this dune field has not yet been measured. Based on these results, there is no simple correlation between a dune field's minimum albedo and ripple migration rate. The linear regression line is a poor fit with a low R^2 value of 0.07. Both the fastest and slowest ripples in this study exhibit low albedo values (less than 0.1), whereas the rest of the migrating ripples exhibit higher albedo values (between 0.11 and 0.12).

All albedo values from each dune field are plotted against the solar longitude at the time each image was taken in Figure 4.7 a and 4.7b. Figure 4.7a shows that the albedos of dune surfaces were generally higher during the second half of the Mars year, which is consistent with the martian dusty season. Specifically, there were typically no

low albedos (<0.12) between roughly L_s = 180° and L_s = 320°. Figure 4.7b, the atmospherically corrected version, shows that in some cases the higher albedos could be result of atmospheric dust rather than deposited dust. When using all uncorrected values, the average albedo of observations taken before L_s = 180° is 0.118 ± 0.02 and after L_s = 180° is 0.140 ± 0.02. When the data points that were greatly affected by dust are removed the average albedo does not change much: the average albedo before L_s = 180° is 0.117 ± 0.01 and after L_s = 180° is 0.140 ± 0.02.

Lastly, I identified dust devil tracks in Syrtis Major, where faint dust devil tracks were visible over some portion of the dunes in almost every image. Figure 4.8 shows the appearance and disappearance of dust devil tracks over sand dunes in Syrtis Major. Figure 4.9 shows a single CTX image taken after the global dust storm in 2007, or Mars Year 28, in which dusty dunes are crossed with dust devil tracks. Using the methods described in section 3, I find that between roughly 25% (Figure 4.9c) and 50% (Figure 4.9d) of the dune was cleared of dust, assuming that dust was initially deposited evenly across the dune. I can use this to estimate how quickly dust devils can remove dust from the surface of a dune. The CTX image used was taken in MY 28, L_s = 325°. Wang *et al.* (2015) noted that the global dust storm in MY 28 started around L_s = 260° and the initial decay phases began around L_s = 310°. The authors also noted that the dust haze continued to dissipate after L_s = 310°, so dust likely would have continued settling after this time. For my purposes, I will use this date as an estimate of the end of the dust storm, so that between L_s = 310° and L_s = 325°, 25-50% of the dune was cleared. If I use 25% (which may account for additional dust fallout) and if the rate of dust clearance is constant, the entire dune would be dust-free by MY 29, L_s =10°. If I use 50%, the dune would be dust-

free by MY 28, L_s =340°. The next image taken, which exhibits a low albedo value, was taken at MY 29, L_s = 57° (Figure 4.8c). Therefore, the majority of the dust was cleared before L_s = 57°, which is consistent with my calculations. In reality, the rate of dust clearance is not likely constant, but rather an exponential decay. While this would cause the dune to be cleared more slowly, this could still be consistent with a nearly dust-free dune by L_s = 57°. Indeed, Figure 4.8c shows that some faint dust devil tracks were still visible on the surface of the dune, as well as at the edge of the dune and on the adjacent sandy surfaces.

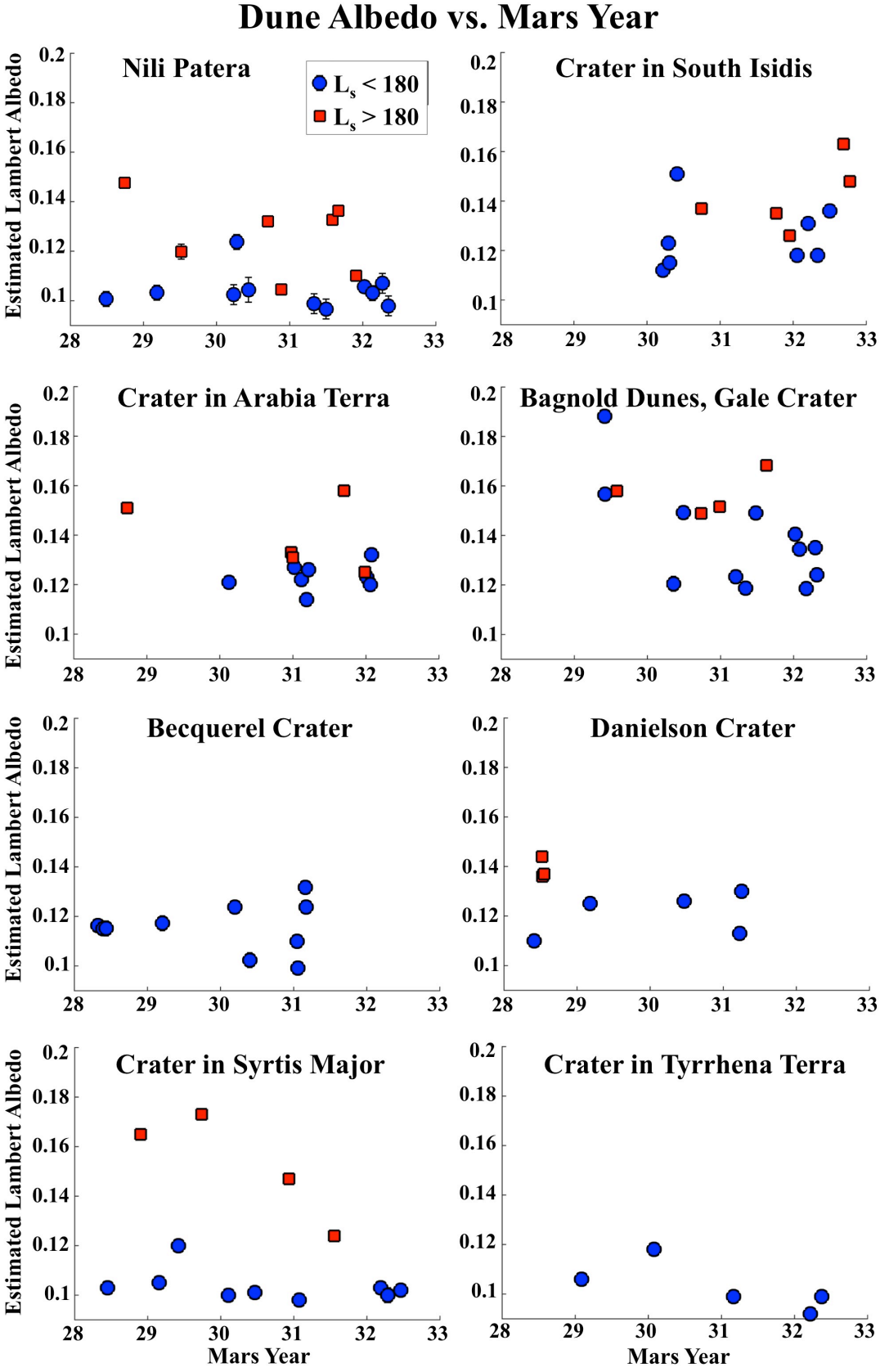
Dune Albedo vs. Mars Year
Nili Patera
Crater in South Isidis
Crater in Arabia Terra
Bagnold Dunes, Gale Crater
Becquerel Crater
Danielson Crater
Crater in Syrtis Major
Crater in Tyrrhena Terra
L_s < 180
L_s > 180
Estimated Lambert Albedo
Mars Year
0.2
0.18
0.16
0.14
0.12
0.1
28
29
30
31
32
33

Figure 4.3 CTX albedo (not atmospherically corrected) of dunes plotted against the time when the image was taken. The x- and y-axes are the same in every plot. Blue circles represent images taken during the first half of the martian year, when the atmosphere is generally less dusty (L_s = 0 - 180º). Red squares represent images taken during the second half of the martian year, when dust storms are more common (L_s = 180 - 360º).

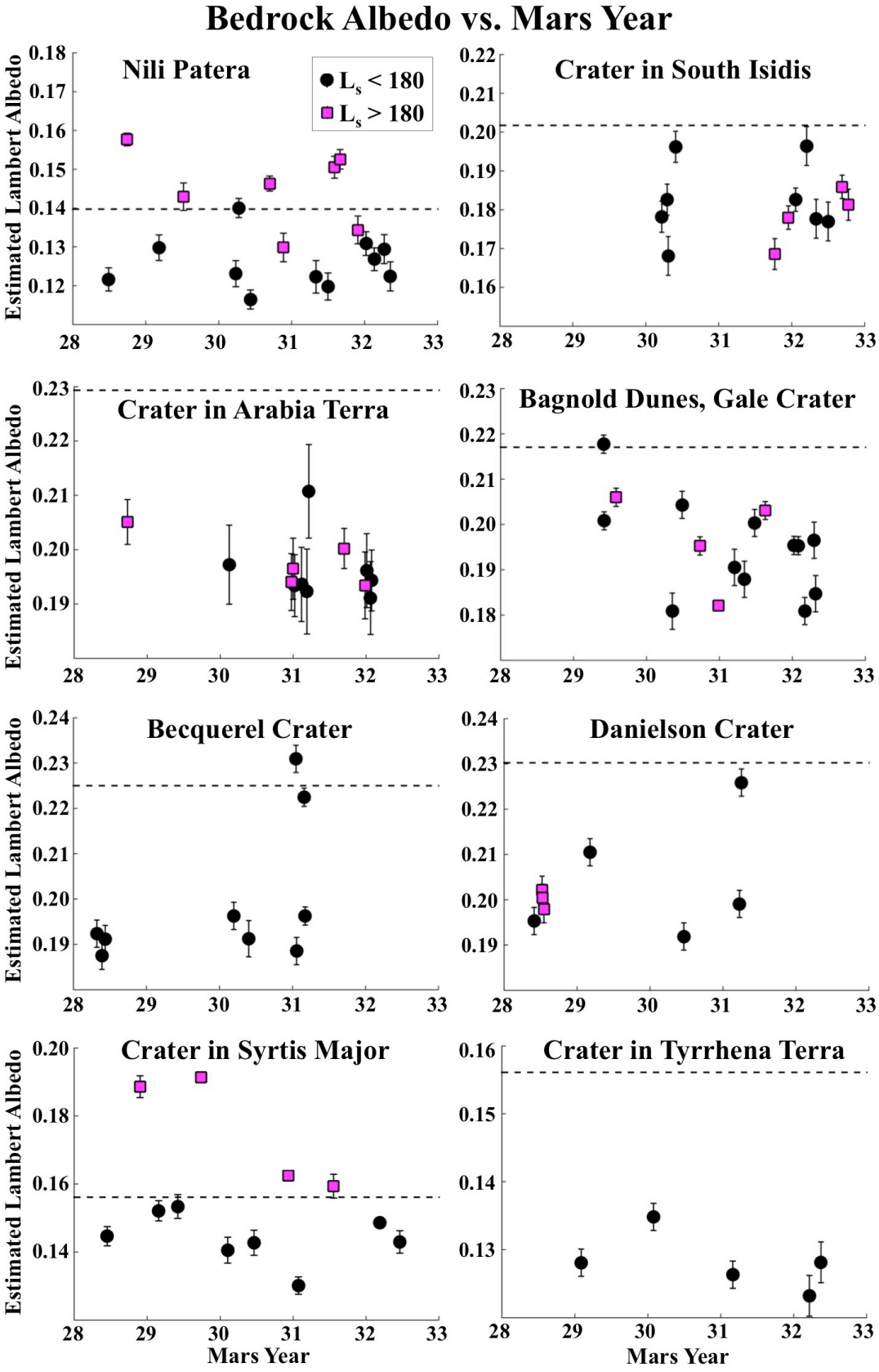
Bedrock Albedo vs. Mars Year
Nili Patera
$L_s < 180$
$L_s > 180$
Crater in South Isidis
Crater in Arabia Terra
Bagnold Dunes, Gale Crater
Becquerel Crater
Danielson Crater
Crater in Syrtis Major
Crater in Tyrrhena Terra
Estimated Lambert Albedo
Mars Year

Figure 4.4 The albedo from CTX images of bright terrain near each dune field. The x-axis is the same in each plot, but due to the variety of terrain used, the y-axis is different in each plot. The black circles are images taken in the first half of the Mars year, whereas the pink squares are images taken in the second half. Points below the dashed line are likely not greatly effected by atmospheric dust.

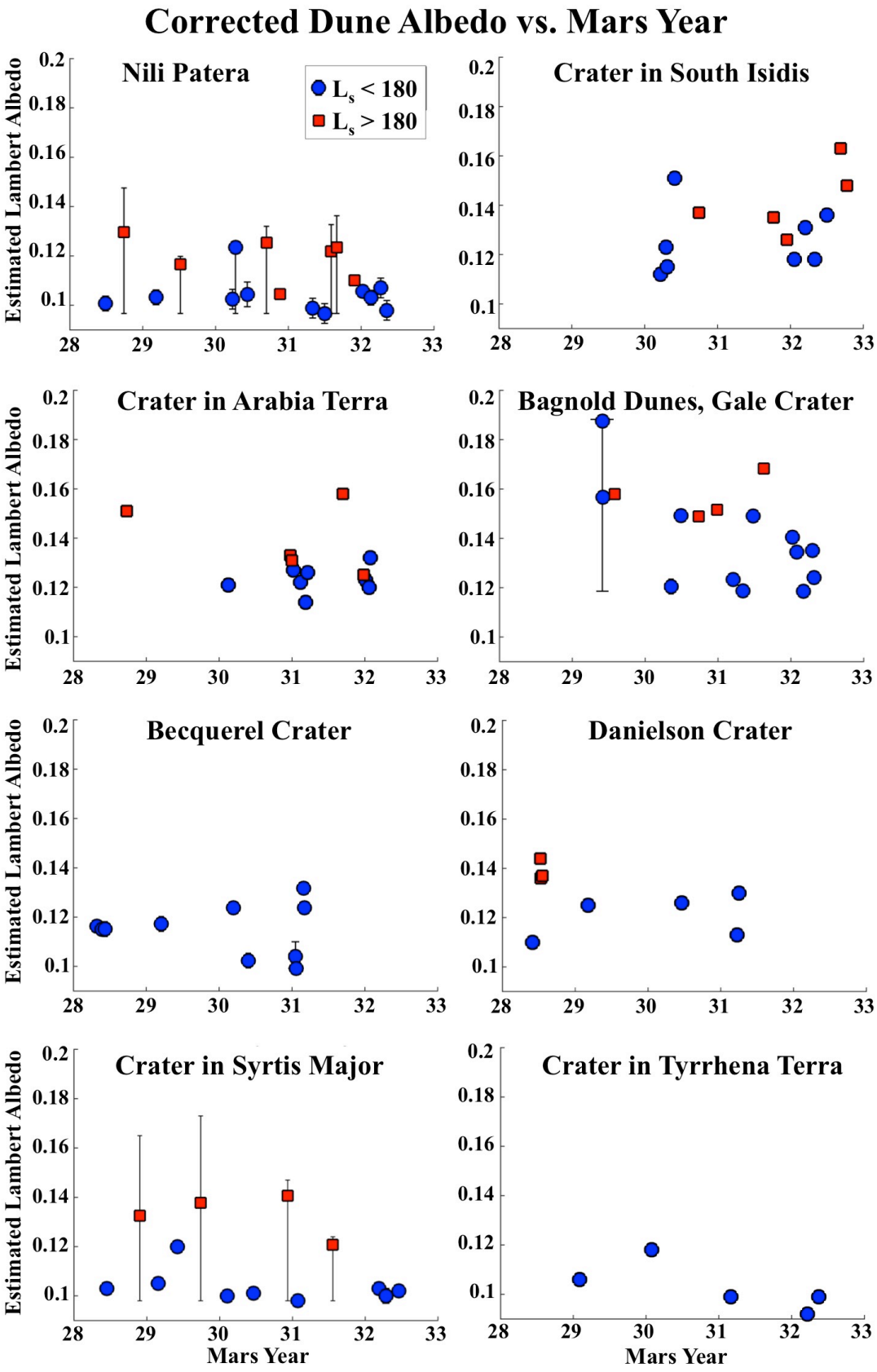
Corrected Dune Albedo vs. Mars Year
Nili Patera
$L_s < 180$
$L_s > 180$
Crater in South Isidis
Crater in Arabia Terra
Bagnold Dunes, Gale Crater
Becquerel Crater
Danielson Crater
Crater in Syrtis Major
Crater in Tyrrhena Terra
Estimated Lambert Albedo
Mars Year
0.1
0.12
0.14
0.16
0.18
0.2
28
29
30
31
32
33

Figure 4.5 Atmospherically corrected version of Figure 4.3. Points with large error bars were observations taken when there was a lot of atmospheric dust. Observations taken during dusty times are regarded as the maximum possible value. I use arrows for the bottom error bars because the minimum possible value is not known. See Methods section for a complete description of the correction.

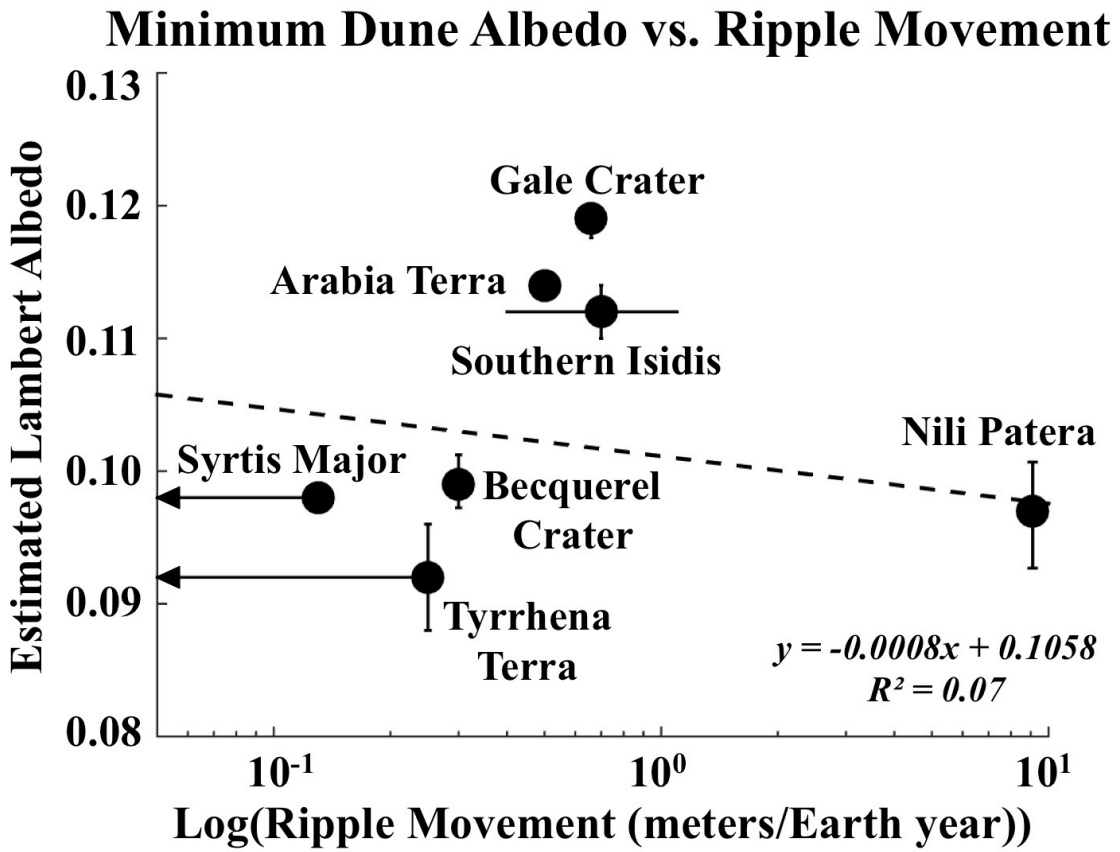

Figure 4.6 The minimum albedo of each dune field plotted against the rate of movement of the ripples at each dune field. The horizontal axis is logarithmic because most ripples moved less than 1 m/Earth year. The two points with horizontal arrows represent the dunes that have not been observed to move. These ripples must be moving slower than 0.13 and 0.25 m/Earth year, respectively. The points are at these maximum values. The arrows are included to show that the exact rate of movement is unknown.

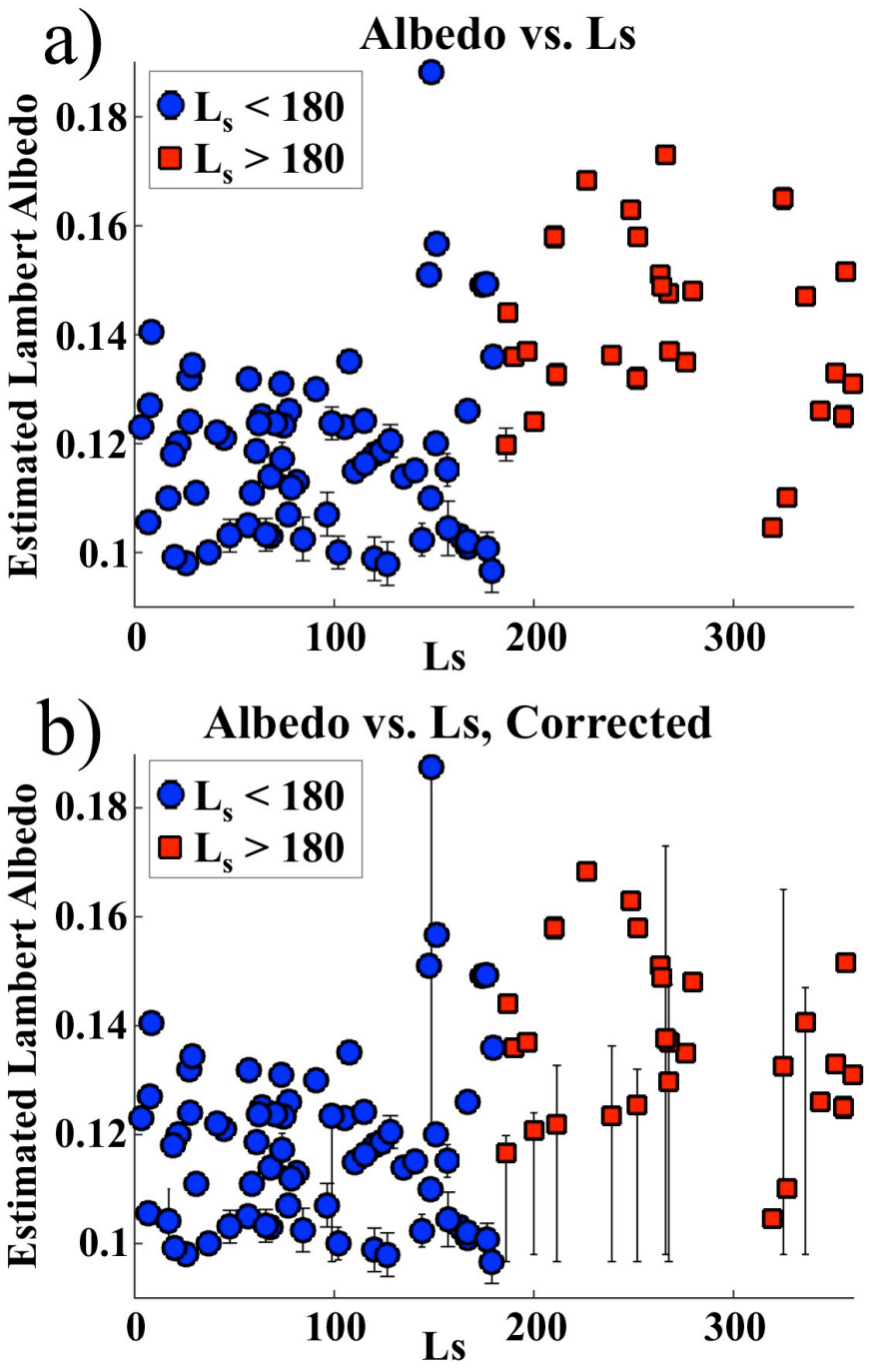

Figure 4.7 a) The albedo (not atmospherically-corrected) of each dune field (all CTX observations) plotted against the L_s value at the time of the image. Generally, the albedo of dunes is greater during higher $L_s > 180^o$. b) The atmospherically corrected albedo of each dune field against L_s.

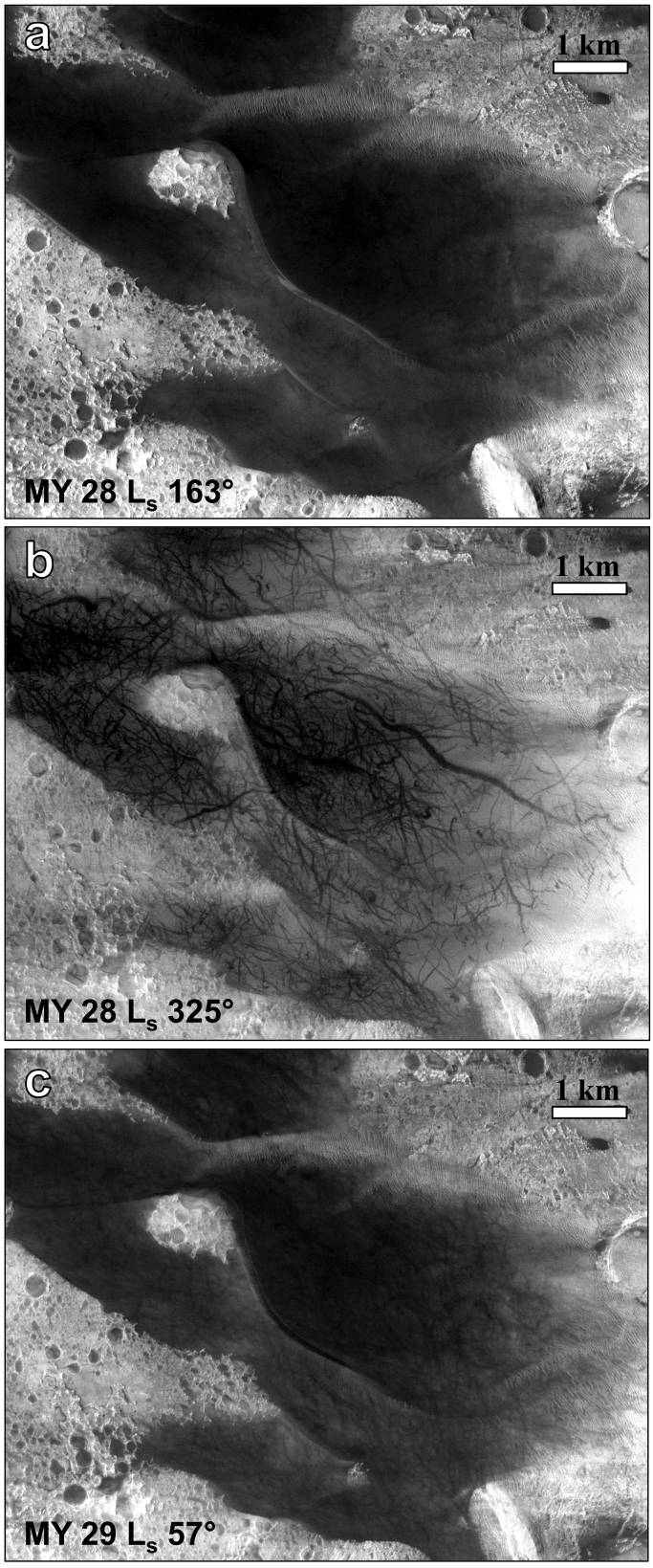
a
1 km
MY 28 L$_s$ 163°
b
1 km
MY 28 L$_s$ 325°
c
1 km
MY 29 L$_s$ 57°

Figure 4.8 Progression of CTX images before and after a global dust storm in Syrtis Major. a) CTX image P03_002110_2000_XI_20N280W. Before the MY 28 global dust storm. The dune has a low albedo and only faint traces of dust devil tracks. b) CTX image P12_005578_2002_XN_20N280W. After the global dust storm. The dune has a higher albedo and obvious dust devil tracks. c) CTX image P18_008004_1992_XI_19N280W. After the global dust storm. The dune has a low albedo again and the dust devil tracks have mostly disappeared.

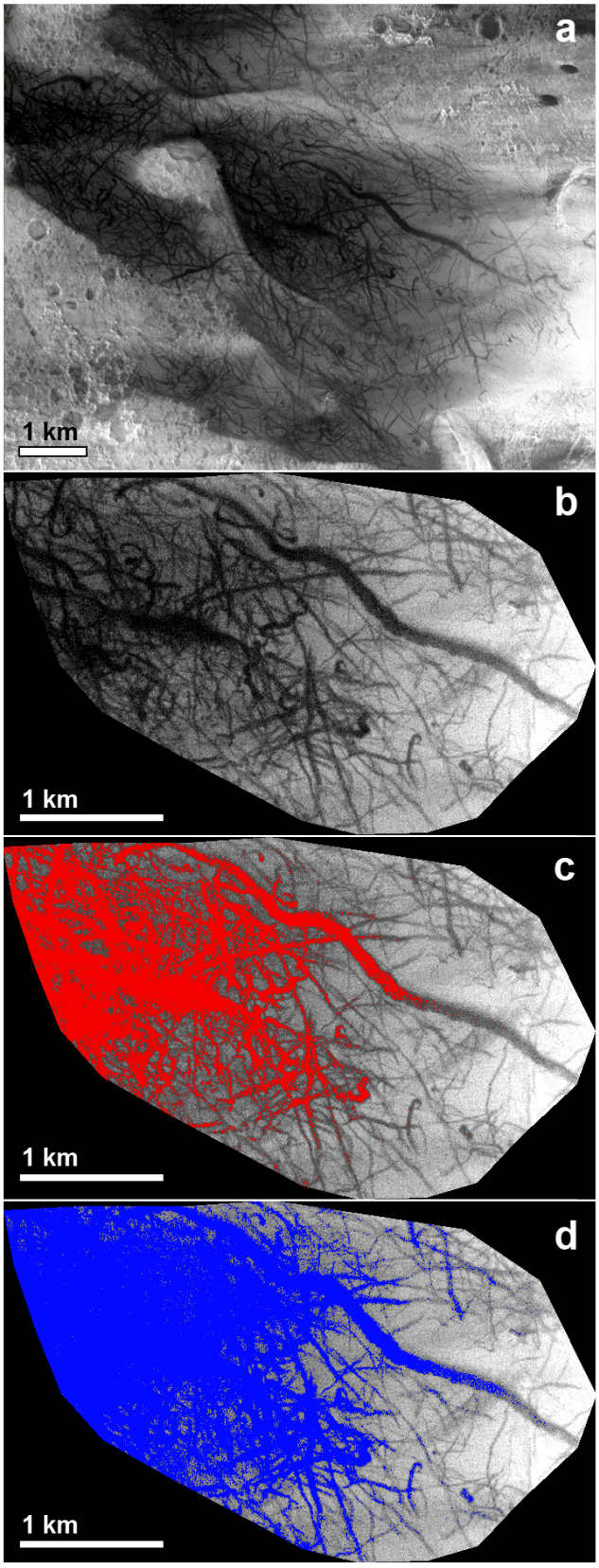

Figure 4.9 a) Dust devil tracks over the dunes in a crater in Syrtis Major (CTX image P12_005578_2002_XN_20N28 0W; My 28 L_s = 325º). b) The region of interest. c) and d) The red and blue areas represent two interpretations of the area on the dune that has been cleared of dust. c) A conservative estimate of dust removal in which only the blackest, lowest albedo dust devil tracks are considered to be cleared of dust. d) A less conservative estimate of dust removal in which all dust devil tracks (even grey, moderate albedo tracks) are considered to be cleared of dust.

4.5 Discussion

4.5.1 Dune albedos

The albedos of dunes increase after L_s = 180° (Figure 4.7) which can be explained by large-scale martian dust storms, which tend to occur after Ls 180° (e.g., Wang *et al.*, 2013) and lead to elevated optical thickness (e.g., Clancy *et al.*, 2000). During dust storms, and in their wake, relatively bright dust is deposited on top of relatively dark dunes.

The dunes in Nili Patera are some of the fastest moving dunes thus far identified on Mars (Bridges *et al.*, 2011). My results suggest that this dune field exhibits a consistently low albedo throughout the year. This implies that any dust deposited during the dusty season is almost immediately removed and that these dunes are consistently active throughout the dusty season. These dunes could remain active throughout the year, but it is also possible that winds strong enough to saltate sand occur only during the dusty season and leave the dunes clear of dust but also immobile until the next dusty season. At the Nili Patera dune field, the former is more feasible. Ayoub *et al.* (2014) showed that these dunes are likely active year-round, with a peak in activity from L_s = 207-355º, in the midst of the dusty season.

The intracrater dunes in southern Isidis Planitia and Arabia Terra had temporary trends of increasing albedo which I propose correspond to deposition of dust layers 0.63-0.72 and 0.63-0.69 microns thick, respectively. This suggests that winds over those periods are too weak to prevent dust from accumulating on the dunes. In Arabia Terra the albedo gradually decreased from the end of MY 30 through the beginning of MY 31. There are six CTX images that were taken every few weeks during this time. In the first

image taken in MY 30 at L_s = 351º the dunes have a high albedo, which is expected at the end of the dusty perihelion season. In the next four observations (from MY 30 L_s = 359º to MY 31 L_s = 41º) the dune albedos decreased, consistent with dust removal from their surfaces. In the sixth observation (MY 31 L_s = 68º) the dunes exhibit a slightly higher albedo. One explanation for the decrease in albedo at the Arabia Terra dune field is that dust is still settling out of the atmosphere after the dusty season. In this scenario the observed decrease in albedo would have been caused by a steadily diminishing dust load in the atmosphere, which would gradually clear to fully reveal the dark dunes. If this were the case, the albedo of the bright terrain near the dunes should also have decreased over this time period, but Figure 4.4 shows this did not happen. In the first five observations (from My 30 L_s = 351º to MY 31 L_s = 41º) the bright terrain had extremely similar albedo values (within ~.05), but in the sixth observation (MY 31 L_s = 68º) the albedo of the bright terrain increased. Therefore, the only data point that could have been influenced by dust in the atmosphere is the sixth observation, which could explain the increased albedo noted for the dune field. Instead, the decreasing albedo trend in Arabia Terra likely implies that the dunes are getting consistently cleared of surface dust after the perihelion season. The wind was active enough in this region to saltate sand and loft dust into the air, but it was not so strong and/or frequent that all the dust was cleared from the dune immediately following the dusty season.

The intracrater dunes in Syrtis Major exhibited a trend similar to those in Nili Patera, with a low albedo throughout the year and high albedo observations taking place during very dusty periods and requiring an atmospheric correction. However, the ripples on these dunes have not been observed to move (see Methods section), which means that

the ripples must be moving less than ~0.13 m/Earth year (Bridges *et al.*, 2011). There are two possible explanations for the low albedo of a very slow moving dune. Wind strong enough to saltate sand could occur every year at the end of the dusty season and clear dust off the surface of the dune but not move enough sand to cause significant ripple migration. The other possibility is that dust devils clear the surface of the dunes without causing migration. The latter hypothesis is supported by the presence of many dust devil tracks in a CTX image over the dunes in Syrtis Major acquired at L_s = 325º after the end of the 2007 (MY 28) global-scale dust storm (Figure 4.8). The presence of tracks implies that dust devils were the only significant mechanism of particle entrainment after dust accumulated on the dune surfaces, as the saltation induced by strong winds would have erased the tracks. It is possible that strong winds occur at some season in this location, but these winds did not occur at the end of the dusty season or immediately after it in Mars Year 28. The presence of dust devil tracks also suggests that the albedo variations observed are real surface albedo changes. The presence of both dark and light areas on the dune rules out the possibility that the albedo variations are entirely due to atmospheric effects.

It is difficult to draw conclusions from the results at Becquerel crater and at the crater in Tyrrhena Terra, as there have not yet been observations taken in these locations after L_s = 180°. These dune fields have a low albedo during the aphelion (nondusty) season, but I cannot tell how much dust was deposited or how quickly it may have been removed. I selected the crater in Tyrrhena Terra in order to include a second dune field with no observed movement, in addition to the stationary dune field in Syrtis Major. I attempted to find a site with no movement recorded and that had CTX images taken

throughout the Mars year, but no immobile dune fields have adequate temporal coverage. This is understandable, as it is not as beneficial to spend resources monitoring a dune field that is immobile when those resources could be spent monitoring mobile dune fields. These sites are still useful to this study because I can compare the minimum albedo at these dunes to other sites.

Although there are observable trends in the data for most of the study sites, some exhibit more scatter. The dunes in Gale crater and in Danielson crater generally have higher albedos during $L_s < 180°$, but beyond that it is difficult to identify trends at these sites. Possible explanations for the scattered albedo of the dunes in Gale crater could be that winds strong enough to saltate sand are very sporadic, or that dust fallout might not be as seasonally recurrent relative to the more regularly-varying sites, such as the crater in Syrtis Major.

4.5.2 Minimum albedo and migration rate

The minimum albedo of each dune field is listed in Table 4.1: for each dune field studied, there is a minimum value to which the albedo roughly returns each year which may represent the true, dust-free, albedo of each dune field. Several of the study sites (including the fast-moving Nili Patera dune field) reach albedo values below 0.1. If I assume that ~0.1 is the dust-free albedo of all martian dunes, this implies that a dune that does not reach this low albedo is never entirely cleared of dust. From this I would predict that the dune fields in this study that have minimum albedos higher than 0.1 (between 0.11 and 0.12) are removing dust less efficiently, and therefore are moving more slowly than dunes that have minimum albedos below 0.1 (Figure 4.6). The fastest moving dunes

in this study (Nili Patera; 9.1 m/Earth year) have a very low minimum albedo of 0.097, whereas dunes moving slower (0.5-1.0 m/Earth year) have the highest minimum albedos. Immobile or very slow moving dunes (<0.5 m/Earth year) also exhibit low albedos. It is possible that albedo correlates to ripple migration rate above a certain threshold (~0.5 m/Earth year) where saltation is the primary dust removal process. Below this threshold the albedo of a dune is decoupled from its migration rate and dust devils primarily remove dust.

The question remains as to why dust devils wouldn't also clear dust off of the slow-moving dunes in Gale crater, Arabia Terra, and Southern Isidis. It is possible that these particular dune fields are located in areas where the circulations that produce strong and frequent dust devils are suppressed. Data from the *Curiosity* rover in Gale crater support this idea, as very few dust devils have been observed by the rover over the past two martian years.

One additional potential issue with drawing conclusions based on multiple dune fields is the assumption that the dust-free albedo of all dunes is the same. Martian sand dunes have similar compositions of primarily pyroxene, which suggests that their albedos are also similar (Tirsch *et al.*, 2011). One specific example is provided by the Mars Science Laboratory investigations at the Rocknest aeolian bedform in Gale crater. This bedform contained amorphous material, plagioclase, olivine, and pyroxene (Bish *et al.*, 2013). However, it is possible that some dunes contain additional minerals from local sources that could cause the albedo of the dunes to increase. For example, Danielson crater and Gale crater have high minimum albedos and are located within craters that contain large interior deposits. Light-toned sediment eroded from those layered deposits

could be included in the dunes. The Rocknest aeolian bedform did not contain any phyllosilicates (which have been observed in this area by orbiters; Bish *et al.*, 2013), but investigations at dunes closer to the mound could reveal different minerals. The Curiosity rover will obtain data that can address this idea during its investigation of the Bagnold dunes in Gale crater. If the albedo of a dune is shown to change with the local mineralogy, then albedo might not be able to be used as a proxy for migration rate, as albedo differences due to either dust or composition could be indistinguishable. One could potentially work around this challenge by constraining and accounting for the composition of each dune.

These results show that the albedo of dunes does not have a simple correlation with the migration rate of dunes or their superposed ripples. There is no way to distinguish between fast moving dunes with a low albedo and slow or immobile dunes with a low albedo. Variations in albedo may be due to compositional differences rather than dust cover. Therefore, I conclude that albedo should not be used as a proxy to determine how quickly a dune is moving.

4.5.3 Dust devils

In this study, I found that albedo variations can be influenced by the occurrence of dust devils. The only site in this study that definitively experiences dust removal by dust devils is in Syrtis Major. These dunes have not been observed to move and almost every image reveals traces of dust devil tracks across the dunes. I estimated how quickly dust devils can remove dust from the surface of a dune, but I do not have an estimate of how much dust was deposited on the dunes in Syrtis Major. All observations at Syrtis Major

taken in the second half of the martian year were affected by a dusty atmosphere. This makes it difficult to compare how quickly dust devils and saltation removed dust from the surface of these dunes.

We can compare these results on saltation and dust devils at dunes to the results from Sullivan *et al.* (2008) for the El Dorado ripple field at Gusev crater. Ripples near El Dorado were observed to move during the 2007, MY 28, dust storm. If the only time that winds are strong enough to initiate saltation at this site occurs during dust storms, then saltation should not be the primary mechanism for removing dust and keeping the albedo of sand dunes low (Sullivan *et al.,* 2008). Even if there is a gust of wind strong enough to saltate particles during a dust storm, dust can continue to be deposited on the dune's surface after the strong wind ceases. I hypothesize that the El Dorado ripple-like bedforms and the ripples superimposed on dunes in Syrtis Major are similar and represent a class of very slow-moving bedforms. At these sites, there are not many occurrences of strong winds. Strong winds occur during the dusty season when the albedo will not decrease because freshly deposited dust quickly replaces that removed by saltation.

Dust-covered dune fields could be a good site for observing dust devil tracks. By removing high albedo dust from low albedo dunes, dust devils create albedo patterns with high contrast. Also, dust devils tend to occur in the local summer and at specific locations (*e.g.* Fisher *et al*., 2005; Cantor *et al.*, 2006). While it is possible that the dunes in Syrtis Major happen to be in a location that is ideal for dust devils, it is also possible that many dune fields are an ideal terrain for dust devils. Sinclair (1966) proposed that the ideal conditions for dust devils include a large supply of loose surface material, areas with anomalously high surface temperatures, local impediments to wind flow that can create

vortices, and terrain boundaries where horizontal thermal gradients can occur. Dune fields match this description very well. After dust storms, a large amount of dust is available at the surface, accumulations of dark, moderately low thermal inertia sand can have the highest daytime surface temperature in an area, and the boundary between the hot sand dunes and the relatively cool adjacent surfaces would create horizontal thermal gradients.

It is possible that dust devils preferentially form on all dune fields because their surface properties present an ideal setting for vortex generation. Their tracks would be most easily observed on slow-moving or immobile dunes, because the strong winds required to saltate sand and raise dust occur infrequently there. On mobile dune fields, dust devil tracks are likely quickly erased by saltation. The dune fields in Gale crater could represent an exception to this rule. Despite being an ideal setting for vortex generation, these dune fields could be located in an area in which the circulations that produce devils are suppressed.

4.6 Conclusions

Our analysis of dune albedo variations has led to several conclusions:

1. Based on my assumptions and corrections, the albedo of dunes should not be used as a proxy for migration rate. The minimum albedo of the studied dune fields does not correlate well with ripple migration rate. Both fast- (Nili Patera dunes; 9 m/Earth year) and slow- (Syrtis Major dunes, etc.; < 0.5 m/Earth year) moving dunes exhibit low albedos. Dunes with

intermediate migration rates exhibit high albedos. Additional data and future studies will be required to confirm the robustness of this trend.

2. Temporal albedo variation trends may reveal information about the local wind regime. The albedo of the Nili Patera dunes was consistently low, which implies that strong winds occur frequently during the dusty season to prevent much dust from settling on dunes. The albedo gradually decreased on the dunes in craters in Arabia Terra and southern Isidis, which implies that strong winds occur consistently after the dusty season to slowly remove the deposited dust. In southern Isidis, the albedo gradually increased from L_s = ~90º to ~345º, suggesting that winds over that period were too weak to prevent dust from accumulating on the dunes. The change in albedo was more random on the dunes in Gale crater, which implies that either strong winds occur sporadically or that dust fallout might not be as seasonally constrained here.
3. The dust on most of the dune fields that I studied was removed by strong winds that saltated sand, but on some slow or immobile dunes the dust was primarily removed by dust devils. Dust devil tracks were not observed on any mobile dunes in this study, whereas they were observed in almost every observation taken at the stationary dune field in a crater in Syrtis Major. Indeed, dune fields may be an ideal location for dust devil formation on Mars.

CHAPTER 5

COMPLEX EXPLOSIVE VOLCANIC ACTIVITY ON THE MOON WITHIN OPPENHEIMER CRATER

Kristen A. Bennett, Briony H. N. Horgan, Lisa R. Gaddis, Benjamin T. Greenhagen, Carlton C. Allen, Paul O. Hayne, James F. Bell III, David A. Paige (2016) Complex explosive volcanic activity on the Moon within Oppenheimer crater. Icarus, 273, 296-314, http://dx.doi.org/10.1016/j.icarus.2016.02.007.

Oppenheimer Crater is a floor-fractured crater located within the South Pole-Aitken basin on the Moon, and exhibits more than a dozen localized pyroclastic deposits associated with the fractures. Localized pyroclastic volcanism on the Moon is thought to form as a result of intermittently explosive Vulcanian eruptions under low effusion rates, in contrast to the higher-effusion rate, Hawaiian-style fire fountaining inferred to form larger regional deposits. I use Lunar Reconnaissance Orbiter Camera images and Diviner Radiometer mid-infrared data, Chandrayaan-1 orbiter Moon Mineralogy Mapper near-infrared spectra, and Clementine orbiter Ultraviolet/Visible camera images to test the hypothesis that the pyroclastic deposits in Oppenheimer crater were emplaced via Vulcanian activity by constraining their composition and mineralogy. Mineralogically, I find that the deposits are variable mixtures of orthopyroxene and minor clinopyroxene sourced from the crater floor, juvenile clinopyroxene, and juvenile iron-rich glass, and that the mineralogy of the pyroclastics varies both across the Oppenheimer deposits as a whole and within individual deposits. I observe similar variability in the inferred iron

content of pyroclastic glasses, and note in particular that the northwest deposit, associated with Oppenheimer U crater, contains the most iron-rich volcanic glass thus far identified on the Moon, which could be a useful future resource. I propose that this variability in mineralogy indicates variability in eruption style, and that it cannot be explained by a simple Vulcanian eruption. A Vulcanian eruption should cause significant country rock to be incorporated into the pyroclastic deposit; however, large areas within many of the deposits exhibit spectra consistent with high abundances of juvenile phases and very little floor material. Thus, I propose that at least the most recent portion of these deposits must have erupted via a Strombolian or more continuous fire fountaining eruption, and in some cases may have included an effusive component. These results suggest that localized lunar pyroclastic deposits may have a more complex origin and mode of emplacement than previously thought.

5.1 Introduction

Over 100 pyroclastic or "dark mantling" deposits have thus far been identified on the Moon (Gaddis *et al.*, 1985, Gaddis *et al.*, 2003, Hawke *et al.*, 1989, Carter *et al.*, 2009,Gustafson *et al.*, 2012 and Campbell *et al.*, 2014). These deposits are characterized by their low albedo and are believed to be products of explosive volcanic eruptions. Pyroclastic deposits are high priority targets for future exploration because of both their scientific value and their potential as a resource. Lunar pyroclastic materials are thought to originate from deep within the Moon. Therefore their primitive composition may help to constrain the composition and geophysical evolution of the lunar magma ocean and the lunar mantle (Delano, 1986 and Shearer and Papike, 1993). Pyroclastic glass beads

returned as Apollo samples have surface coatings that indicate that they formed in volatile-rich eruptions, and recent reanalysis of the Apollo 17 glass beads revealed melt inclusions with water content as high as the Earth's mantle (Hauri *et al.*, 2011). The abundance and source of these volatiles may have major implications for the interior structure, composition, and origin of the Moon (Hauri *et al.*, 2015). Pyroclastic deposits are also likely targets for future *in situ* resource extraction, due to both their high abundances of metal oxides that could be processed to yield oxygen in higher abundances than any other known lunar material (Allen *et al.*, 1996), and their thickness and uniform grain size, which could facilitate rapid extraction of ^{3}He (Hawke *et al.*, 1990). Indeed, Burns *et al.* (2013) proposed a landing site near the Schrodinger pyroclastic deposit as a potential location for a future lunar mission.

Lunar pyroclastic deposits are generally divided into localized (<1000 km^2 in area) and regional (>1000 km^2 in area) deposits (*e.g.,* Gaddis *et al.*, 2003). The localized deposits that have been investigated previously using Earth-based telescopic spectra appear to contain minerals likely to originate from different sources, including juvenile magmatic minerals (typically clinopyroxenes, olivine and/or quenched glass) and local country-rock (orthopyroxenes from lunar highlands or clinopyroxenes from mare; Hawke *et al.*, 1989) or mixtures of these. However, the juvenile component of localized deposits is poorly constrained, as both olivine and glass could account for the spectral shapes observed (Gaddis *et al.*, 2000). Strombolian activity is not energetic enough to strip country rock from the vent walls to produce deposits with non-juvenile components. Fire fountaining could erode the vent wall enough to incorporate non-juvenile material, but this implies such high eruption rates that the ejected pyroclasts would be hot enough that

they would coalesce to form lava flows instead of forming pyroclastic deposits (Head and Wilson, 1979). Therefore, localized deposits are primarily thought to result from Vulcanian-style periodic eruptions. Vulcanian eruptions occur when intruding magma near the surface solidifies and creates a plug. The magma in the conduit is trapped below this plug; as gas exsolves from the magma, pressure builds up under the plug. Once the pressure overcomes the strength of the plug the magma explodes violently, ejecting juvenile magmatic material and up to 50% country rock (*e.g.,* Head and Wilson, 1979). Vulcanian-style eruptions imply a relatively low mass eruption rate (*e.g.,* Head and Wilson, 1979 and Gaddis *et al.*, 2000), as would be the case for extrusion through crustal weak points from sills and dikes (Head and Wilson, 1979 and Head *et al.*, 2000). This scenario is supported by the association of small deposits with floor-fractured craters (*e.g.*,Schultz, 1976). Floor-fractured craters are thought to occur when a sill intrudes beneath a crater and the increased pressure causes the crater floor to uplift and fracture. The magma in the sill can then slowly travel through these fractures and reach the surface with a low mass eruption rate (Head and Wilson, 1979 and Jozwiak *et al.*, 2015). Dozens of previously unrecognized localized pyroclastic deposits have been identified in the past decade using Clementine data (Gaddis *et al.*, 2003), LROC visible images (Gustafson *et al.*, 2012), and radar signatures (Carter *et al.*, 2009 and Campbell *et al.*, 2014), resulting in what is now a global population of more than 100 hypothesized local and regional pyroclastic deposits.

Regional pyroclastic deposits are thought to result from either low mass eruption rate Strombolian eruptions (coalesced bubble explosions) or high mass eruption rate fire fountains (Heiken *et al.*, 1974 and Wilson and Head, 1981). The regional deposits may be

related to mare volcanism, as they are often associated with rilles and vent-like irregular depressions on mare margins (Head, 1974 and Gaddis *et al.*, 1985). Regional deposits consist of more juvenile material than would be expected in Vulcanian deposits, and contain both glass and partially crystalline beads (Gaddis *et al.*, 1985). Volcanic glass is formed when erupted magma droplets occur in an optically thin part of a fountain and are quickly quenched, while crystalline beads are deposited when the droplets are in an optically thick part of the fountain and have time to crystallize before they cool (Arndt *et al.*, 1984 and Arndt and Engelhardt, 1987). Glass and crystalline beads in a single eruption have been observed at Apollo 17 (*i.e.*, the Taurus–Littrow landing site) to have the same geochemical composition (Pieters *et al.*, 1974), but this relationship has not been documented in detail for other regional pyroclastic deposits.

Gaddis *et al.* (2013) identified at least 8 previously unrecognized sites of pyroclastic eruption in the floor of Oppenheimer crater using recently available high-resolution remote sensing data. This discovery increases the number of recognized volcanic vents in Oppenheimer crater to 15 and highlights the importance of pyroclastic volcanism in this and other floor-fractured craters. The presence of at least 15 pyroclastic deposits with a wide variety of sizes and morphologies within a single crater enables me to characterize the composition and occurrence of these deposits at a level not previously possible. In particular, I can assess the influence of local and regional factors such as crustal thickness, subsurface fractures, and crater rays on these volcanic deposits. In this study, I characterize the composition and morphology of the pyroclastic deposits within Oppenheimer crater using near- and thermal-infrared data and visible images from lunar

orbiters to constrain the likely eruption style, mode of occurrence, and resource potential of each deposit.

5.2 Background

Oppenheimer crater is a floor-fractured crater located at 35°S and 166°W (Figure 5.1) within the South Pole–Aitken basin (SPA). Oppenheimer is Pre-Nectarian (Hiesinger *et al.*, 2012) and roughly 200 km in diameter. Figure 5.1 shows the location of Oppenheimer crater and Figure 5.4a shows the distribution of the largest pyroclastic deposits within the crater. The Oppenheimer pyroclastic deposits are associated with vents along fractures in the crater floor. The deposits range in size from 1500 km^2 (northwest deposit) to a few square kilometers (Gaddis *et al.*, 2003 and Gaddis *et al.*, 2013). Most deposits are informally named here for their compass locations within the crater (*e.g.,* Oppenheimer south, Oppenheimer north, *etc.*). Although two of the deposits occur within formally named craters (Oppenheimer U and Oppenheimer H, respectively) on the floor of Oppenheimer, I will refer to these deposits by their compass locations (northwest and southeast) for consistency of naming with other deposits.

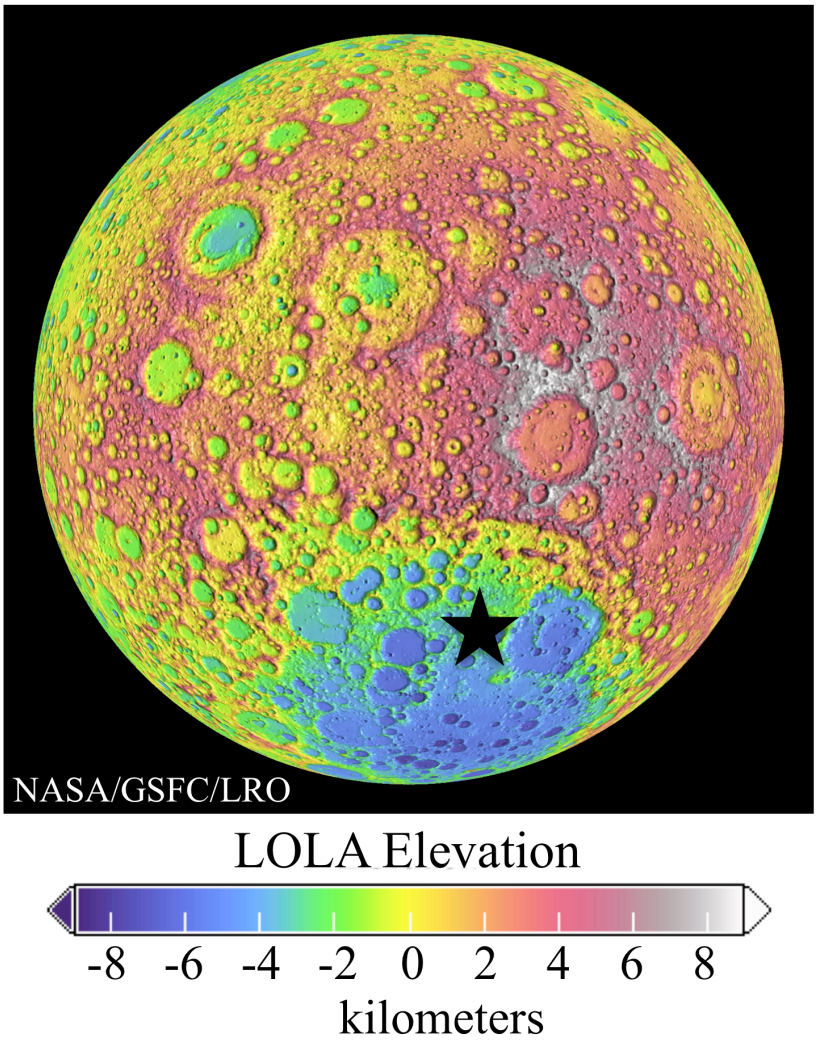

Figure 5.1 LRO Lunar Orbiter Laser Altimeter lunar far-side topographic data (Smith *et al.*, 2009) showing the global context of Oppenheimer crater (black star). Oppenheimer is located within the South Pole-Aitken basin.

Compositional studies using Clementine UVVIS data at Oppenheimer crater showed little diversity between the pyroclastic deposits, suggesting that they had the same magmatic source, with a composition dominated by mafic minerals (*e.g.*, pyroxene) in fragmented basalts and very little, if any, volcanic glass (Petro *et al.*, 2001). One eastern floor deposit showed a composition consistent with lunar highlands material, but this was interpreted to be due to relatively high-albedo impact ejecta lying over the eastern half of the crater. More recent work by Jawin *et al.* (2015) using Moon Mineralogy Mapper near-infrared spectra showed that several of the pyroclastic deposits within Oppenheimer exhibit signatures consistent with volcanic glass.

Although previous studies support an origin by Vulcanian eruption for all deposits in Oppenheimer (Head *et al.*, 2000), the Oppenheimer northwest deposit (within and adjacent to the interior floor-fractured crater Oppenheimer U) could be large enough to be considered a regional deposit (Gaddis *et al.*, 2003) and thus may have formed by the fire fountaining or Strombolian eruption style associated with regional deposits. Therefore, in this study I explore the possibility that the Oppenheimer northwest deposit formed *via* a different eruptive mechanism (fire fountaining/Strombolian), or that this deposit may be unique in that it is a large deposit with a Vulcanian origin (Gaddis *et al.*, 2003).

We also note that the original efforts to classify lunar pyroclastic deposits selected arbitrary areas (2500 km^2, Gaddis *et al.*, 2000; 1000 km^2, Gaddis *et al.*, 2003) as the cutoff between regional and localized deposits. Oppenheimer northwest (1500 km^2) is only a few hundred square kilometers above the 1000 km^2 cutoff, and Oppenheimer south (674 km^2) is only a few hundred square kilometers below this cutoff (Gaddis *et al.*,

2003). Although modeling studies on several deposits show that the size of a deposit generally correlates with its eruption mechanism (Gaddis *et al.*, 2003), in this study I will not assume a particular eruption mechanism for a deposit solely based on its size, since several deposits are similar in size to the arbitrary cutoff.

Our analysis focuses on the compositions of the pyroclastic deposits as a way to distinguish between a fire fountaining or Strombolian *vs*. Vulcanian eruption style; fire fountaining and Strombolian activity should generally produce a deposit with more juvenile material and a more glass-rich composition. In this study, I test the prediction of compositional heterogeneity between the deposits using a variety of data. In contrast to previous studies, I utilize new spectral analysis methods that allow me to assess and map the relative glass content in these deposits. I use thermal- and near-infrared data in tandem, which yields more insight than separate analyses. Thermal infrared data are useful for deriving thermophysical properties and constraining the silicate composition of a material (Vasavada *et al.*, 2012 and Greenhagen *et al.*, 2010). The thermal inertia yields information about the physical characteristics of a material; higher thermal inertia indicates blocky material while lower thermal inertia indicates finer grained particles. The Christensen Feature (CF) value, the emissivity maximum near 8 μm, constrains whether a material is dominantly composed of olivine, pyroxene or plagioclase, the major minerals on the lunar surface. However, the CF value cannot determine whether a material is crystalline or glassy. Also, CF values can be non-unique – for example, a material that is primarily pyroxene would have the same CF value as a material that is a mixture of olivine and plagioclase. Near infrared spectra are thus also used for improved detectability of several iron-bearing minerals (one cannot use near infrared spectra to

easily detect an iron-poor mineral such as plagioclase). Near infrared spectra are also used to detect glass, which exhibits iron absorption bands at different wavelengths than more crystalline minerals (Section 4.2). Therefore, in this study I use near infrared data to help determine whether or not a pyroclastic deposit is glassy, and use thermal infrared data to constrain the composition of the glass. However, it is important to note that these infrared datasets only yield information on the composition and mineralogy of the surface of each deposit.

5.3 Eruption style and resulting deposits

Our aim in this study is to use the composition and mineralogy of the pyroclastic deposits to constrain the eruption style that produced the deposits (Vulcanian *vs*. Strombolian/fire fountaining) and thus to reconstruct the volcanic history of Oppenheimer crater. In Figure 5.2, I illustrate several different types of eruptions and the resulting deposits.Idiscuss a single Vulcanian eruption, multiple Vulcanian eruptions, a Vulcanian eruption followed by a continuous Hawaiian-style eruption, and a single continuous eruption.

(1) Single Vulcanian eruption: Previous models suggest that deposits from Vulcanian eruptions should consist of both crystalline material that has a similar composition as the surrounding terrain and glassy or crystalline juvenile material (Head and Wilson, 1979). However, in considering the mechanics of a Vulcanian eruption, I hypothesize that it is necessary to invoke the concept of superposition and that the deposits may exhibit some stratification. In particular, the country rock and crystalline juvenile material that formed the initial plug should be located at the base of the

pyroclastic deposit as it was the first material to be ejected. Due to break up of the solid plug, this initial deposit should be blocky at LROC resolution. Above this would be crystalline to glassy juvenile material that was ejected after the plug exploded. However, due to the rapid decrease in pressure once the overlying cap fails, an extended eruption of juvenile material is not expected in a purely Vulcanian eruption (Head and Wilson, 1979). Thus, I expect that the fine-grained overlying juvenile material should be a thin deposit, and that the blocky underlying crystalline juvenile material and country rock should be visible. At the resolution of my spectral datasets, this scenario would manifest as a mixture of country rock and juvenile material.

(2) Multiple Vulcanian eruptions: It is also possible that some vents experienced multiple cycles of Vulcanian activity. In this scenario, after the initial Vulcanian eruption, magma that was still slowly rising once again cooled to form a plug and increased the pressure in the conduit. The explosion caused by the overpressure in the conduit would create a deposit that is indistinguishable from a single Vulcanian eruption.

(3) Vulcanian eruption followed by a continuous eruption: If the initial Vulcanian eruption cleared the plug and the magma begins rising more rapidly, a continuous Hawaiian-style eruption could then take place. This would result in a layer of glass-rich juvenile material above the blocky Vulcanian deposit. Depending on how long this continuous eruption persists, the smooth glassy layer could completely obscure the underlying blocky material. The resulting deposit would either appear as glass-rich or glass-rich with some crystalline plug material and country rock.

(4) Immediate continuous eruption: In this scenario, there is no Vulcanian eruption. If magma reaches the surface at ascent rates higher than those expected to

create Vulcanian eruptions, possibly emerging through fractures in the crater floor, a plug does not form and Hawaiian-style fire fountaining commences. The resulting deposit would be glass-rich and could form a small cone around the vent. This deposit is thus indistinguishable from a long-lived continuous eruption that started with a Vulcanian eruption but completely obscures the initial blocky deposit (scenario 3 above).

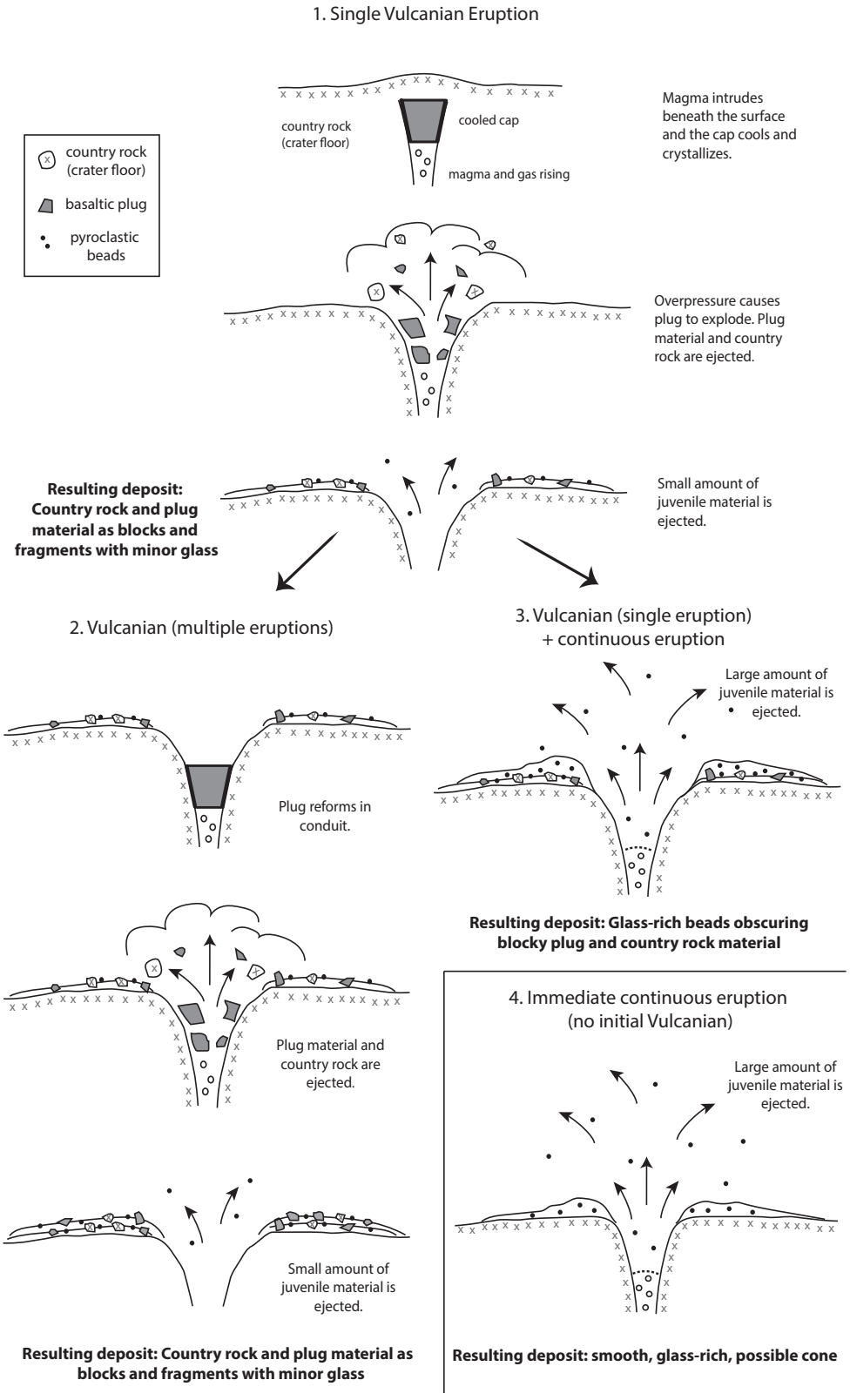

Figure 5.2 Illustration of possible eruption styles and their resulting deposits.

In Figure 5.2 I illustrate that continuous fire fountaining would occur if a plug does not form in the conduit. However, it is also possible that Strombolian activity could occur if the mass eruption rate is low enough. The resulting deposit from a Strombolian eruption would be glass-rich and therefore indistinguishable from fire fountaining deposits in this study. Modeling efforts outside the scope of this study would be necessary to distinguish between Strombolian and fire fountaining activity.

5.4 Methods

In this study I use a variety of remote sensing datasets to study the Oppenheimer crater pyroclastic deposits and their environs, including thermal-infrared data from the Diviner Lunar Radiometer Experiment (Diviner; Paige *et al.*, 2009) on the Lunar Reconnaissance Orbiter (LRO) and visible to near-infrared (VNIR) hyperspectral images from the Moon Mineralogy Mapper (M^3; Pieters *et al.*, 2009 and Green *et al.*, 2011) on Chandrayaan-1.Ialso include LRO Lunar Reconnaissance Orbiter Camera (LROC;Robinson *et al.*, 2010) visible images and Clementine ultraviolet to visible color ratio maps for context (Nozette *et al.*, 1995).

5.4.1 LRO Diviner thermal-infrared datasets

We derive silicate composition, iron abundance, and the thermal inertia of Oppenheimer crater and its pyroclastic deposits from Diviner thermal-infrared data (Paige *et al.*, 2009). I investigate the silicate mineralogy of Oppenheimer through an analysis of the infrared emissivity maximum, or the Christiansen Feature (CF; Greenhagen *et al.*, 2010). The CF value is the wavelength location of the emissivity

maximum (or reflectance minimum), which occurs near 8-μm, but is strongly dependent upon the degree of polymerization of minerals, with framework silicate minerals such as feldspars exhibiting CFs at shorter wavelengths than less polymerized pyroxene and olivine. The Diviner instrument has three channels (3–5) near 8-μm that I use to estimate the CF value. The parabola that fits the three emissivity values from channels 3 to 5 is calculated, and the wavelength that corresponds to the maximum of that parabola is estimated as the CF value. For a more detailed explanation of calculating CF values, see Greenhagen *et al.* (2010). I use Diviner CF values to search for relative abundances of silicate phases such as plagioclase (Glotch *et al.*, 2010) that near-infrared spectra often cannot detect, which could indicate mixing with country rock in Vulcanian-style eruptions.

In order to evaluate the variability of CF values within each deposit and to determine the CF value for the glassiest portion of each deposit,Ireport CF values for several different regions of interest. To obtain the average CF value of each pyroclastic deposit, I created a region of interest for each deposit by outlining the extent of the deposit using visible images and then took the average CF value of each region. To obtain the maximum CF value of a deposit, I visually identified areas within each deposit that exhibited higher CF values than the rest of the deposit and took the average CF of those areas. Not every deposit exhibited areas with enhanced CF values. I also obtained the CF value for glass-rich areas of each deposit by averaging the CF value of all pixels within each deposit that exhibited an M^3 glass band depth above a threshold value. Finally, the CF values for the crater floor were obtained by averaging a section of each side of the crater floor away from the pyroclastic deposits.

We also use Diviner data to estimate iron abundances of lunar pyroclastic deposits. Allen *et al.* (2012) found that the bulk FeO wt% of Apollo soil samples correlated with the CF value (FeO = 74.24∗CF − 599.9; r^2 = 0.90). I use this relationship between FeO abundance and CF values for lunar glasses to estimate the FeO wt% of each deposit (Allen *et al.*, 2012).

Finally, I use Diviner thermal-infrared data to derive the thermal inertia of each deposit, $I = \sqrt{k\rho c_p}$, where k is thermal conductivity, ρ is density, and c_p is heat capacity. I parameterize thermal inertia through the "*H*-parameter", which describes the scale depth of exponential increase, *e.g.*, $\rho(z) \sim e^{-z/H}$. Thermal conductivity is assumed to be proportional to density, and therefore follows the same exponential depth increase. The boundary values on conductivity and density are those of Vasavada *et al.* (2012), with the exception of the surface density, which is $\rho_d = 1100\ kg\ m^{-3}$. For each map element, I perform a least-squares minimization on the nighttime regolith temperatures from Diviner, to derive the *H*-parameter. The *H*-parameter is inversely related to thermal inertia, with larger *H* values indicate lower thermal inertia within the upper ~10 cm.

Regional lunar pyroclastic deposits typically exhibit lower nighttime temperatures than the lunar regolith, which implies that they have lower thermal inertia (Bandfield *et al.*, 2011) and can yield insight on the particle sizes and shapes in the deposits. For example, spherical pyroclastic beads of juvenile material could stack in an organized way creating more pore space and lowering the thermal inertia, while deposits with higher country rock content could have a thermal inertia similar to the average lunar regolith.

5.4.2 M^3 visible to near-infrared spectral maps

We use M^3 visible to near-infrared spectra (0.43–3.0 μm) to characterize the iron-bearing minerals and glasses within Oppenheimer crater. M^3 Level 2 reflectance data from the global mapping campaign is acquired from the Planetary Data System, which includes corrections for thermal emission as well as topographic, photometric, and instrumental effects (Green *et al.*, 2011, Clark *et al.*, 2011, Hicks *et al.*, 2011, Boardman *et al.*, 2011 and Besse *et al.*, 2013). Here I use two images from high signal to noise ratio (SNR) operational periods (M3G20090621T022743 and M3G20090621T065503), which cover the eastern half of the crater, and two images from low SNR operational periods (M3G20090815T074952 and M3G20090718T101402;), which cover the west and the northeast rim of the crater. All images are from the "2C" period of the mission when the spacecraft operated from a higher orbit, so the native resolution of all four images is ~280 m/pixel (two times lower resolution than the global data from earlier in the mission). There is a coverage gap between these images (*e.g.* Figure 5.5). There is no M^3coverage over part of the western half of Oppenheimer crater where the centers of the northwest and southwest pyroclastic deposits are located. These images are mapped into a mosaic with a local cylindrical projection at 140 m/pixel horizontal resolution.

Iron-bearing minerals can be identified in M^3 data based on the position and shape of the 1 and 2 μm iron absorption bands, which vary significantly with mineralogy and composition (*e.g.,* Adams, 1974, Cloutis and Gaffey, 1991, Sunshine and Pieters, 1993 and Horgan *et al.*, 2014). See Figure 5.3 for examples of near-infrared spectra of iron-bearing minerals typically found on the Moon. The wavelength range of M^3 covers both of the broad 1 and 2 μm absorption bands, and the 82 spectral band global dataset is

ideal in particular for analysis of the 1 μm band, with 2× higher spectral sampling in the 0.7–1.6 μm region.

Before the 1 and 2 μm iron absorption bands can be analyzed in detail, however, the overall continuum slope must be suppressed by removing an approximate continuum function. In analyzing a wide variety of lunar terrains, I find that the simplest continuum shape that fits most lunar spectra is a linear convex hull, where linear continua are found independently over the 1 and 2 μm band regions (*e.g.*, Clark and Roush, 1984). To find the continuum function, I first smooth each spectrum with nested boxcar average and median smoothing functions, both 3 channels wide. Then, I remove an initial estimate of the continuum, fit to fixed endpoints at 0.7, 1.5, and 2.6 μm. Next I fine-tune these endpoints for each spectrum by finding the local maxima in this initial continuum removed spectrum. For the 1 μm region, I find the local maxima between 0.6–1.0 and 1.0–1.7 μm, which become the new endpoints. For the 2 μm region, local maxima are found between the previous endpoint (between 1.0 and 1.7 μm) and 2.0 μm and 2.0–2.6 μm. These ranges avoid both possible long-wavelength plagioclase absorptions near 1.3 μm and thermal effects beyond 2.6 μm. Using the new endpoints, the final continuum of three joined linear segments is calculated from the original spectrum.

We use the methods of Horgan *et al.* (2014) to map the position of the 1 and 2 μm iron absorption bands, which are indicators of iron mineralogy. Band position is parameterized as band center, calculated as the wavelength position of the minimum of a fourth-order polynomial fit to the spectrum within 0.1 μm of the minimum channel in each band. Band depth is the percent depth below the continuum at the location of the band center (*i.e.*, one minus the value of the continuum removed spectrum at that

wavelength). The 1 and 2 μm band positions together can be used to broadly distinguish between orthopyroxene (OPX; band centers between 0.9–0.94 and 1.8–1.95 μm), clinopyroxene (CPX; 0.98–1.06 and 2.05–2.4 μm), and iron-bearing glass (1.06–1.2 and 1.9–2.05 μm). Mixtures of these minerals have band centers that fall in the intermediate regions between the endmembers (Horgan *et al.*, 2014). Other iron-bearing minerals can also be identified using similar methods. Olivine exhibits a characteristically asymmetric 1 μm band typically centered near 1.05–1.08 μm and plagioclase feldspars exhibit broad and shallow bands centered between 1.25 and 1.35 μm, but neither exhibits a corresponding 2 μm band.

One drawback of only using band centers when trying to identify glass in a mixture is that glass is a poor absorber compared to other iron-bearing minerals, and thus glass only significantly shifts the 1 and 2 μm band centers when it is present at very high abundances (typically 50–80 wt%; Horgan *et al.*, 2014). However, low to moderate glass abundances can still cause additional absorption beyond 1.1 μm, where other minerals are not as strongly absorbing. Thus, I have developed a "glass band depth" spectral parameter to aid in identifying glass at lower abundances, which is equal to the average of the depth below the continuum at three wavelengths: 1.15, 1.18, and 1.20 μm. This parameter will detect glass, but will also detect olivine if present.

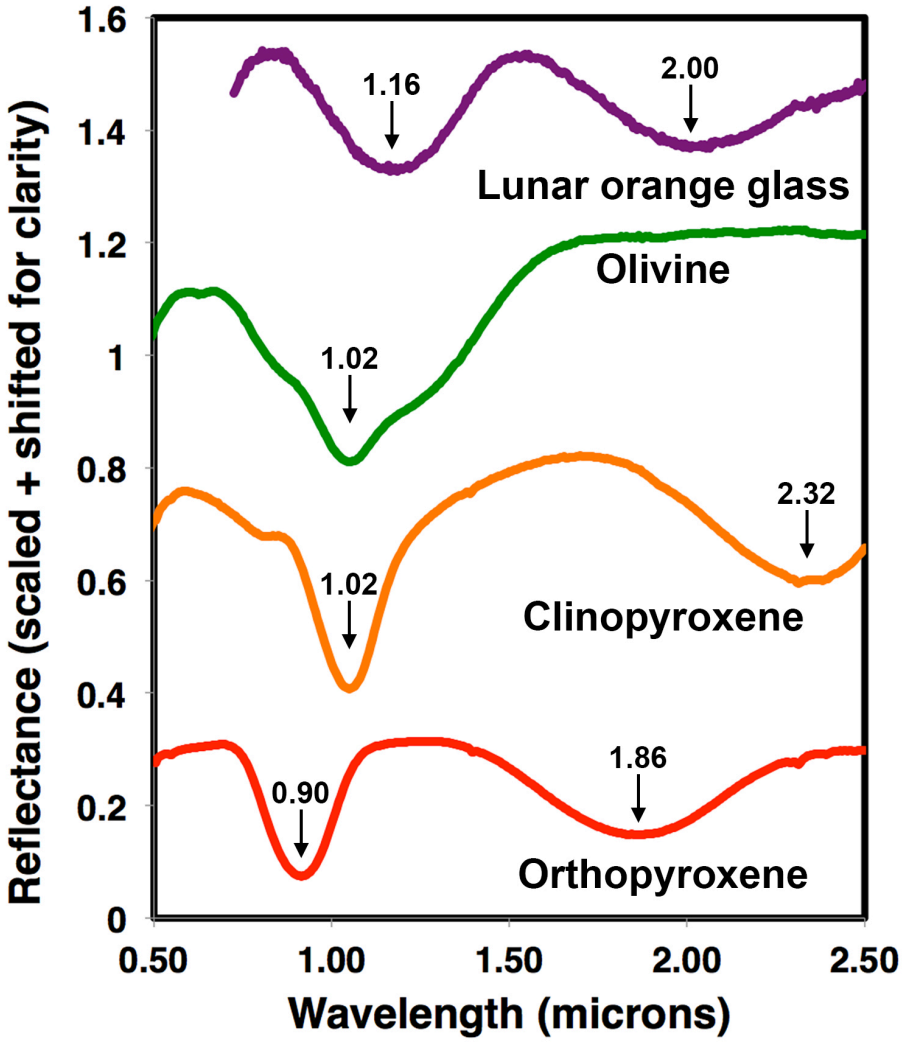

Figure 5.3 Laboratory spectra of typical examples of iron-bearing minerals discussed in this study, including Apollo orange glass, which is interpreted to be pyroclastic in origin (Adams *et al.*, 1974). All spectra are continuum removed, shifted and scaled for clarity, and labeled with their calculated 1 and 2 micron band centers.

5.4.3 Additional data sets

I use LROC wide angle camera (WAC) mosaics and narrow angle camera (NAC) images to provide context for my composition and mineralogy study (Robinson *et al.*, 2010). I use the global WAC mosaic available on JMARS for the Moon (Christensen *et al.*, 2009) and individual calibrated NAC images that are currently available from the PDS. These LROC products are used to study the morphology and albedo variations of pyroclastic deposits within Oppenheimer crater. I also use Clementine color ratio maps that are publicly available on JMARS for the Moon (McEwen and Robinson, 1997 and Christensen *et al.*, 2009). In Clementine color ratio maps, red is 750/415 nm, green is 750/950 nm, blue is 415/750 nm. These maps cancel out the dominant brightness variations from albedo and topography and highlight color differences dues to mineralogy and maturity. I use these maps to provide context for Oppenheimer, especially with respect to the influence of crater ejecta and rays on observed remote sensing signatures.

5.5 Results

5.5.1 Diviner results

Figure 5.4 shows the CF map of Oppenheimer crater and Table 5.1 shows the average CF value of each pyroclastic deposit as well as the crater floor. Observed CF values range from roughly 8.15–8.40 μm, with much of the crater floor showing comparable values to nearby highlands, at 8.15–8.2 μm. All pyroclastic deposits have a higher CF value than the crater floor, but the large western pyroclastic deposits (south, southwest, northwest) exhibit higher CF values (8.28–8.33 μm, with areas of enhanced

CF values that reach as high as 8.48 μm) than the smaller eastern deposits (north, east, southeast, south–southeast; 8.25–8.27 μm). This may or may not be related to the observation that the western crater floor also has a higher CF than the eastern crater floor. A fresh impact crater (indicated by the arrow in Figure 5.4c) near the north pyroclastic deposit has the lowest CF value in the study area (8.07 μm). I converted the Diviner CF values to FeO wt% (Table 5.1). Since iron abundance correlates with CF values, the same trends observed in the CF values apply to the FeO wt%. The western pyroclastic deposits have an FeO abundance of 15–19 wt%, while the eastern pyroclastic deposits have 13–14%. The areas of enhanced CF within the northwest, southwest and south deposits have FeO abundances of 30 ± 11, 23 ± 6, and 26 ± 10 wt%, respectively.

Figure 5.4c shows the *H*-parameter (the inverse of thermal inertia) of Oppenheimer crater. The thermal inertia calculations presented here do not fully account for slope variations, which is why the crater walls and rim are apparent in Figure 5.4c. As I am primarily interested in the crater floor and pyroclastic deposits, where slopes are small, this does not strongly affect my results. The crater floor and the pyroclastic deposits have *H*-parameter values ranging from 0.08 to 0.10, and the *H*-parameter value for each pyroclastic deposit is the same as its surrounding crater floor material. The largest variation in thermal inertia is the small, fresh impact crater near the northern pyroclastic deposit that has an *H*-parameter value of −0.2 (arrow in Figure 5.4c; also see Table 5.1). Fresh impact craters usually exhibit higher thermal inertia values, and therefore lower *H*-parameter values, due to the high abundance of small rocks in the ejecta. The negative value at the fresh crater implies that the thermal inertia in the upper ~10 cm is higher than the maximum value allowed by the standard model

(~90 J m^{-2} K^{-1} $s^{-1/2}$). A different model, with higher limiting thermal inertia, would be needed to accurately describe this area. Apart from this fresh impact crater, the largest variation in thermal inertia is between the higher *H*-parameter (lower thermal inertia) western half of the crater floor and the lower *H*-parameter (higher thermal inertia) eastern half.

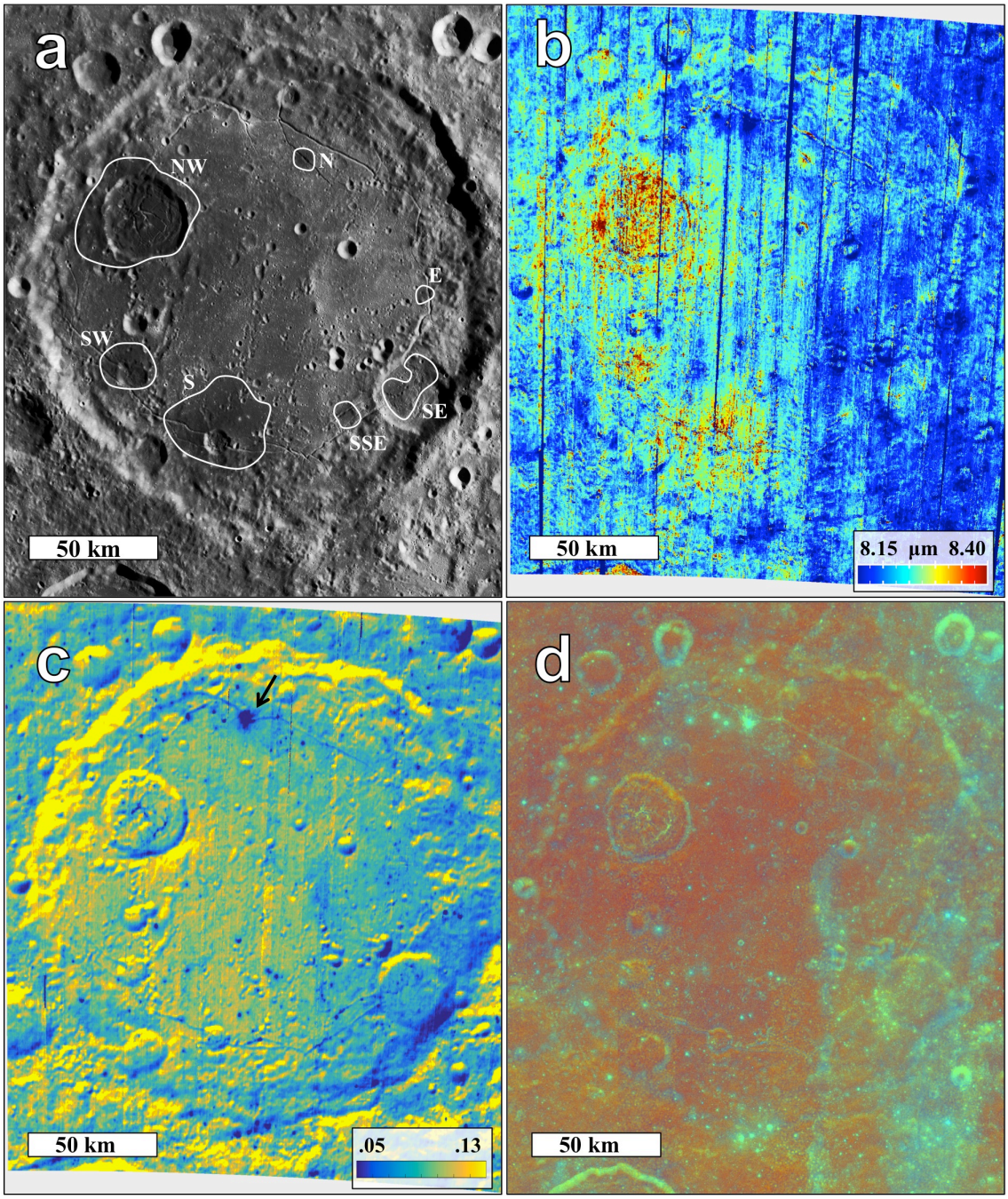

Figure 5.4 a) LROC WAC mosaic of Oppenheimer crater from the global mosaic available on JMARS for the Moon (Robinson *et al.*, 2010; Christensen *et al.*, 2009). The 7 largest pyroclastic deposits are outlined and labeled. b) Diviner CF map of Oppenheimer crater. c) H-parameter (inverse thermal inertia) of Oppenheimer crater. The

black arrow points to a fresh crater. d) Clementine color ratio of Oppenheimer crater available on JMARS for the Moon (McEwen *et al.*, 1997; Christensen *et al.*, 2009). The light green terrain in the eastern part of Oppenheimer is hypothesized to be a crater ray.

Table 5.1 Average Diviner-derived CF values, FeO, and thermal inertia for all deposits. Where deposits are large enough to exhibit significant variation, the maximum value for the CF and corresponding FeO are also shown in parentheses.

Deposit or Unit	**CF Value (μm)**	**FeO (wt. %)**	**Thermal Inertia (H-parameter)**
Pyroclastic Deposits			
NW	8.33 ± .03 *(8.48 ± .15)*	19 ± 2 *(30 ± 11)*	0.10 ± 0.01
SW	8.31 ± .07 *(8.39 ± .08)*	17 ± 5 *(23 ± 6)*	0.10 ± 0.01
S	8.28 ± .06 *(8.43 ± .16)*	15 ± 4 *(26 ± 10)*	0.10 ± 0.01
SSE	8.25 ± .03	13 ± 2	0.08 ± 0.01
SE	8.25 ± .04	13 ± 3	0.08 ± 0.01
E	8.26 ± .04	13 ± 3	0.08 ± 0.01
N	8.27 ± .06	14 ± 4	0.10 ± 0.01
Non-pyroclastic Deposits			
W crater floor	8.24 ± .03	12 ± 2	0.10 ± 0.01
E crater floor	8.20 ± .03	9 ± 2	0.08 ± 0.01
Fresh Crater	8.07 ± .06	-1 ± 4	-0.20 ± 0.10

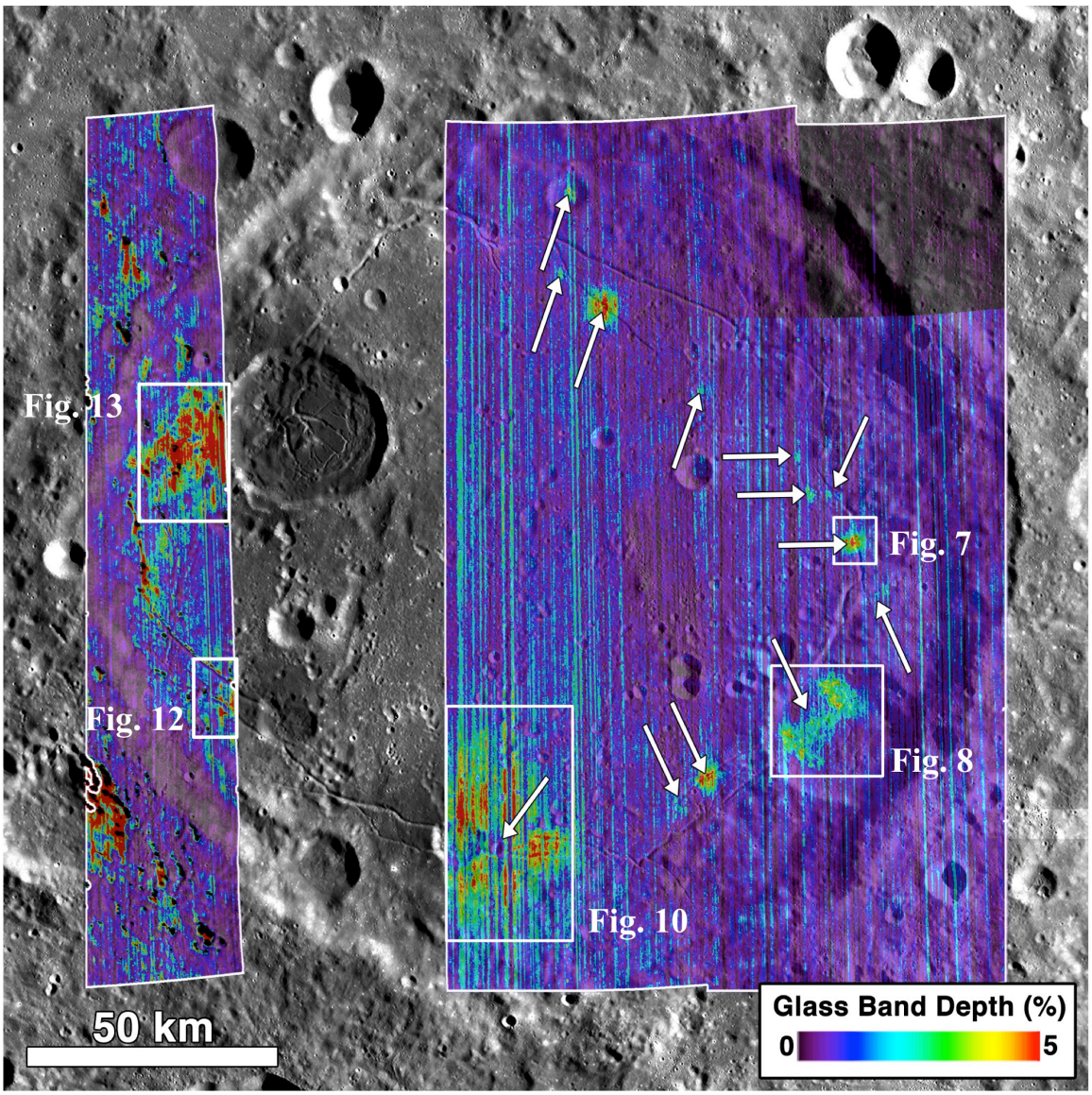

Figure 5.5 M^3 glass band depth spectral parameter mapped in Oppenheimer crater, with LROC WAC mosaic from Figure 5.4 as background. See Section 3.2 for M^3 image names. This spectral parameter indicates enhanced absorption between 1.15-1.20 μm in continuum removed spectra, consistent with glass. Arrows indicate sites of inferred pyroclastic deposits based on glass detections. Boxes indicate locations of deposits shown in detail in Figures 11, 12, 14, 16 and 17.

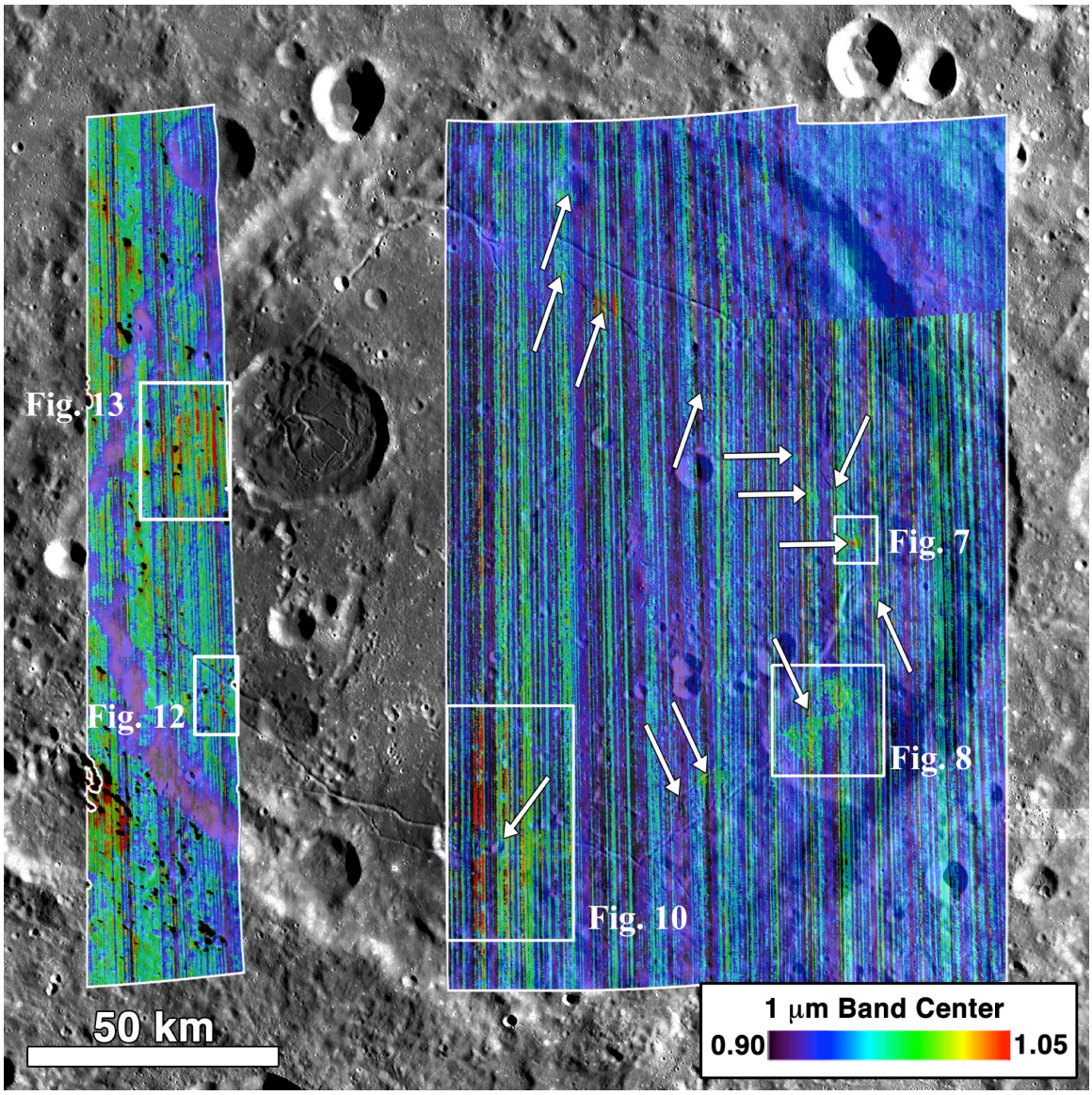

Figure 5.6 M^3 1 μm band center mapped in Oppenheimer crater (superimposed on LROC WAC mosaic). See Section 3.2 for M^3 image names. Arrows indicate sites of inferred pyroclastic deposits based on glass detections. Boxes indicate locations of deposits shown in detail in Figures 11, 12, 14, 16 and 17. High values (yellow to red) are consistent with iron-bearing glass, while moderate values (cyan to green) are consistent with clinopyroxene, clinopyroxene-glass mixtures, or orthopyroxene-glass mixtures.

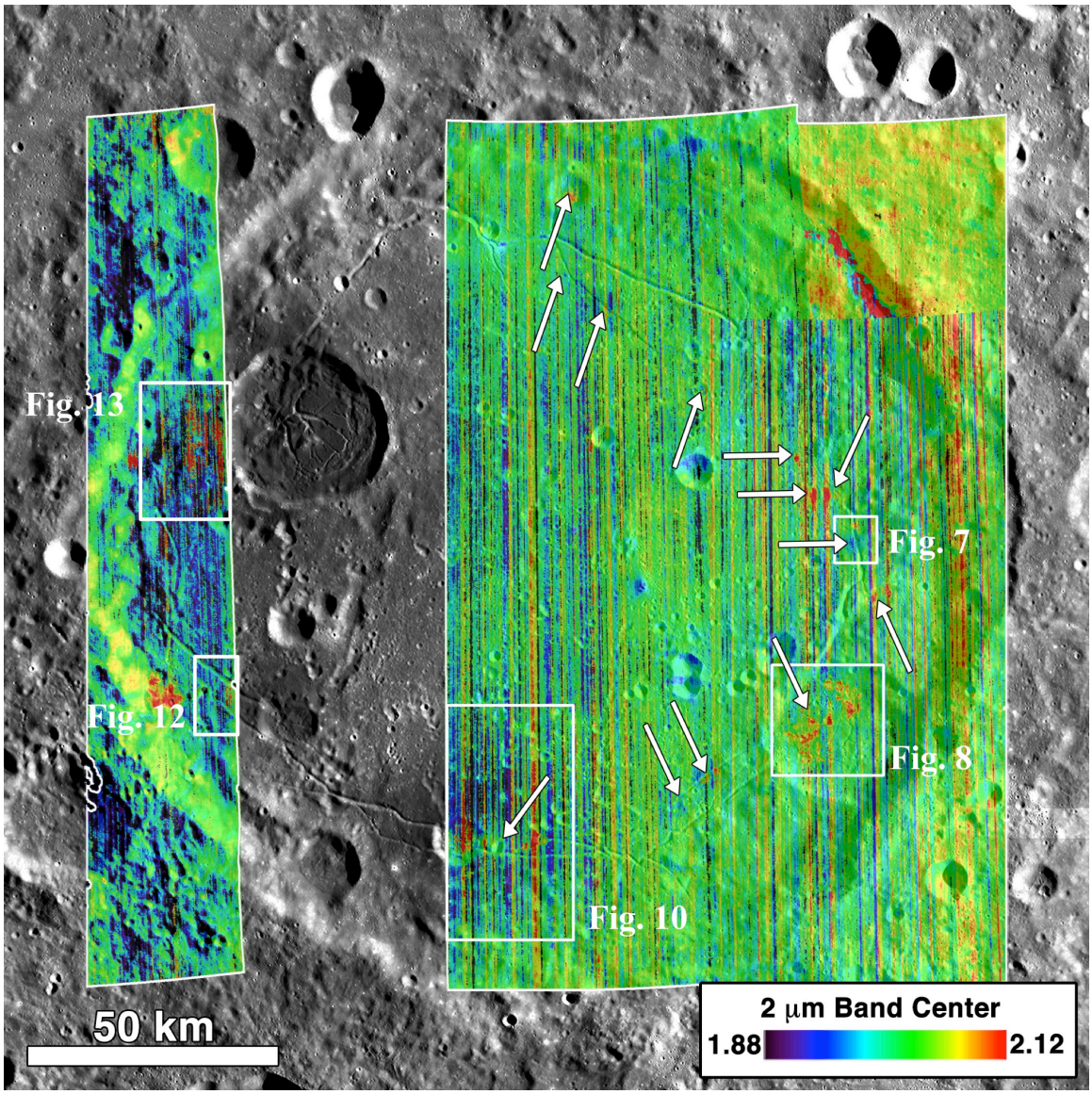

Figure 5.7 M^3 2 μm band center mapped in Oppenheimer crater (superimposed on LROC WAC mosaic). See Section 3.2 for M^3 image names. Arrows indicate sites of inferred pyroclastic deposits based on glass detections. Boxes indicate locations of deposits shown in detail in Figures 11, 12, 14, 16 and 17. High values (yellow to red) are consistent with clinopyroxene, while low values (purple to blue) are consistent with iron-bearing glass.

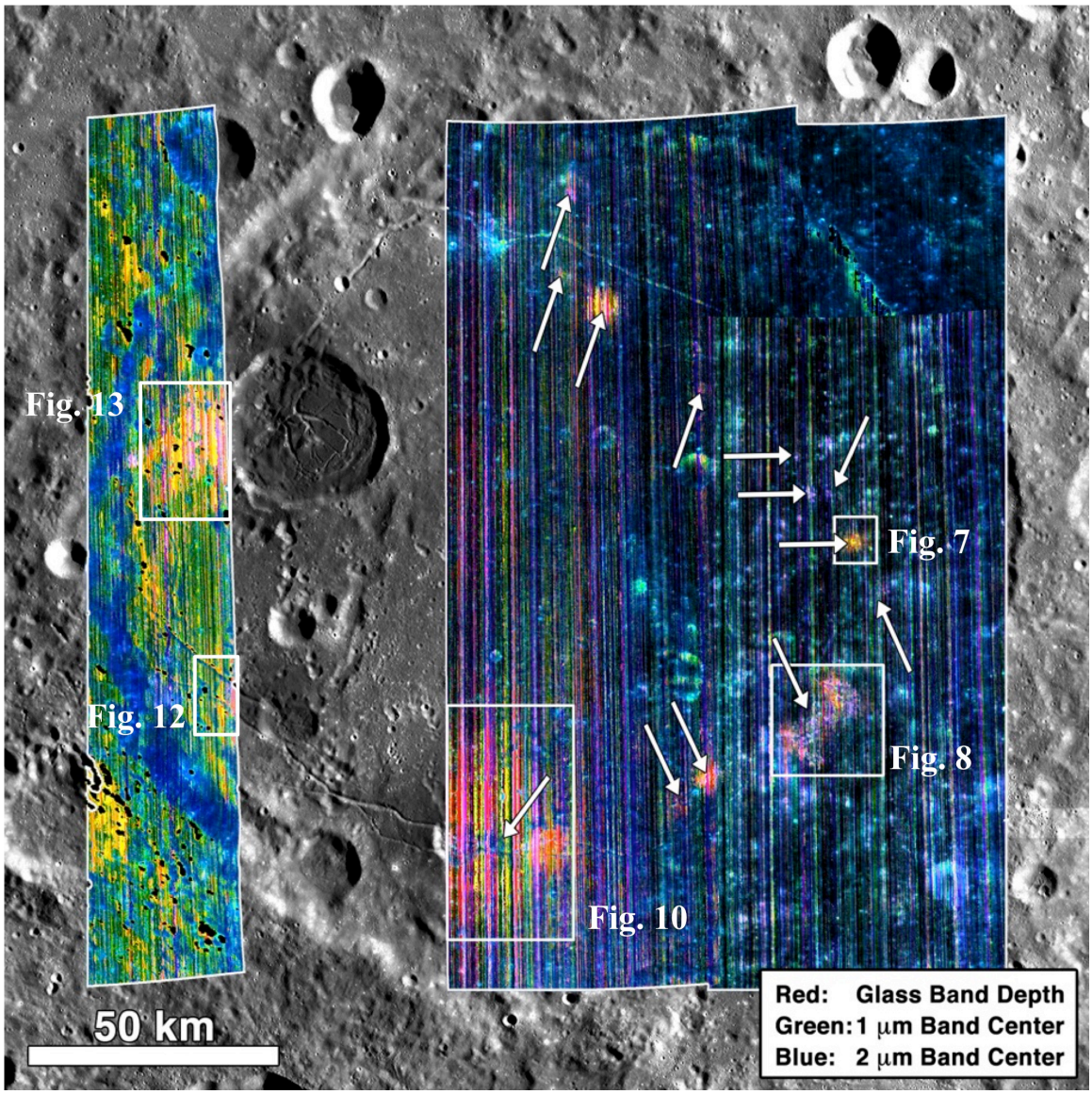

Figure 5.8 M^3 RGB composite map of Oppenheimer crater, with LROC WAC mosaic from Figure 3 as background. Red = Glass band depth (Figure 5.5; stretched from 0.1-3%), Green = 1 μm band center (Figure 5.6; stretched from 0.9-1.05 μm), Blue = 2 μm band center (Figure 5.7; stretched 1.95-2.25 μm). CPX mixed with glass is magenta, glass is yellow, OPX is green, OPX mixed with CPX is teal to blue (see Table 5.2 for more detailed explanation of color scheme). The five white boxes show the areas of additional figures where further analysis is presented.

Table 5.2: This table lists each mineral (or glass), its relevant spectral properties, and its corresponding color in Figure 5.8. For example, glass has a high glass band depth and 1 mm band center, and a low 2 mm band center. Therefore, its red value is high, its green value is high, and its blue value is low. This corresponds to yellow since the RGB value for yellow is 255, 255, 0.

Material	**Red** *Glass Band Depth*	**Green** *1 mm Band Center*	**Blue** *2 mm Band Center*	**Mapped Color**
Glass	High	High	Low	Yellow
OPX	Low	Low/Mod	Low	Green
CPX	Low	Moderate	High	Blue
OPX+CPX	Low	Low/Mod	Moderate	Teal/Blue
Glass+CPX	High	Moderate	Moderate	Magenta

5.5.2 M^3 results

Figure 5.4 shows the M^3 glass band depth parameter across Oppenheimer crater and Figure 5.7 shows an RGB composite of these three maps, with the red channel corresponding to the glass band depth parameter, the green channel the 1 μm band center (see Figure 5.6), and the blue channel the 2 μm band center (see Figure 5.7). In this color scheme, I interpret that glass-rich areas are yellow, CPX and glass mixtures are magenta, OPX-dominated areas are green, and CPX/OPX mixtures are teal or blue. See Table 5.2 for more details about this color scheme.

Analysis of M^3 spectra shows clear spectral differences between the crater floor and the pyroclastic deposits, as well as within and between the various pyroclastic deposits. All reported band center ranges reported here are one standard deviation on either side of the mean, for spectra with 1 and 2 μm band depths greater than 2%. Figure 5.9a shows a density plot of the 1 and 2 μm band centers of the crater, along with approximate ranges for OPX, CPX, and glass-dominated spectra based on my local analyses. The densest portion of Figure 5.9a corresponds to the crater floor, which tends to fall both within the OPX field and between the OPX and CPX fields. This general range encompasses both the lateral and vertical diversity in the composition of the crater floor. The eastern half of the crater floor exhibits 1 and 2 μm band centers between 0.90–0.98 and 1.99–2.06 μm, consistent with an OPX/CPX mixture. The western crater floor exhibits similar 1 μm band centers but 2 μm band centers shifted lower, between 1.93 and 2.02 μm. Many crater walls, fracture walls, and fresh craters in the eastern crater floor also exhibit shifted band centers, typically between 0.91–0.94 and 1.96–1.99 μm.

The west and central-eastern crater floor both exhibit small but positive values of the glass band depth parameter (1–3%).

In comparison, the pyroclastic deposits exhibit much larger values of the glass band depth parameter (3–8%). This makes the glass band depth parameter very useful for identifying pyroclastic deposits, even deposits smaller than a few kilometers across. For example, the arrows in Figure 5.5 point to 13 deposits that are detectable using the glass band depth parameters. There are also two larger deposits on the western side of the crater that are not entirely covered with M^3 data, which brings the total of pyroclastic deposits to 15 within Oppenheimer crater. This agrees with the number of pyroclastic deposits identified in Gaddis *et al.* (2013). However, the glass band depth parameter alone is not sufficient to uniquely identify glass, as it could also indicate olivine. I do not observe any spectroscopic evidence for olivine in the area, though, as all locations with greater glass band depths exhibit both longer wavelength 1 μm band centers and shorter wavelength 2 μm band centers. The shift to longer 1 μm band centers and shorter 2 μm band centers is apparent at the scale of the map in Figs. S1 and S2 in the Supplementary material. While olivine would be expected to shift the 1 μm band center to longer wavelengths, it would not be expected to shift the 2 μm band center at all. This shift in both bands is consistent with the presence of iron-bearing volcanic glass in Oppenheimer crater pyroclastic deposits (Horgan *et al.*, 2014).

The spectral character of the central portions of the pyroclastics varies from glass-rich to CPX/glass mixtures. Only one deposit (south) exhibits signatures of OPX in its interior. An example of a glass-rich deposit is the east deposit, and a detailed analysis of this deposit is shown in Figure 5.11. The plotted M^3 spectra show a progression from

spectra consistent with an OPX/CPX mixture that is representative of the eastern crater floor (Figure 5.11, spectrum 1) to the glass-rich pyroclastic materials (Figure 5.11, spectrum 3). This progression is also shown by the clear linear trend in 1 and 2 μm band centers from those consistent with OPX/CPX mixtures to those consistent with glass in Figure 5.9b. Indeed, the very high 1 μm band centers in this deposit (1.09–1.13 μm) are consistent with lab spectra of mixtures containing more than 70–80 wt% glass (Horgan *et al.*, 2014).

In contrast, Figure 5.12 shows a similar analysis of the southeast deposit, which I interpret as consisting of a mixture of CPX and glass. Figure 5.13 shows LROC NAC images of this deposit for context (discussed in more detail in Section 4.4). As indicated in Figure 5.9c, many areas within this deposit exhibit 1 and, in particular, 2 μm band centers at longer wavelengths than the surrounding crater floor, which is consistent with the presence of CPX (Figure 5.12, spectrum 2). However, these spectra also exhibit a shoulder on the 1 μm CPX band near 1.2 μm consistent with a glass component. While this shoulder could be due to a secondary CPX band that can occur in some very high Ca and/or Fe CPX (Klima *et al.*, 2011 and Trang *et al.*, 2013), local context suggests that glass is more likely. Other areas within the deposit exhibit much stronger shoulders along with longer wavelength 1 μm band centers and shorter wavelength 2 μm band centers, all consistent with higher glass abundances, albeit still mixed with CPX (Figure 5.12, spectrum 3).

The rest of the pyroclastic deposits in Oppenheimer crater vary from glass-rich to glass and CPX mixtures. Some deposits, such as the south deposit, show spectral variation within the deposit. In some areas, this deposit is glass-rich (Figure 5.14,

spectrum 4) and in others it is a CPX/glass mixture (Figure 5.14, spectrum 2). Figure 5.15 shows LROC WAC and NAC images of the south deposit for context (discussed in more detail in Section 4.4). This deposit also exhibits OPX signatures. A spectrum taken from a fracture within the south deposit is similar to the underlying OPX-rich crater floor (Figure 5.14, spectrum 3), while central portions of the deposit are more spectrally similar to the possible mixed OPX/CPX mantle in the eastern crater (Figure 5.14, spectrum 1). In the south deposit in particular, significant striping of unknown origin (but presumed to be noise) in the M^3 data within the dark deposit makes highly local variability difficult to assess. However, there do appear to be real spectral variations between the main lobe and the eastern lobe of the deposit, with a more widely distributed CPX component to the east (Figure 5.14, spectra 2 and 4). The available data over the northwest and southwest deposits, while also noisy, also appears to show variation in glass and CPX concentrations (Figure 5.16).

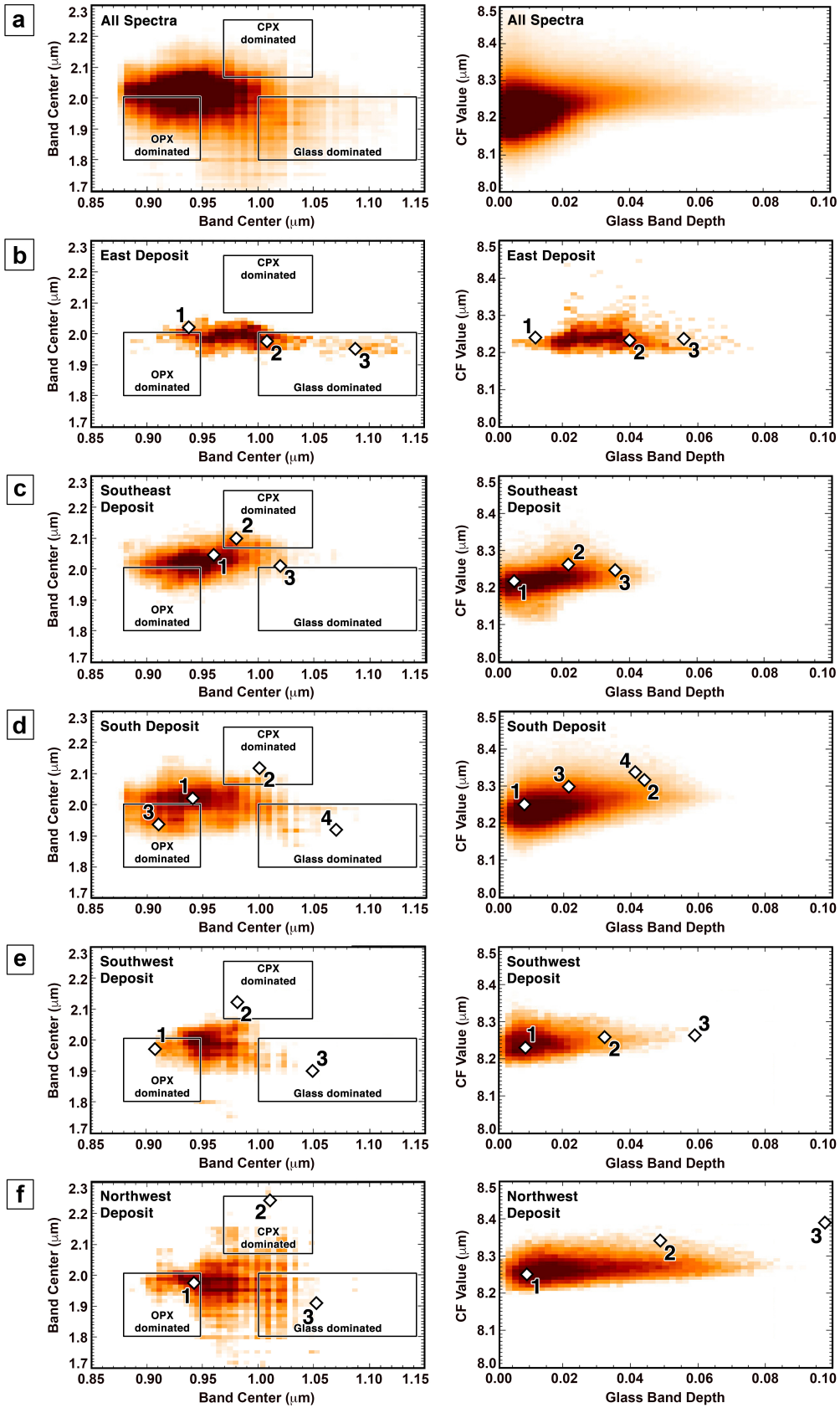
a
All Spectra
CPX dominated
OPX dominated
Glass dominated
Band Center (μm)
CF Value (μm)
Glass Band Depth
b
East Deposit
c
Southeast Deposit
d
South Deposit
e
Southwest Deposit
f
Northwest Deposit

Figure 5.9 Density plots illustrating spectral variability across the entirety of Oppenheimer Crater as well as within individual deposits. Darker orange colors indicate a higher density of spectra. The numbered points in each plot refer to spectra shown from each deposit in Figures 11, 12, 14, 16, and 17. The left column shows M^3 1 and 2 μm band centers for all spectra with 1 μm band depths > 5%, with parameter ranges expected for OPX, CPX and glass-dominated mixtures noted (Horgan *et al.*, 2014). The right column shows Diviner CF values vs. M^3 glass band depths, and illustrates the relatively narrow range of CF values exhibited by glassy materials.

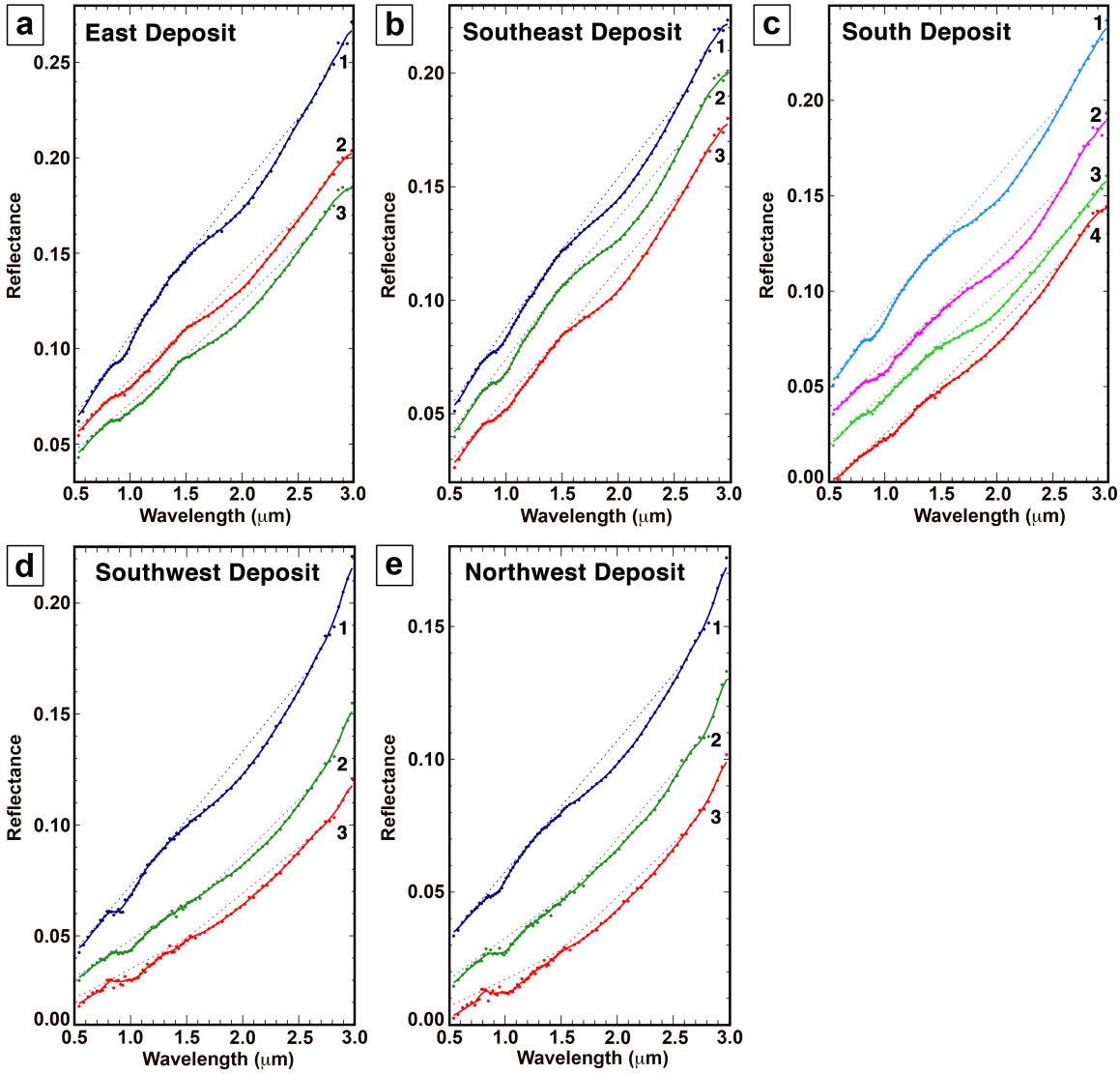

Figure 5.10 Reflectance spectra from within pyroclastic deposits corresponding to the continuum-removed spectra from Figures 11, 12, 14, 16 and 17. Points are actual spectral average, line is the smoothed spectrum, and dashes indicate the continuum fit.

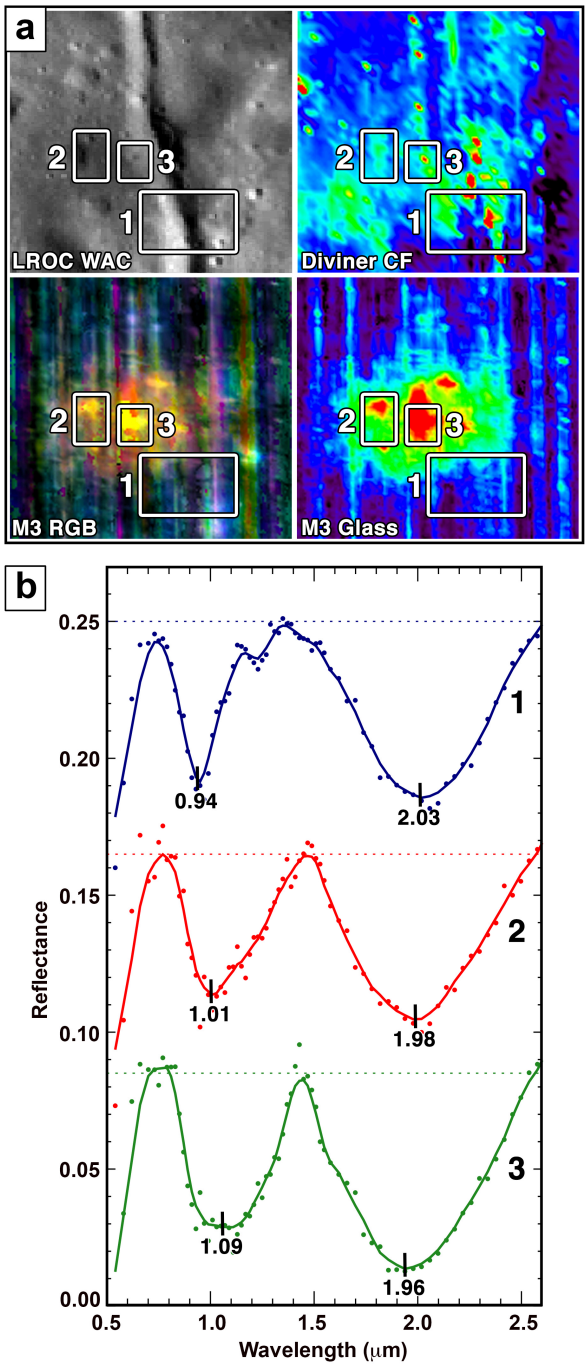

Figure 5.11 Detailed analysis of the eastern deposit, as indicated in Figure 5.5. This deposit is glass-rich, with no indication of significant CPX. (a) Enlarged maps of deposit from Figures 5.4 a and b, 5.5, and 5.8. (e) Continuum removed spectra, with calculated band centers noted.

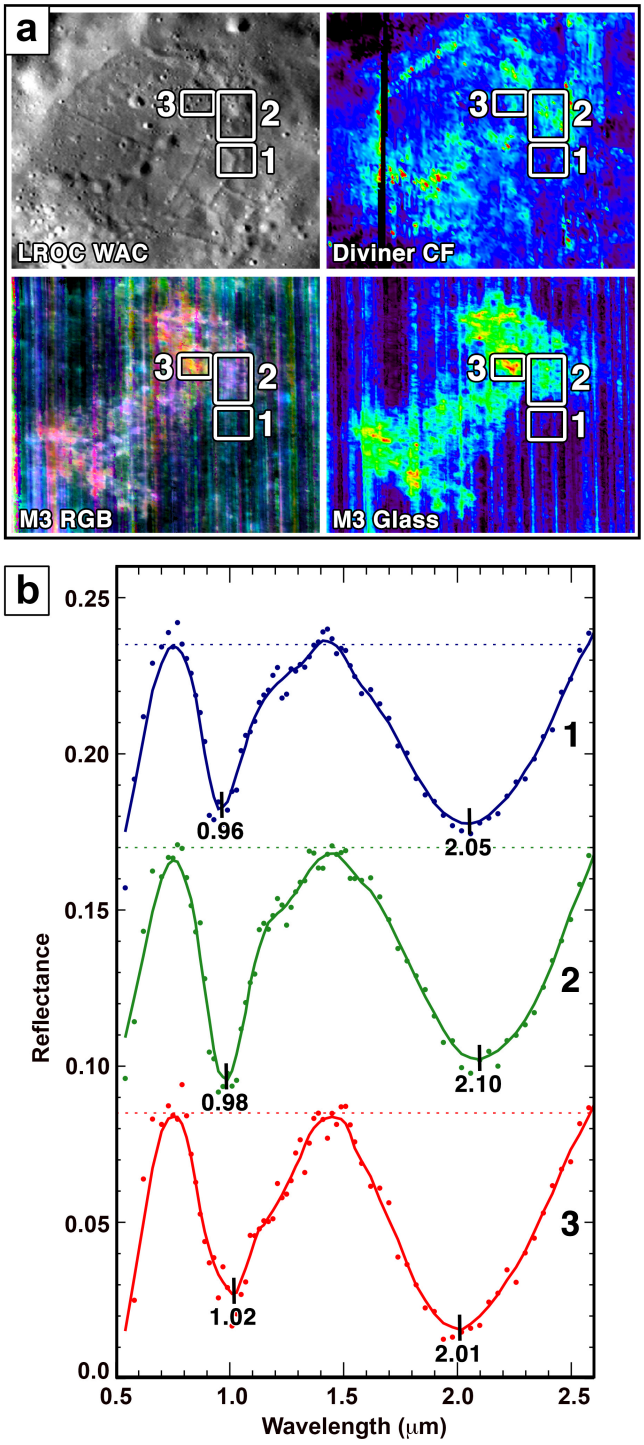

Figure 5.12 Detailed analysis of southeastern deposit, as indicated in Figure 5.5. This deposit is primarily a mixture of CPX and glass. See Figure 5.11 caption for description of individual parts.

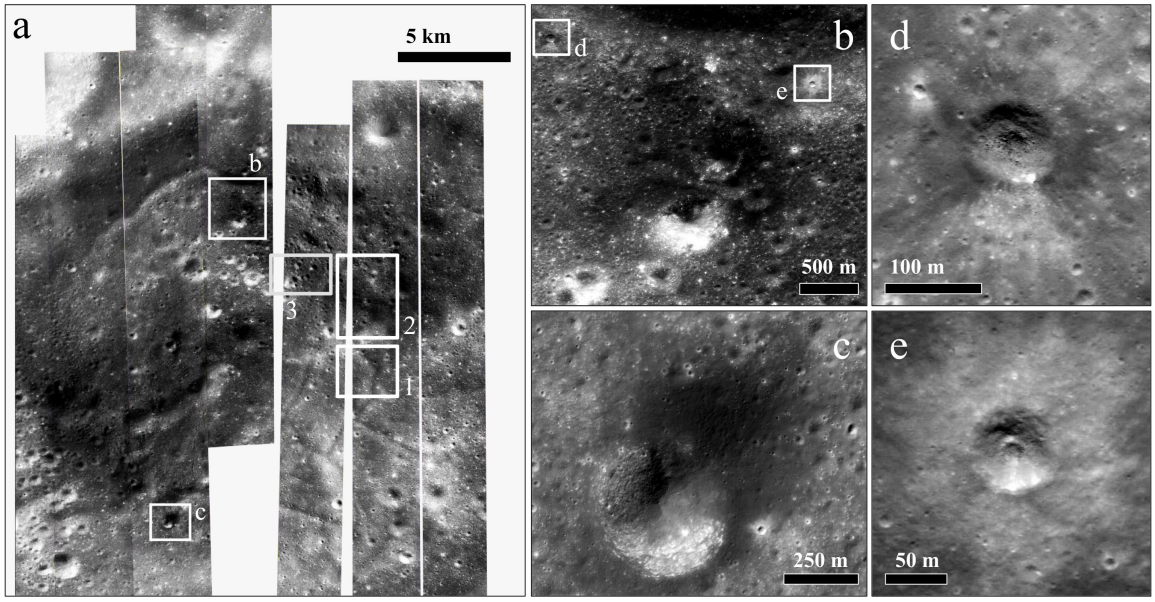

Figure 5.13 a) NAC mosaic of the SE deposit. Boxes labeled 1-3 show the location of spectra from Figure 5.12. b) (M171632283RE) and c) (M1099924536RE) Areas showing distinct low albedo mantling deposits within the SE deposit. d) and e) show bench craters within the SE deposits that indicate a bolide impacted into layered material, possibly loose pyroclastic material over a lava flow. The crater in (d) is ~85 m in diameter and the crater in (e) is ~65 m in diameter.

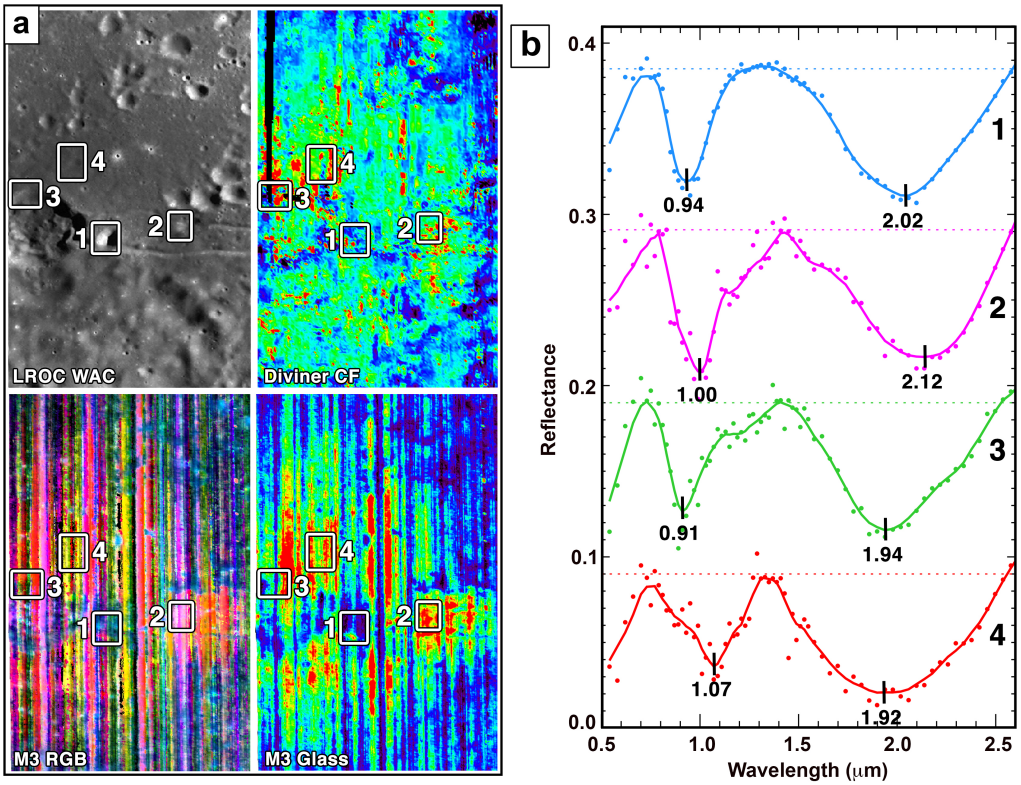

Figure 5.14 Detailed analysis of complex southern deposit, as indicated in Figure 5.5. This deposit exhibits glass-rich areas, CPX/glass mixtures, as well as OPX-rich country rock. See Figure 5.11 caption for description of individual parts.

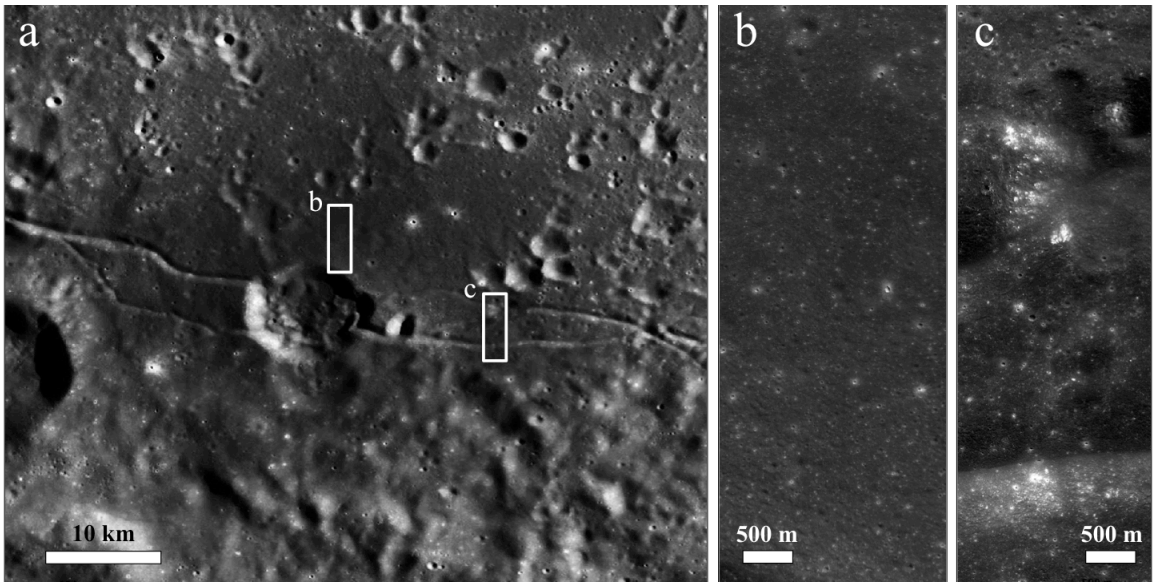

Figure 5.15 a) LROC WAC image of the S deposit. b) NAC (M1119966094LE) of the glass-rich area that roughly corresponds to spectra 4 from Figure 5.14. c) NAC (M110316969RE) of the CPX-rich area that roughly corresponds to spectra 2 from Figure 5.14. The depression in the top of the image could be a vent, the depression in the bottom part of the image is a fracture in the crater floor.

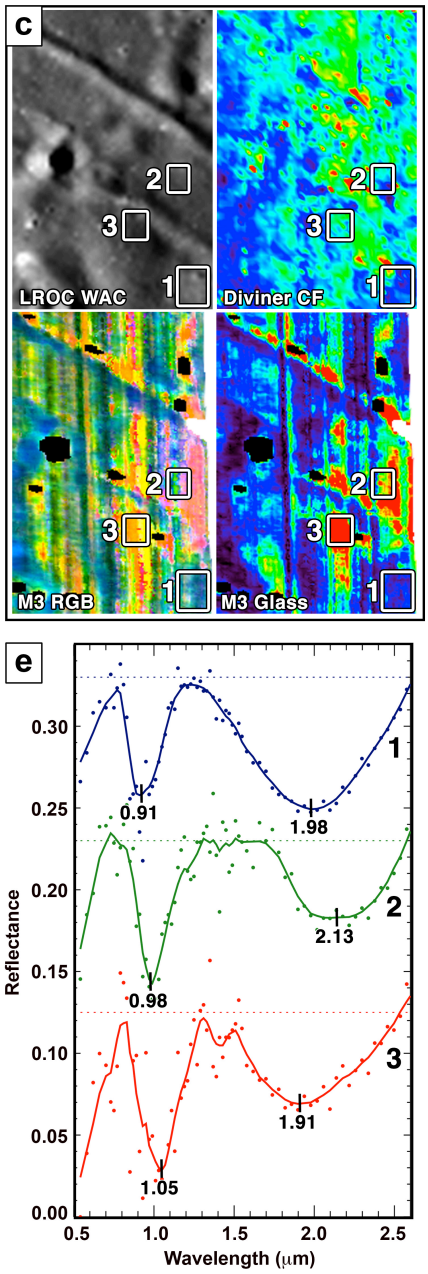

Figure 5.16 Detailed analysis of the margin of the southwestern deposit that is covered by M^3 data, as indicated in Figure 5.5. This deposit exhibits both glass-rich areas and CPX/glass mixtures. The M^3 scene covering this portion of the crater is from a warmer operational period and thus exhibits markedly greater noise than the scenes covering the eastern portion of the crater. See Figure 5.11 caption for description of individual parts.

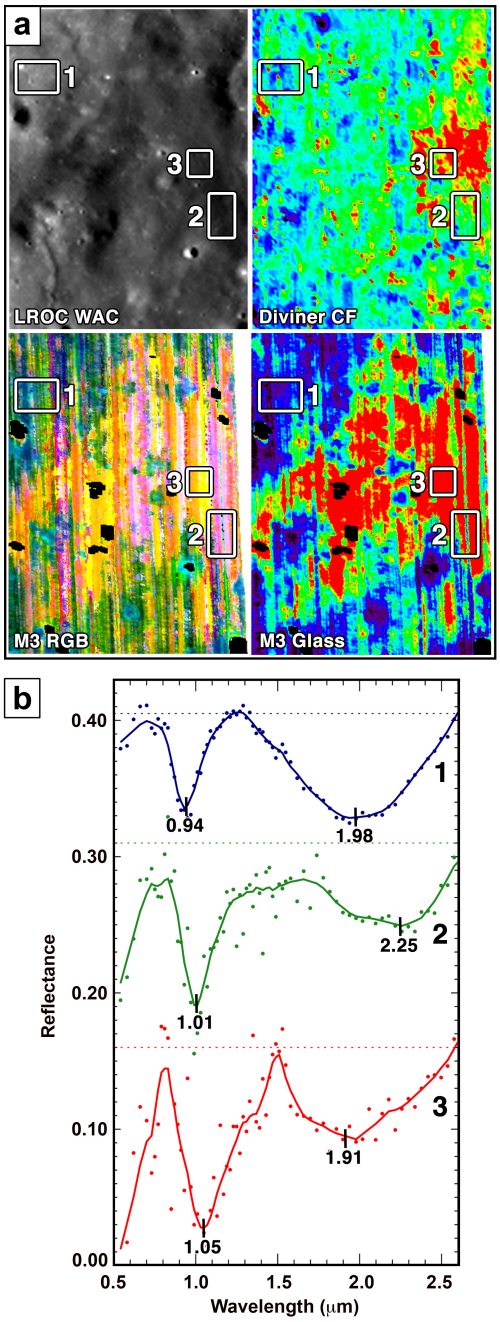

Figure 5.17 Detailed analysis of the margin of the northwestern deposit that is covered by M^3 data, as indicated in Figure 5.5. This deposit exhibits both glass-rich areas and CPX/glass mixtures. The M^3 scene covering this portion of the crater is from a warmer operational period and thus exhibits markedly greater noise than the scenes covering the eastern portion of the crater. See Figure 5.11 caption for description of individual parts.

5.5.3 Synthesizing Diviner and M^3

Figure 5.9a shows a density plot comparing Diviner CF values and the M^3 glass band depth parameter. While there is significant spread in CF values at low glass band depths (8.1–8.4 μm), the range in values shrinks with increasing glass band depths. In particular, CF values at glass band depths greater than 3% are restricted to greater than 8.2 μm. This trend of increasing CF value for increasing glass band depth is generally true at the scale of individual deposits as well, as is best shown in Figure 5.9f for the northwest deposit. In this heterogeneous deposit, the glass-rich area that I sampled (Figure 5.17, spectrum 3) exhibits very high CF values (Figure 5.9f; glass band depth of ~0.10; CF value of ~8.40 μm). The CF values for the glassiest portions of each deposit are listed in Table 5.3. These results also show that the average CF values of each deposit are within the margin of error for the average CF values of the glass-rich portion of that deposit. Together, these observations suggest that the CF values tend to decrease away from the northwest deposit. The lowest CF values for the pyroclastics are observed in the glass-rich east deposit, where the CF values for the nearby crater floor and the glass-rich terrain are nearly identical. This implies that CF values are not strictly correlated with the glass content of a deposit, and thus are controlled by other factors.

Table 5.3 Average CF Values and derived FeO wt. % for just the glassiest materials in each deposit. Glass is defined as having a 1 μm band center > 1.0, 1 μm band depth > 5%, a 2 μm band center < 2.07, and elevated glass band depths, which are restricted to the highest available values in each deposit to isolate the glassiest materials. NW/SW deposits are only sampled in the more distal portions of the deposit that are covered by M^3.

Deposit	Average CF Value of Glass-rich Pyroclastic Materials	Standard Deviation	FeO wt. % of Glass-rich Pyroclastic Materials	Standard Deviation	Glass Band Depth range
NW	8.32	0.07	18	5	0.08-0.14
SW	8.27	0.04	14	3	0.05-0.08
S	8.28	0.05	15	4	0.07-0.09
SSE	8.28	0.07	15	5	0.05-0.08
SE	8.25	0.03	13	2	0.04-0.08
E	8.24	0.03	12	2	0.04-0.06
N	8.29	0.11	16	8	0.05-0.09

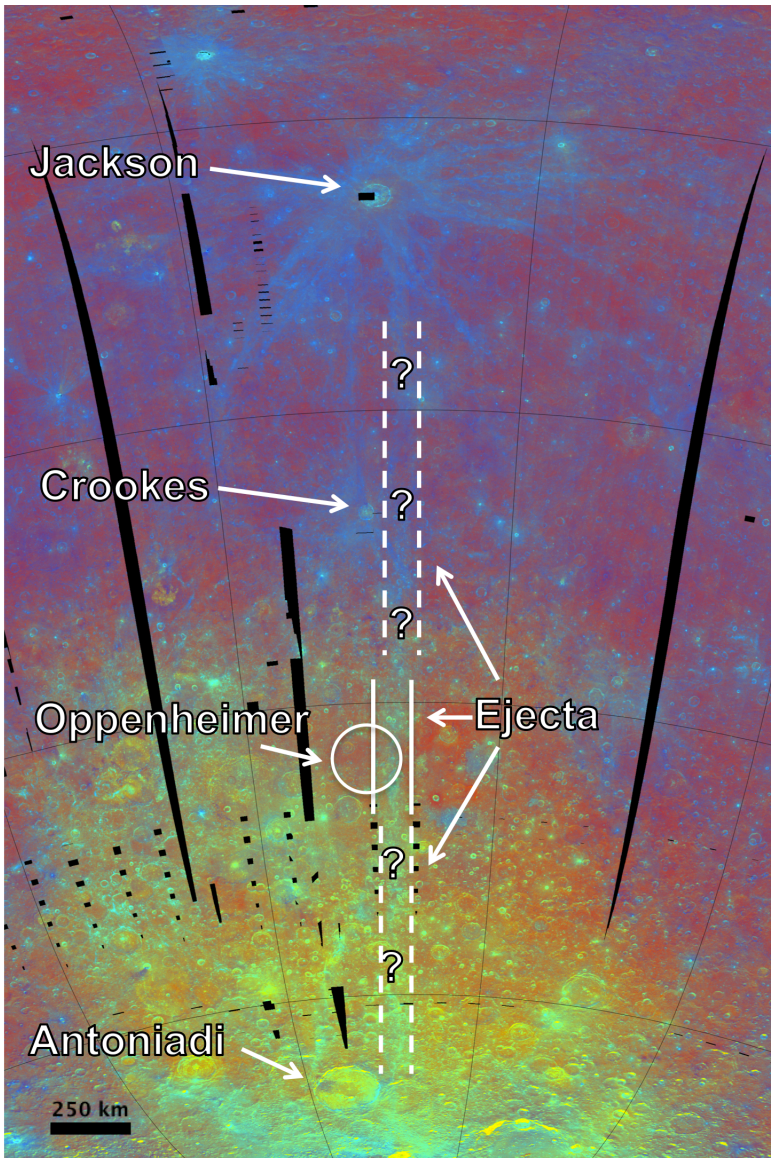

Figure 5.18 Clementine color ratio map for the far side of the Moon (McEwen, 1997), showing the east central region of the South Pole-Aitken basin. Red is 750/415 nm, green is 750/950 nm, blue is 415/750 nm. A lighter, ~linear feature is superimposed on the eastern portion of Oppenheimer crater, and this feature may be a crater ray. The thin black latitude and longitude lines are placed every 30°. Nearby craters include Jackson (located at 22.4° N, 163.1° W) and Antoniadi (located at 69.7° S and 172.0° W).

5.6 Discussion

5.6.1 Crater ray

Petro *et al.* (2001) noted that there is a high albedo crater ray mantling the eastern half of Oppenheimer crater. This ray is apparent in several of the datasets, including the CF map (Figure 5.4b) and Clementine color ratio (Figure 5.4d). Because crater rays can contain both distal ejecta and local ejecta from secondary craters (*e.g.*, Hawke *et al.*, 2004 and Dundas and McEwen, 2007), it is important to know whether the ray was emplaced before or after the pyroclastic deposits. If the ray was emplaced afterwards, I must account for this in my interpretations. Figure 5.18 shows a Clementine color ratio map of part of the far side of the Moon. Oppenheimer is circled and the ray crossing Oppenheimer is outlined. There are several craters that this ray may have originated from, including Jackson, Crookes, and Antoniadi. Jackson (22.4°N, 163.1°W) and Crookes (10.3°S, 164.5°W) craters are both Copernican aged and have visible rays (Wilhelms, 1987). Antoniadi crater (69.7°S, 172.0°W) is late Imbrium aged, and therefore I do not expect to see preserved rays (Wilhelms, 1987). However, there do appear to be a few rays extending from Antoniadi. It is possible that these rays are from a younger impact crater and they happen to cross Antoniadi. The rays from Jackson, Crookes, and near Antoniadi all are in line with the ray that mantles Oppenheimer crater, butIcannot determine which of these craters (if any) the ray over Oppenheimer was sourced from. However, craters that have bright, extensive rays are thought to be Copernican aged (such as Jackson and Crookes craters), while most lunar volcanism is thought to have stopped ~2 billion years ago (Hiesinger *et al.*, 2000). Therefore I can

safely assume that the ray postdates the pyroclastic deposits in eastern Oppenheimer crater. I will examine this possibility while interpreting my data.

5.6.2 Crater floor

M^3 results showed that the ejecta covered crater floor exhibits band centers between 0.90–0.98 and 1.99–2.06 μm, consistent with an OPX/CPX mixture, but that the western (ray-free) half of the crater floor plus fracture walls and fresh craters on the crater floor have band centers shifted slightly lower. Together, these observations suggest that the actual crater floor is primarily OPX mixed with minor CPX. An OPX-rich composition of the floor of Oppenheimer crater is consistent with the general iron enhancement observed throughout the basin, likely due to the existence of OPX-bearing materials (*e.g.*, norite) across the South Pole–Aitken basin interior (Ohtake *et al.*, 2014). Both the western crater floor (8.24 μm) and the eastern crater floor (8.20 μm) have a CF value that is consistent with pyroxene, which is consistent with the M^3 results. I hypothesize that the difference in CF value between the western and eastern crater floors is due to the large ray across the eastern half of the crater. Crater rays contain large numbers of secondary craters, which can churn up fresh material (Hawke *et al.*, 2004 and Dundas and McEwen, 2007). Since I observe a difference between the ray-covered east crater floor and ray-free west crater floor (8.20 μm and 8.24 μm, respectively), this could mean one of two things. One possibility is that the ray covered eastern half of the crater is more immature than the western half. Diviner CF is affected by maturity, so it is possible that the only difference between the two crater halves is how much space weathering has occurred, consistent with recent exposure of lower CF

material inside of the crater ray in the eastern half. Another possibility is that the western crater floor is mantled by a material that is slightly more iron-rich than the OPX-rich crater floor. In this scenario, the entire crater floor could have been mantled by a thin layer of iron-rich material and this thin layer was overturned and mixed with crater floor material when the east half of the crater was impacted by the ejecta in the ray. The thin mantling layer could be pyroclastic material, as there are glass signatures on both the western and central-eastern crater floor in the M^3 mineral maps that could represent a small amount of pyroclastic glass.

5.6.3 Pyroclastic deposits

5.6.3.1 Thermal inertia

Previous studies have shown that regional pyroclastic deposits exhibit lower nighttime temperatures than the lunar regolith, which implies that they have a lower thermal inertia and are likely finer-grained than typical lunar regolith (*e.g.,* Bandfield *et al.,* 2011). My results (Figure 5.4c; Table 5.1) are not consistent with those previous studies. The largest variation in thermal inertia is between the western half of the crater floor and the eastern half, which is covered by a large crater ray. The many secondary craters associated with the ray across the eastern half of the crater likely raises the thermal inertia of these areas. The pyroclastic deposits exhibit the same thermal inertia as the surrounding crater floor. The south, southwest, and northwest deposits are located on the western half of the crater and all have an *H*-parameter value of ~0.1, which is similar to the western crater floor and typical of mature highlands regolith. The east, southeast,

and south–southeast deposits are located within the boundaries of the ray and they have an *H*-parameter value of 0.08, which is the same as the eastern crater floor.

That the eastern pyroclastic deposits exhibit similar thermal inertia as the surrounding area is unsurprising since impact craters and rays greatly influence the thermal inertia of the lunar surface. The eastern pyroclastic deposits and crater floor are both covered with small secondary craters inside of the ray and this likely caused both areas to exhibit similar thermal inertia values. However, the western pyroclastic deposits that are not affected by the ray also exhibit similar thermal inertia as the surrounding area. This implies that the physical characteristics of the pyroclastic deposits within Oppenheimer crater are not necessarily similar to the regional deposits that contain fine-grained, spherical beads and exhibit low thermal inertia values.

There are several possible explanations for these results. A deposit emplaced by a Vulcanian-style eruption will contain blocks and ash, which would raise its thermal inertia. If an eruption began with a Vulcanian-style eruption and then finished with fire fountaining activity, the blocky, high thermal inertia material from the Vulcanian eruption could cancel out the effects of the fine-grained, low thermal inertia material from the fire fountaining activity. However, this scenario is likely to coincidental to be a reasonable solution. An alternate explanation is that if a deposit was emplaced by a Hawaiian-style eruption in which individual pyroclasts were still warm when they were deposited, the pyroclasts would have been welded together. These welded pyroclasts would have the effect of raising the thermal inertia of a deposit. A final explanation is localized deposits are small enough that over time impact gardening homogenized each deposit so that it has the same thermal properties as the surrounding regolith. The impact

gardening must not affect the mineralogy of the deposits, as clear differences in mineralogy are observed between the pyroclastic deposits and the crater floor.

5.6.3.2 Composition

The CF values of the pyroclastic deposits (8.25–8.48 μm) range from being consistent with pyroxene to olivine or iron-rich glass. The average CF value may correlate with the size of the deposit, with the larger deposits (south, southwest, and northwest) exhibiting higher CF values and the smaller deposits (north, east, southeast, south–southeast) exhibiting lower CF values. However, this could also be due to the low CF crater ray covering the eastern half of the crater and mixing with the pyroclastic material to lower the deposits' CF value. The Clementine color ratio image (Figure 5.4d) shows the extent of the crater ray. The ray covers the east, southeast and south–southeast deposits, but it does not extend to the north deposit. The north deposit has a slightly higher CF value than the east, southeast, and south–southeast deposits (8.27 μm *vs*. 8.24–8.25 μm). This implies that the east, southeast, and south–southeast deposits could be mixed with fresh material that lowers each deposit's CF value. However, the difference in CF values between the north deposit and the east, southeast, and south–southeast deposits is within the standard deviation of the measurements (±0.03–0.04 μm), so the variation between these deposits could also be due to noise. The larger deposits (south, southwest, and northwest) have CF values that range from 8.29 to 8.36 μm, although small areas within each deposit exhibit CF values as high as 8.48 μm. I interpret these values to represent an iron-rich glass, as olivine is not supported by my M^3 analyses. Most of the smaller deposits (east, southeast, and south–southeast) are homogeneous and do not

exhibit areas of enhanced CF values. However the north deposit shows higher CF values in the center of the deposit and lower CF values towards the edges, which suggests a radial mixing of crater floor material with pyroclastic material.

Table 5.1 also shows the estimated iron abundance of each deposit. The high CF areas within the larger deposits have estimated iron abundances of up to 30 wt%. The relationship between iron abundance and CF values was calculated using Apollo samples, and in that study the sample with the highest iron abundance was Taurus Littrow (22.7 FeO wt%; Allen *et al.*, 2012). Therefore, the nature of the relationship between iron abundance and CF value can only be extrapolated linearly above 22.7 FeO wt%. The pyroclastic glass beads from the Apollo samples have FeO contents that range from 16.5 to 24.7 wt% (Delano *et al.*, 1986). If the linear extrapolation above 22.7 FeO wt% is an accurate representation of the iron and CF correlation, the northwest and south deposits both have areas of enhanced FeO content that contain more FeO than any other previously known lunar pyroclastic glass (~30 wt% and ~26 wt%, respectively). The M^3 data support the presence of glass in these deposits (Figure 5.5), and therefore these deposits may contain the most iron-rich pyroclastic glass thus far identified on the Moon. SPA shows an iron-enhancement across the basin (Ohtake *et al.*, 2014). It is possible that Oppenheimer crater's location within the iron-rich SPA basin contributed to the high iron abundances in the pyroclastic deposits. It is also possible that the thin crust in SPA basin (~20 km as opposed to 30–50 km thick for the rest of the Moon; Wieczorek *et al.*, 2013) meant magma sourced from the mantle spent a shorter amount of time rising through the

crust and therefore had less time to accumulate less iron-rich country rock or evolve and preferentially crystallize iron-rich olivine out of the melt.

5.6.3.3 Classification of pyroclastic deposits based on mineralogy

Previous studies have generally studied pyroclastic deposits based on their average spectral character (*e.g.* Hawke *et al.*, 1989, Gaddis *et al.*, 2003 and Jawin *et al.*, 2015). A particular strength of this study is that I use spectral parameter maps to determine compositional and mineralogical variations at the sub-deposit level. Using these mapping techniques, I demonstrate that the mineralogy varies between and within pyroclastic deposits in Oppenheimer crater. My results directly address the Lunar Roadmap goal of "map the extent and composition of lunar pyroclastic deposits, including their associated crystalline components" (LEAG, 2011). These mapping results show that the pyroclastic deposits within Oppenheimer crater can be divided into three groups based on their mineralogy: small glass-rich deposits, small to medium deposits that are mixtures of CPX and glass, and large deposits with complex mineralogy. Furthermore, these mineralogical groups appear to correlate with the location of the deposits within Oppenheimer crater.

In the northeastern portion of Oppenheimer crater, the small north and east deposits are both glass-rich. The north deposit exhibits the second highest glass band depths between 5% and 9%, while the east deposit exhibits the purest glass signatures (the bulk of the deposit does not appear to be significantly mixed with other minerals). Indeed, the very high 1 μm band centers in the east deposit (1.09–1.13 μm) are consistent with lab spectra of mixtures containing more than 70–80 wt% glass (Horgan *et al.*, 2014).

These deposits have CF values that lie roughly in the middle of all pyroclastic deposits, 8.27 and 8.26 μm, respectively. The mineralogy of the east deposit is shown in detail in Figure 5.11. The center of this deposit is glass-rich, but the edge is a mixture of glass and crater floor material, OPX and minor CPX. While this deposit shows evidence of crater floor material mixing with juvenile material, this does not necessarily imply that it is a result of Vulcanian activity. In Vulcanian deposits, the country rock is typically mixed in with the entire deposit. Jawin *et al.* (2015) used M^3 data to show that some pyroclastic deposits get thinner toward the edge of the deposit and the underlying material begins to contribute to the spectral signature. Therefore it is likely that the surface material in the east deposit is entirely juvenile glassy material, and the OPX/CPX signature at the edge of the deposit is the crater floor being revealed in patches or rough terrain exposed in the thin deposit.

In the southeastern portion of Oppenheimer crater, the southeast and south–southeast deposits are mixtures of CPX and glass. These deposits have the lowest CF value of all the Oppenheimer pyroclastic deposits: both are 8.25 μm. Figure 5.12 shows the detailed mineralogy and Figure 5.13 shows the morphology of the southeast deposit. I observe evidence of multiple eruption centers in the southeast deposit. Figure 5.13 shows two locations within the deposit that appear to be small, distinct deposits of low albedo mantling material. Thus, the southeast deposit could consist of many small eruptions that make up the larger deposit. This could explain the deposit's irregular shape, as well as some of the many vent-like craters found within the deposit.

In the western half of Oppenheimer crater, the south, southwest, and northwest deposits are all heterogeneous in composition. The south deposit contains OPX, CPX and

glass, but there are sections of the deposit that are glass-rich and sections that are CPX/glass mixtures. The southwest and northwest deposits contain both CPX and glass. These three deposits exhibit the highest CF values in Oppenheimer crater, 8.28, 8.31, and 8.33 μm. While there is striping due to noise within the south deposit, there do appear to be real spectral variations between the main lobe and the eastern lobe of the deposit. These spectral variations within the deposit correspond to differences in morphology. Figure 5.15 shows LROC visible images of the S deposit. The NAC image in Figure 5.15b shows a glass-rich area of the deposit and the NAC image in Figure 5.15c shows a CPX/glass mixture. The glass-rich area is in the center of the deposit, is smooth and flat, and does not have many large craters. In contrast, the area that is a mixture of CPX and glass is at the eastern edge of the deposit, the pyroclastic material mantles the local topography, and is associated with a crater, possibly a vent, along the fracture. Therefore, it is likely that there are at least two eruptive centers within this deposit.

5.6.4 Inferred eruption styles

In this section I discuss how the mineralogy of the pyroclastic deposits in Oppenheimer crater compares to the deposits drawn in Figure 5.2 and how this constrains the eruption styles that likely occurred to emplace each deposit.

The first category of pyroclastic deposits (north and east deposits) in Oppenheimer crater is small and glass-rich. I hypothesize that glass-rich areas represent pyroclastic glass beads. There is no sign of mixing with plug material in these deposits, which implies that the last stage of an eruption at these vents was a fire fountaining event.

If there was an initial Vulcanian eruption, the glass-rich deposit completely obscures it in both deposits.

The second category of pyroclastic deposits (southeast and south–southeast) is mixtures of CPX and glass. I hypothesize that the CPX in these pyroclastic deposits is likely crystalline juvenile material. The CPX could be sourced from the ejection of a solidified plug in a Vulcanian eruption. Alternatively, crystalline juvenile material could be emplaced if molten magma is erupted and given enough time to crystallize instead of immediately quenching and becoming glass. For example, during a high mass-eruption rate fire-fountain event in which the eruptive column is optically thick, magma droplets could crystallize (Head and Wilson, 1989). Lastly, if the eruption is a fire fountaining or Strombolian event, large blebs of molten magma can accumulate near the vent and begin to form a lava flow and crystallize. Lava flows have not been directly identified associated with these pyroclastic deposits, but in the CPX-rich southeast deposit I have identified several bench craters (Figure 5.13d and e). Bench craters are associated with an impact into layered terrain where less coherent materials overlie more coherent materials, such as a regolith covered mare (Oberbeck and Quaide, 1967 and Quaide and Oberbeck, 1968). In the southeast deposit, bench craters might indicate that there was an impact into unconsolidated pyroclastic material or regolith overlying a lava flow. Indeed, Jozwiak *et al.* (2015) suggested that a lava flow could have occurred in the crater associated with the southeast deposit based on their model of floor-fractured craters. Alternatively, the bench crater could have resulted from an impact into unconsolidated pyroclastic material that overlies a more coherent crater floor material. Thus, CPX in the southeast deposit could either be plug material from multiple cycles of Vulcanian eruptions, crystalline

juvenile material from less energetic fire-fountain eruptions, or from lava flows. Therefore, the eruption style of these deposits is less well constrained.

The third category of pyroclastic deposits (south, southwest, and northwest) is heterogeneous deposits. Since the composition varies throughout the deposit, it is likely that multiple eruptions created these deposits. The south deposit shows variation along the fracture, with fire fountaining likely depositing the bulk of the smooth, glass-rich pyroclastic material and Vulcanian activity depositing the smaller area that is a mixture of CPX and glassy material.

The component that is conspicuously lacking from the Oppenheimer pyroclastic deposits is country rock, or crater floor material, which is OPX-rich. As shown in Figure 5.2, the presence of country rock implies there was Vulcanian activity. However, I only see OPX in one pyroclastic deposit, the south deposit, and it is likely that the OPX signatures are coming from the vent wall. Indeed, some of the strongest OPX signatures I observe are exposed in the wall of a portion of the source fracture. The lack of country rock within pyroclastic deposits in Oppenheimer crater suggests that these deposits were not emplaced by simple Vulcanian eruptions. It is still possible that there is plug material in the deposits which would support Vulcanian activity, but the lack of country rock most likely indicates that there were fire fountaining events that covered the country rock.
In summary, glass-rich deposits contain high abundances of pyroclastic glass beads, most likely emplaced in fire fountaining or Strombolian-type eruptions. CPX-rich deposits could either contain plug material from multiple cycles of Vulcanian eruptions, crystallized juvenile material from fire fountaining, or lava flows. Lastly, OPX signatures would indicate country rock/crater floor material emplaced during a classical Vulcanian

eruption, but the fact that I observe very little OPX within the pyroclastic deposits suggests that they were emplaced by other types of eruptions.

5.6.5 Implication for magmatic activity

Vulcanian activity within a floor-fractured crater has been described in detail earlier (Head and Wilson, 1979 and Head *et al.*, 2000), but the occurrence of Vulcanian activity in association with both fire fountaining and Strombolian activity has not previously been postulated to explain glass-rich pyroclastic deposits in such a setting. This combination of eruption styles may imply variability in magma ascent rates. It has been assumed that magma ascending from sills under floor-fractured craters is rising slowly, so that the mass eruption rate is low (Head and Wilson, 1979). In a Vulcanian eruption, this leads to a cooled plug and a slow buildup of pressure beneath it. In this scenario, after the initial violent explosion the eruption would cease quickly once the overpressure is released. However, since I observe large amounts of glass-rich juvenile material, some eruption of juvenile magmatic material must have occurred. If the source magma volume was sufficiently large, the eruption mechanism could start with an initial Vulcanian eruption and then shift to a fire fountaining event. Such a shift and the initial eruption could be triggered by an increase in magma ascent rate after initial plug formation.

Alternatively, the slow magma ascent rates assumed to be implied by the presence of a sill could still lead to a glass-rich deposit. If a plug does not form and magma ascends slowly to reach the surface, this could conceivably lead to relatively low mass eruption rate Strombolian activity rather than higher mass eruption rate fire fountaining.

Pyroclastic glass beads in Strombolian activity are thought to be formed when bubbles within the conduit reach the surface and infinitely expand in the atmosphere-less environment, disrupting the thin surface layer of magma caught above the bubble into pyroclasts and ejecting them away from the vent (Wilson and Head, 1981). However, if these models are underestimating sill emplacement or recharge rates and the mass eruption rate of the volcanic activity within Oppenheimer crater was high, perhaps due to the thin crust at SPA, then fire fountaining could have occurred instead.

These data suggest that multiple styles of eruption, specifically both Vulcanian and fire fountaining or Strombolian activity, may have occurred within Oppenheimer crater to form the observed pyroclastic deposits. In some cases (*e.g.,* the north and east deposits) where there is a single central vent, crater floor material mixed into the deposit, and abundant glass produced by fire fountaining or Strombolian activity could have followed an initial Vulcanian eruption at the same vent. The built-up pressure from trapped gas within a sill under Oppenheimer crater could have caused the initial Vulcanian explosion and created a path to the surface for the magma. Once a pathway existed, fire fountaining or Stombolian activity would have commenced if there were enough magma still ascending through the fractures.

The possibility of multiple styles of pyroclastic eruptions may have been enhanced by the location of Oppenheimer crater within the relatively thin crust (~20 km; Wieczorek *et al.,*2013) of the SPA basin because of increased access to magma sources beneath the fractured crust (*e.g.*, Soderblom *et al.,* 2015). This could have allowed fire fountaining or Strombolian activity to occur for longer periods of time as the magma was being replenished. This scenario would have resulted in larger, more iron-

and glass-rich deposits in addition to the smaller Vulcanian deposits. New studies of lunar pyroclastic deposits in other geologic settings with these methods will be necessary to address these hypotheses further. Also, additional modeling work that incorporates these results is critical for understanding the ascent and eruption of magma on the Moon. This will be especially relevant at deposits like the north deposit, which has been shown to have a small cone surrounding the vent and is glass-rich. These are characteristics of a Hawaiian-style fire fountaining eruption, but the eruption occurred in a floor fractured crater setting and created a smaller deposit than has been modeled for lunar fire fountaining events. Future modeling efforts will be necessary to address the new questions raised in this study.

5.7 Conclusions

Our analysis of lunar pyroclastic deposits within Oppenheimer crater reveals a complex volcanic history and demonstrates the usefulness of combining mid and near infrared measurements. My results support the following conclusions:

1. By using mapping techniques to analyze mid- and near-infrared datasets, I was able to analyze localized pyroclastic deposits in more detail than previous studies. A major result of this study was that I identified variable mineralogy within and between pyroclastic deposits in Oppenheimer crater.

2. The pyroclastic deposits within Oppenheimer contain various ratios of pyroxene (CPX and/or OPX) to iron-rich glass. All the deposits contain glass; the east and northwest deposit are the most glass-rich. Many deposits also exhibit strong CPX signatures that may be crystalline juvenile products emplaced during the pyroclastic

eruptions. No olivine was identified within Oppenheimer crater, despite its location within the deep South Pole Aitkin basin.

3. The mineralogic variations between deposits result from a combination of pyroclastic Vulcanian activity (producing glass and CPX), fire fountaining or Strombolian activity (producing glass), and possible lava flows related to the latter category of eruptions (producing CPX).

4. Morphology from visible images and variable mineralogy within deposits imply that several of the deposits (south and southeast) are likely the result of multiple eruption centers.

5. The variability of eruption styles and composition inferred for these deposits suggests that the eruption mechanics of local pyroclastic eruptions and the magmatic histories of floor-fractured craters are more complicated than previously thought.

6. Oppenheimer crater's location within the SPA basin could have caused the high iron content of the deposits, and the thin crust could have enabled magma transport to the surface.

7. From a resource standpoint, the three largest pyroclastic deposits within Oppenheimer (northwest, southwest and south) would be good sites for future exploration. These deposits contain the most iron-rich volcanic glass thus far identified on the Moon (giving them a high potential to also contain significant abundances of oxygen), have large areas (the northwest deposit is large enough to be considered a regional deposit; < 1000 km^2), and are not covered in impact ejecta like the deposits on the eastern half of the crater.

CHAPTER 6

CONCLUSIONS

This thesis has made significant contributions to the fields of martian sedimentology and lunar volcanology. Chapters 2 and 3 contributed to the growing body of knowledge regarding widespread ancient sedimentary deposits on Mars and provided context for the Mars Science Laboratory investigations in Gale crater. Chapter 4 demonstrated that Mars is still geologically active (at least via aeolian transport) and that current aeolian processes are not straightforward. Chapter 5 showed that several small pyroclastic deposits on the Moon were a result of complex explosive volcanism and may require us to rethink our models of lunar volcanism. Overall, this work has demonstrated that using multiple datasets in tandem greatly increases their aggregated science return.

In Chapter 2, I showed that central mounds in large (> 25 km diameter) craters occur across Mars, but primarily in the cratered highlands with over 60% of mounds located in Arabia Terra. I proposed that central mounds are remnants of previously more extensive large-scale sedimentary deposits. With this constraint, I discussed the many potential formation mechanisms of central mounds and concluded that groundwater upwelling, explosive volcanism and ice-related processes were the most likely processes to contribute to mound growth. I would like to emphasize that all central mounds do not necessarily have the same formation mechanism. It is possible that all mounds formed from a global process, such as global ice ages, but it is more likely that clusters of mounds experienced similar formation mechanisms. Mars has a complex geologic history that varied across the globe, and central mounds likely reflect that.

I also showed that mounds are offset away from the center of their host crater. The mounds in Arabia Terra and near the north pole are offset to the western side of their host crater. These offsets correspond to the prevailing wind direction in those regions, which implies that wind is the primary eroding agent for the majority of central mounds. A more recently published study by Day *et al.* (2016) supports this hypothesis. They showed that models of a full crater being eroded by a unidirectional wind will become a central mound offset in the same direction as the wind.

Mt. Sharp in Gale crater is a complex central mound that may require a more complicated model of emplacement than the rest of the global population of mounds. It will be difficult to compare Mt. Sharp to other, simpler, central mounds. In addition, it is possible that some of the complex mineralogy and geology observed at Gale crater is a result of geologic processes (possibly a lake; *i.e*. Le Deit *et al.*, 2013) that occurred after the mound was emplaced. If this is the case, then it is not appropriate to compare the features observed in Gale crater to other central mounds.

This study on the global population of central mounds raised several more questions that I will continue to address. For example, this study showed that while there are several clusters of mounds, some mounds are not located near other mounds. This raises the question of whether these mounds should be included in these studies. I have conducted a preliminary morphology study of central mounds, which shows that while several of these isolated mounds technically meet our definition of a central mound, their morphology is extremely different than the rest of the population and therefore should not be included in the global study. This preliminary morphology study also supports that there are several groups or categories of mounds, and that these groups might have

different formation mechanisms. In the future, I plan to complete this morphology study to further characterize mounds and constrain their formation mechanisms.

In addition to future morphology studies, studies utilizing radar data, stratigraphic analysis, and near- and thermal- infrared spectra could each constrain potential formation mechanisms in unique ways. Preliminary studies on mounds using radar data have been limited, as some mounds don't exhibit any subsurface radar signals. However, radar at central mounds has not been extensively investigated, there could be data that would allow us to study the subsurface below a mound. In addition to subsurface stratigraphy, studies using visible data to understand mound stratigraphy can contribute to this study. As outlined in Kite *et al.* (2013) each geologic process deposits layers with specific inclines, and analyzing the dip of layers within multiple central mounds can constrain their deposition history. Finally, it will be useful to include near- and thermal-infrared datasets in central mound studies. At least one mound exhibits hydrated minerals (Mt. Sharp in Gale crater). Conducting a comprehensive study on the mineralogy and composition of central mounds can show whether the hydrated minerals at Gale crater are unique.

In Chapter 3 I investigated a single central mound, Mt. Sharp in Gale crater, and demonstrated that THEMIS-VIS data products are useful for the characterization of regional color and morphology as well as providing context and finding locations to investigate further with higher resolution multi-spectral datasets (such as HiRISE + CRISM). In contrast to CTX mosaics that primarily show albedo differences due to dust cover, such as wind tails, the THEMIS-VIS band 3 greyscale mosaic reveals more details about the morphology, including different textures, due to the images being acquired at

later local times. The combination of the higher resolution THEMIS-VIS band 3 greyscale mosaic with the thermophysical information from the THEMIS-IR DCS mosaics can reveal unique patterns and units.

THEMIS-VIS has the potential to be a quantitative multispectral dataset, but, as I outlined in Appendix B, I only used this data qualitatively because of the uncertainties linked to quantitatively comparing multiple images. Future studies on the variations between different THEMIS-VIS images may lead to lower uncertainties in the data, but presently analysis of features within one image is the best option.

My analysis of dune albedo variations in Chapter 4 emphasizes that Mars is still a complex and dynamic planet. The dust on most of the dune fields that I studied is removed by strong winds that saltate sand, but on some slow or immobile dunes the dust is removed by dust devils. Dust devil tracks were not observed on any mobile dunes in this study, whereas they were observed in almost every observation taken at the stationary dune field in a crater in Syrtis Major. I observed a possible threshold migration rate in this study. If a dune is migrating faster than this threshold value, it is likely being cleared of dust via saltation. If a dune is migrating slower than this threshold value, it is likely being cleared of dust via dust devils. In future work, I can examine the physics of saltation and dust devils to derive a theoretical explanation of this threshold migration rate.

In this chapter I also show that the CTX albedo of dunes should not be used as a proxy for migration rate. The minimum albedo of the studied dune fields does not correlate well with ripple migration rate. In the future, this result should be compared to studies using other visible albedo datasets. For example, preliminary work by Banks *et al.*

(2015) suggests that there is a correlation between HiRISE albedo and dune migration rates. If this result holds, research needs to be done to explain this difference. One possibility is that HiRISE images are taken at a slightly different wavelength than CTX images, and this could be enough to observe different albedo values at the same location. Alternatively, the HiRISE images could be taken during a different time period than the CTX images I used. To test these possibilities, I would need to conduct a similar study with HiRISE images and obtain the albedo value of many dune fields at different times of year.

My analysis of lunar pyroclastic deposits within Oppenheimer crater in Chapter 5 reveals a complex volcanic history and demonstrates the usefulness of combining thermal- and near-infrared measurements. By using mapping techniques to analyze both mid- and near-infrared datasets, I was able to analyze localized pyroclastic deposits in more detail than previous studies. Near-infrared data yields information about the mineralogy of a material, but may or may not not yield information on its glassy components. Thermal-infrared data constrains the bulk composition of a material (including glass). By combining these two datasets one can better illuminate the full story and implications of a study region.

In this chapter I showed that the pyroclastic deposits within Oppenheimer crater are extremely glass-rich and iron-rich. This implies that these deposits were emplaced via fire fountaining instead of Vulcanian activity, as expected for localized pyroclastic deposits within a floor-fractured crater. These results raise a larger question about localized deposits in general: are the deposits in Oppenheimer crater anomalies or are localized deposits in general more complex than previously realized? This question can

be addressed by analyzing additional pyroclastic deposits. I hypothesized that Oppenheimer crater's location within the thin-crusted South Pole Aitken basin could have allowed magma to reach the surface more easily and resulted in more iron-rich, glass-rich deposits. In a preliminary study, I compared the CF values in Oppenheimer to the CF value of the only other pyroclastic deposit located within the South Pole Aitken basin, the Schrodinger deposit. This deposit is extremely iron-poor; however, this deposit is extremely close to the south pole where the CF data becomes less reliable. These preliminary results may suggest that pyroclastic deposits are not iron-rich simply because they are located within the South Pole Aitken basin, but more work must be done to validate these results.

The other possible hypothesis is that localized deposits are not always a result of Vulcanian activity and instead there is a spectrum or transition between Vulcanian and fire fountaining eruptions. Recent studies that I was involved with support this hypothesis. Gaddis *et al.* (2016) investigated the pyroclastic deposits within Alphonsus crater using near-infrared data and found that they include abundant country rock and very little glass. Research by Keske *et al.* (2016) used LROC digital elevation models to estimate the volume of localized pyroclastic deposits compared to the volume of the vent. If the volume of the deposit is much greater than the volume of the vent, there must have been juvenile material emplaced. The results from Keske *et al.* (2016) correlate with the results from Chapter 5 and from Gaddis *et al.* (2016). The northern pyroclastic deposit in Oppenheimer crater that I showed contains abundant glass consists of ~90% juvenile material while a deposit in Alphonsus that Gaddis *et al.* (2016) showed contains country

rock contains only ~50% juvenile material. Together, these results suggest that localized deposits vary in eruption style and composition.

In this thesis I used a variety of remote sensing techniques and datasets to address questions in the fields of martian sedimentology and lunar volcanology. In the future, I will apply these techniques to other important questions in planetary science. I will also continue to build my skill set to work with additional and future datasets as well as gain skills in other techniques relevant to planetary science such as field work, laboratory studies, and/or modeling.

REFERENCES

Adams, J.B., 1974. Visible and near-infrared diffuse reflectance spectra of pyroxenes as applied to remote sensing of solid objects in the Solar System. J. Geophys. Res. 79, 4829–4836. doi:10.1029/JB079i032p04829.

Allen, C.C., Morris, R.V., McKay, D.S., 1996. Oxygen extraction from lunar soils and pyroclastic glass. J. Geophys. Res. 101 (E11), 26085–26095. doi:10.1029/ 96JE02726.

Allen, C.C., Greenhagen, B.T., Donaldson Hanna, K.L., *et al.*, 2012. Analysis of lunar pyroclastic deposit FeO abundances by LRO Diviner. J. Geophys. Res. 117, 1–12. doi:10.1029/2011JE003982, E00H28.

Anderson, R., Bell, J. F., III., 2010. Geologic mapping and characterization of Gale Crater and implications for its potential as a Mars Science Laboratory landing site. The Mars Journal, *5*, 76–128. doi:10.1555/mars.2010.0004

Andrews-Hanna, J. C., Phillips, R. J., Zuber, M. T., 2007. Meridiani Planum and the global hydrology of Mars. Nature, 446(7132), 163–166. http://doi.org/10.1038/nature05594

Andrews-Hanna, J. C., Zuber, M. T., Arvidson, R. E., Wiseman, S. M., 2010. Early Mars hydrology: Meridiani playa deposits and the sedimentary record of Arabia Terra. J. Geophys. Res. Planets, 115 (E06002). doi:10.1029/2009JE003485

Arndt, J., Engelhardt, W.V., Gonzalez-Cabeza, I., Meier, B., 1984. Formation of Apollo 15 green glass beads. In: Proceedings of the 15th Lunar and Planetary Science Conference, pp. C225–C232.

Arndt, J., Engelhardt, W., 1987. Formation of Apollo 17 orange and black glass beads. J. Geophys. Res. 92, E372–E376.

Ayoub, F., J.-P. Avouac, C. E. Newman, M. I. Richardson, A. Lucas, S. Leprince, N. T. Bridges, 2014. Threshold for sand mobility on Mars calibrated from seasonal variations of sand flux. Nat. Commun., 5, 5096, doi:10.1038/ncomms6096.

Bandfield, J.L., *et al.*, 2011. Lunar surface rock abundance and regolith fines temperatures derived from LRO Diviner Radiometer data. J. Geophys. Res. 116, 1–18. doi:10.1029/2011JE003866, E00H02.

Banks, M., Geissler, P., Bridges, N., *et al.*, 2015. Emerging global trends in aeolian bedform mobility on Mars. 4th International Planetary Dunes Workshop, 8036.

Bell III, J.F., M.C. Malin, B.A. Cantor, M.A. Caplinger, M.J. Wolff, *et al*., 2013 Calibration and Performance of the Mars Reconnaissance Orbiter Context Camera (CTX), Mars 8, 1-14, 2013, doi:10.1555/mars.2013.0001.

Bennett, K. A., Bell, J. F., III., 2016. A global survey of martian central mounds: Central mounds as remnants of previously more extensive large-scale sedimentary deposits. Icarus, 264, 331–341. http://doi.org/10.1016/j.icarus.2015.09.041

Besse, S.J., *et al.*, 2013. A visible and near-infrared photometric correction for Moon Mineralogy Mapper (M3). Icarus 222 (1), 229–242. doi:10.1016/j.icarus.2012.10. 036.

Boardman, J.W., *et al.*, 2011. Measuring moonlight: An overview of the spatial properties, lunar coverage, selenolocation, and related Level 1B products of the Moon Mineralogy Mapper. J. Geophys. Res. 116, 1–15. doi:10.1029/2010JE003730, E00G14.

Bradley, B. A., 2002. Medusae Fossae Formation: New perspectives from Mars Global Surveyor. J. Geophys. Res., *107*(E8), 5058. doi:10.1029/2001JE001537

Bridges, N. T., Bourke, M. C., Geissler, P. E., Banks, M. E., Colon, C., *et al.*, 2011. Planet-wide sand motion on Mars. Geology, 40(1), 31–34. http://doi.org/10.1130/G32373.1

Burns, J.O., Kring, D.A., Hopkins, J.B., *et al.*, 2013. A lunar L2-Farside exploration and science mission concept with the Orion Multi-Purpose Crew Vehicle and a teleoperated lander/rover. Adv. Space Res. 52 (2), 306–320. doi:10.1016/j.asr.2012.11. 016.

Cabrol, N. A., Grin, E. A., 1999. Distribution, classification, and ages of Martian impact crater lakes. Icarus, 142(1), 160–172.

Campbell, B.A., Hawke, B.R., Morgan, G.A., 2014. Improved discrimination of volcanic complexes, tectonic features, and regolith properties in Mare Serenitatis from Earth-based radar mapping. J. Geophys. Res.: Planets 119, 313–330. doi:10.1002/ (ISSN)2169-9100.

Cantor, B. A., K. M. Kanak, K. S. Edgett, 2006, Mars Orbiter Camera observations of Martian dust devils and their tracks (September 1997 to January 2006) and evaluation of theoretical vortex models, J. Geophys. Res., 111, E12002, doi:10.1029/2006JE002700.

Carr, M. H., Clow, G. D., 1981. Martian channels and valleys: Their characteristics, distribution, and age. Icarus, 48, 91-117, doi:10.1016/0019-1035(81)90156-1.

Carter, L.M., Campbell, B.A., Hawke, B.R., *et al.*, 2009. Radar remote sensing of pyroclastic deposits in the southern Mare Serenitatis and Mare Vaporum regions of the Moon. J. Geophys. Res. 114 (E11), 1–12. doi:10.1029/2009JE003406, E11004.

Chojnacki, M., J. R. Johnson, J. E. Moersch, L. K. Fenton, T. I. Michaels, and J. F. I. Bell, 2015. Persistent aeolian activity at Endeavour crater, Meridiani Planum, Mars; new observations from orbit and the surface, Icarus, doi:10.1016/j.icarus.2014.04.044.

Christensen P. R., 1988. Global Albedo Variations on Mars: Implications for Active Aeolian Transport, Deposition, and Erosion. J. Geophys. Res., vol. 93, 7611-7624.

Christensen, P. R., Bandfield, J. L., Hamilton, V. E., Ruff, S. W., Kieffer, *et al.*, 2001. Mars Global Surveyor Thermal Emission Spectrometer experiment: investigation description and surface science results. J. Geophys. Res. Planets (1991–2012), *106*(E10), 23823–23871.

Christensen, P. R., Jakosky, B. M., Kieffer, H. H., Malin, M. C., McSween, H. Y., Jr, *et al.*, 2004. The thermal emission imaging system (THEMIS) for the Mars 2001 Odyssey mission. Space Science Reviews, 110, 85–130.

Christensen, P.R., Engle, E., Anwar, S., Dickenshied, S., Noss, D., *et al.*, 2009. JMARS - A Planetary GIS. *AGU Fall Meeting*, Abstract #IN22A-06.

Clancy, R. T., B. J. Sandor, M. J. Wolff, P. R. Christensen, M. D. Smith, *et al.,* 2000. An intercomparison of ground-based millimeter, MGS TES, and Viking atmospheric temperature measurements: Seasonal and interannual variability of temperatures and dust loading in the global Mars atmosphere. J. Geophys. Res., 105(E4), 9553–9571, doi:10.1029/1999JE001089.

Clark, R., Roush, T., 1984. Reflectance spectroscopy: Quantitative analysis techniques for remote sensing applications. J. Geophys. Res. 89, 6329–6340.

Clark, R.N., Pieters, C.M., Green, R.O., *et al.*, 2011. Thermal removal from nearinfrared imaging spectroscopy data of the Moon. J. Geophys. Res. 116, 1–9. doi:10.1029/2010JE003751, E00G16.

Cloutis, E.A., Gaffey, M.J., 1991. Spectral-compositional variations in the constituent minerals of mafic and ultramafic assemblages and remote sensing implications. Earth Moon Planets 53, 11–53. doi:10.1007/BF00116217.

Conway, S. J. et al., 2012. Climate-driven deposition of water ice and the formation of mounds in craters in Mars' north polar region. Icarus, 220(1), 174–193. doi:10.1016/j.icarus.2012.04.021

Craddock, R. A., Maxwell, T.A., 1993. Geomorphic evolution of the Martian highlands through ancient fluvial processes, J. Geophys. Res., 98(E2), 3453–3468, doi:10.1029/92JE2508.

Day, M. D., Kocurek, G. A., Anderson, W., 2014. Aeolian Erosion of Filled Martian Craters. Lunar and Planetary Science Conference, Abstract #2296.

Day, M., Anderson, W., Kocurek, G., Mohrig, D., 2016. Carving intracrater layered deposits with wind on Mars, Geophys. Res. Lett., 43, 2473–2479, doi:10.1002/2016GL068011.

Delamere, W. A. *et al.*, 2010. Color imaging of Mars by the High Resolution Imaging Science Experiment (HiRISE). Icarus, 205(1), 38–52. doi:10.1016/j.icarus.2009.03.012

Delano, J.W., 1986. Pristine lunar glasses: Criteria, data, and implications. J. Geophys. Res. 16, D201–D213.

Dundas, C.M., McEwen, A.S., 2007. Rays and secondary craters of Tycho. Icarus 186 (1), 31–40. doi:10.1016/j.icarus.2006.08.011.

Edwards, C. S., Nowicki, K. J., Christensen, P. R., Hill, J., Gorelick, N., Murray, K., 2011. Mosaicking of global planetary image datasets: 1. Techniques and data processing for Thermal Emission Imaging System (THEMIS) multi-spectral data. J. Geophys. Res., 116(E10), E10008. http://doi.org/10.1029/2010JE003755

Farley, K. A. *et al.*, 2013. In Situ Radiometric and Exposure Age Dating of the Martian Surface. Science. doi:10.1126/science.1247166

Fenton, L. K., Richardson, M. I., 2001. Martian surface winds: Insensitivity to orbital changes and implications for aeolian processes. J. Geophys. Res., 106(E12), 32885–32–902.

Edgett, K.S., 1997. Aeolian Dunes as Evidence for Explosive Volcanism in the Tharsis Region of Mars, Icarus, Vol. 130, 96-114, doi:10.1006/icar.1997.5806.

Fergason, R. L., Christensen, P. R., 2008. Formation and erosion of layered materials: Geologic and dust cycle history of eastern Arabia Terra, Mars. J. Geophys. Res., 113(E12), E12001. doi:10.1029/2007JE002973

Fisher, J. A., M. I. Richardson, C. E. Newman, M. A. Szwast, C. Graf, *et al.*, 2005. A survey of Martian dust devil activity using Mars Global Surveyor Mars Orbiter Camera images, J. Geophys. Res., 110, E03004, doi:10.1029/2003JE002165.

Gaddis, L.R., Pieters, C.M., Ray Hawke, B., 1985. Remote sensing of lunar pyroclastic mantling deposits. Icarus 61 (3), 461–489.

Gaddis, L.R., Hawke, B.R., Robinson, M.S., *et al.*, 2000. Compositional analyses of small lunar pyroclastic deposits using Clementine multispectral data. J. Geophys. Res. 105 (E2), 4245–4262.

Gaddis, L.R., Staid, M.I., Tyburczy, J.A., *et al.*, 2003. Compositional analyses of lunar pyroclastic deposits. Icarus 161 (2), 262–280. doi:10.1016/S0019-1035(02) 00036-2.

Gaddis, L.R., Weller, L., Barret, J., *et al.*, 2013. "New" volcanic features in lunar floorfractured Oppenheimer crater. In: Proceedings of the 44th Lunar and Planetary Science Conference, p. 2262.

Gaddis, L. R., Horgan, B., McBride, M., Bennett, K., Stopar, J., *et al.*, 2016. Alphonsus crater: Compositional clues to eruption styles of lunar small volcanoes. In: Proceedings of the 47th Lunar and Planetary Science Conference, p. 2065.

Garvin, J. , 2000. North Polar Region Craterforms on Mars: Geometric Characteristics from the Mars Orbiter Laser Altimeter. Icarus, 144(2), 329–352. doi:10.1006/icar.1999.6298

Geissler, P. E., R. Sullivan, M. Golombek, J. R. Johnson, K. Herkenhoff, *et al.*, 2010. Gone with the wind: Eolian erasure of the Mars Rover tracks, J. Geophys. Res., 115, E00F11, doi:10.1029/2010JE003674.

Geissler, P. E., Fenton, L. K., Enga, M.-T., Mukherjee, P., 2016. Orbital monitoring of martian surface changes, in press at Icarus, doi:10.1016/j.icarus.2016.05.023.

Glotch, T.D., Lucey, P.G., Bandfield, J.L., *et al.*, 2010. Highly Silicic Compositions on the Moon. Science 329 (5998), 1510–1513. doi:10.1126/science.1192148.

Greeley, R., 2002. Saltation as a means for raising dust on Mars. Planetary and Space Science, 50(2), 151-155.

Greeley, R. *et al.*, 2003. Martian Dust Devils: Laboratory Simulations of Particle Threshold. J. Geophys. Res.*,* 108, no. E5, 5041. doi:10.1029/2002JE001987

Grotzinger, J. P., Sumner, D. Y., Kah, L. C., Stack, K., Gupta, S., *et al.*, 2014. A habitable fluvio-lacustrine environment at Yellowknife Bay, Gale Crater, Mars. Science. Vol 343. 1242777

Green, R.O., Pieters, C., Mouroulis, P., *et al.*, 2011. The Moon Mineralogy Mapper imaging spectrometer for lunar science: Instrument description, calibration, onorbit measurements, science data calibration and on-orbit validation. J. Geophys. Res. 116, 1–31. doi:10.1029/2011JE003797, E00G19.

Greenhagen, B.T., Lucey, P.G., Wyatt, M.B., *et al.*, 2010. Global silicate mineralogy of the Moon from the Diviner Lunar Radiometer. Science 329 (5998), 1507–1509. doi:10.1126/science.1192196.

Gustafson, J.O., Bell III, J.F., Gaddis, L.R., *et al.*, 2012. Characterization of previously unidentified lunar pyroclastic deposits using Lunar Reconnaissance Orbiter Camera data. J. Geophys. Res. 117 (E12), 1–21. doi:10.1029/2011JE003893, E00H25.

Hauri, E.H., Weinreich, T., Saal, A.E., *et al.*, 2011. High pre-eruptive water contents preserved in lunar melt inclusions. Science 333 (6039), 213–215. doi:10.1126/science.1204626.

Hauri, E.H., Saal, A.E., Rutherford, M.J., *et al.*, 2015. Water in the Moon's interior: Truth and consequences. Earth Planet. Sci. Lett. 409 (C), 252–264. doi:10.1016/j.epsl.2014.10.053.

Hawke, B.R., Coombs, C.R., Gaddis, L.R., *et al.*, 1989. Remote sensing and geologic studies of localized dark mantle deposits on the moon. In: Proceedings of the 20th Lunar and Planetary Science Conference, pp. 255–268.

Hawke, B.R., Coombs, C.R., Clark, B., 1990. Ilmenite-rich pyroclastic deposits: An ideal lunar resource. In: Proceedings of the 20th Lunar and Planetary Science Conference, pp. 249–258.

Hawke, B.R., Blewett, D.T., Lucey, P.G., *et al.*, 2004. The origin of lunar crater rays. Icarus 170 (1), 1–16. doi:10.1016/j.icarus.2004.02.013.

Head, J.W., 1974. Lunar dark-mantle deposits – Possible clues to the distribution of early mare deposits. In: Proceedings of the 5th Lunar and Planetary Science Conference, pp. 207–222.

Head III, J.W., Wilson, L., 1979. Alphonsus-type dark-halo craters – Morphology, morphometry and eruption conditions. In: Proceedings of the 5th Lunar and Planetary Science Conference, pp. 2861–2897.

Head, J.W., Wilson, L., 1989. Basaltic pyroclastic eruptions: influence of gas-release patterns and volume fluxes on fountain structure, and the formation of cinder cones, spatter cones, rootless flows, lava ponds and lava flows. J. Volcan. Geoth. Res. 37 (3), 261–271.

Head, J. W., Hiesinger, H., Ivanov, M. A., Kreslavsky, M. A. (1999). Possible ancient oceans on Mars: evidence from Mars Orbiter Laser Altimeter data. *Science*, 286, 2134-2137.

Head III, J.W., Wilson, L., Pieters, C.M., 2000. Pyroclastic eruptions associated with the floor-fractured lunar farside crater Oppenheimer in the South Pole Aitken Basin. In: Proceedings of the 31st Lunar and Planetary Science Conference, p. 1280.

Heiken, G.H., McKay, D.S., Brown, R.W., 1974. Lunar deposits of possible pyroclastic origin. Geochim. Cosmochim. Acta 38, 1703–1718.

Hicks, M.D., Buratti, B.J., Nettles, J., *et al.*, 2011. A photometric function for analysis of lunar images in the visual and infrared based on Moon Mineralogy Mapper observations. J. Geophys. Res. 116 (E12), E00G15. doi:10.1029/2010JE003733.

Hiesinger, H., Jaumann, R., Neukum, G., *et al.*, 2000. Ages of mare basalts on the lunar nearside. J. Geophys. Res. 105 (E12), 29239–29275. doi:10.1029/ 2000JE001244.

Hiesinger, H., Van Der Bogert, C.H., Jolliff, B.L., *et al.*, 2012. Stratigraphy of the South Pole–Aitken Basin based on crater size-frequency distribution measurements. In: Proceedings of the GSA Annual Meeting, GSA #30953-212430.

Hobbs, S. W., Paull, D. J., Bourke, M. C., 2010. Aeolian processes and dune morphology in Gale Crater. Icarus, 210(1), 102–115. http://doi.org/10.1016/j.icarus.2010.06.006

Horgan, B.H.N., Cloutis, E.A., Mann, P., *et al.*, 2014. Near-infrared spectra of ferrous mineral mixtures and methods for their identification in planetary surface spectra. Icarus 234 (C), 132–154. doi:10.1016/j.icarus.2014.02.031.

Iverson, Greeley, R., Pollack, 1976. Windblown Dust on Earth, Mars and Venus. Journal of Atmospheric Sciences, 33, 2425-2429.

Jakosky, B. M., Phillips, R. J., 2001. Mars' volatile and climate history. Nature, 412, 237-244. doi:10.1038/35084184.

Jawin, E.R., Besse, S., Gaddis, L.R., *et al.*, 2015. Examining spectral variations in localized lunar dark mantle deposits. J. Geophys. Res.: Planets 120, 1310–1331. doi:10.1002/2014JE004759.

Jozwiak, L.M., Head, J.W., Wilson, L., 2015. Lunar floor-fractured craters as magmatic intrusions: Geometry, modes of emplacement, associated tectonic and volcanic features, and implications for gravity anomalies. Icarus 248 (C), 424–447. doi:10. 1016/j.icarus.2014.10.052.

Kerber, L., Head, J. W., Madeleine, J.-B., Forget, F., Wilson, L., 2012. The dispersal of pyroclasts from ancient explosive volcanoes on Mars: Implications for the friable layered deposits. Icarus, 219(1), 358–381. doi:10.1016/j.icarus.2012.03.016

Kerber, L., Michalski, J. R., Bleacher, J. E., Forget, F., 2013. Ash Sources in Arabia Terra? Implications for the Arabia Deposits. 44th Lunar and Planetary Science Conference, Abstract #2290.

Keske, A. L., Robinson, M. S., Bennett, K. A., 2016. The morphometry of lunar localized dark mantle deposits. In: Proceedings of the 47th Lunar and Planetary Science Conference, p. 3048.

Kite, E. S., Lewis, K. W., Lamb, M. P., Newman, C. E., Richardson, M. I., 2013. Growth and form of the mound in Gale Crater, Mars: Slope wind enhanced erosion and transport. Geology, *41*(5), 543–546. doi:10.1130/G33909.1

Klima, R.L., Dyar, D.M., Pieters, C.M., 2011. Near-Infrared spectra of clinopyroxenes: Effects of calcium content and crystal structure. Meteor. Planet. Sci. 46, 379– 395. doi:10.1111/j.1945-5100.2010.01158.

Kok, J.F., 2010. Difference in the Wind Speeds Required for Initiation versus Continuation of Sand Transport on Mars: Implications for Dunes and Dust Storms. Physical Review Letters. 104. 074502. doi: 10.1103/PhysRevLett.104.074502

Lane, M. D., Christensen, P. R., 2013. Determining olivine composition of basaltic dunes in Gale Crater, Mars, from orbit: Awaiting ground truth from Curiosity. Geophysical Research Letters, 40(14), 3517–3521. http://doi.org/10.1002/grl.50621

Le Deit, L., Hauber, E., Fueten, F., Pondrelli, M., Rossi, A. P., Jaumann, R., 2013. Sequence of infilling events in Gale Crater, Mars: Results from morphology, stratigraphy,

and mineralogy. J. Geophys. Res. Planets, 118(12), 2439–2473. doi:10.1002/2012JE004322

Lee, S. W., Clancy, R. T., 1990. The Effects of Atmospheric Dust on Observations of the Surface Albedo of Mars. Scientific Results of the NASA-Sponsored Study Project on Mars: Evolution of Volcanism, Techtonics, and Volatiles. LPI Technical Report 90-06. p. 195.

Lunar Exploration Analysis Group, 2011. The Lunar Exploration Roadmap: Exploring the Moon in the 21st Century: Themes, Goals, Objectives, Investigations, and Priorities. Lunar Exploration Analysis Group.

Malin, M. C., Edgett, K. S., 2000. Sedimentary Rocks of Early Mars. Science, *290*(5498), 1927–1937. doi:10.1126/science.290.5498.1927

Malin, M. C., Edgett, K. S., 2001. Mars global surveyor Mars orbiter camera: Interplanetary cruise through primary mission. J. Geophys. Res. Planets (1991–2012), 106(E10), 23429–23570.

Malin, M. C. *et al.*, 2007. Context Camera Investigation on board the Mars Reconnaissance Orbiter. J. Geophys. Res., 112(E5), E05S04. doi:10.1029/2006JE002808

Matsuyama, I., Nimmo, F., Mitrovica, J. X., 2007. Reorientation of planets with lithospheres: The effect of elastic energy. Icarus, 191(2), 401–412. doi:10.1016/j.icarus.2007.05.006

McConnochie, T. H., Bell, J. F., III, Savransky, D., Mehall, G., Caplinger, M., *et al.*, 2006. Calibration and in-flight performance of the Mars Odyssey Thermal Emission Imaging System visible imaging subsystem (THEMIS-VIS). J. Geophys. Res., 111(E6), E06018. http://doi.org/10.1029/2005JE002568

McEwen, A.S., Robinson, M.S., 1997. Mapping of the Moon by Clementine. Adv. Space Res. 19 (10), 1523–1533.

McEwen, A. S., Eliason, E. M., Bergstrom, J. W., Bridges, N. T., Hansen, C. J., Delamere, W. A., *et al.*, 2007. Mars reconnaissance orbiter's high resolution imaging science experiment (HiRISE). J. Geophys. Res. Planets (1991–2012), 112(E5).

McEwen, A., 2010. The High Resolution Imaging Science Experiment (HiRISE) during MRO's Primary Science Phase (PSP). Icarus, 205 (1) pp. 2-37. doi: 10.1016/j.icarus.2009.04.023

McSween, H. Y., Harvey, R. P., 1993. Outgassed Water on Mars: Constraints from Melt Inclusions in SNC Meteorites. Science. 259 (5103), 1890-1892. doi:10.1126/science.2595103.1890

Melosh, H. J., 1980. Tectonic patterns on a reoriented planet: Mars. Icarus, 44, 745-751.

Milliken, R. E., Grotzinger, J. P., Thomson, B. J., 2010. Paleoclimate of Mars as captured by the stratigraphic record in Gale Crater. Geophysical Research Letters, 37(4), L04201. doi:10.1029/2009GL041870

Moores, J. E. *et al.*, 2015, Observational evidence of a suppressed planetary boundary layer in northern Gale Crater, Mars as seen by the Navcam instrument onboard the Mars Science Laboratory rover, Icarus, 249, 129–142, doi:10.1016/j.icarus.2014.09.020.

Morris, E. C., 2007. Aureole Deposits of the Martian Volcano Olympus Mons. Journal of Geophysical Research. Vol. 87, No. B2, 1164-1178.

Murchie, S., Arvidson, R., Bedini, P., Beisser, K., Bibring, J. P., Bishop, J., *et al.*, 2007. Compact Reconnaissance Imaging Spectrometer for Mars (CRISM) on Mars Reconnaissance Orbiter (MRO). J. Geophys. Res., 112(E5), E05S03. http://doi.org/10.1029/2006JE002682

Murray, K. C., P. R. Christensen, G. L. Mehall., 2016. THEMIS Geometric Processing User's Guide, NASA, Planetary Data System, ODY-M-THM-5-VISGEO-V2.0.

Neukum, G., *et al.*, 2004. Recent and episodic volcanic and glacial activity on Mars revealed by the High Resolution Stereo Camera. Nature, *432*(7020), 971–979.

Nozette, S., 1995. The Clementine mission: Past, present, and future. Acta Astronautica 35 (Suppl. 1), S161–S169. doi:10.1016/0094-5765(94)00181-K.

Oberbeck, V.R., Quaide, W.L., 1967. Estimated thickness of a fragmental surface layer of Oceanus Procellarum. J. Geophys. Res 72 (18), 4697–4704.

Ohtake, M., Uemoto, K., Yokota, Y., *et al.*, 2014. Geologic structure generated by large-impact basin formation observed at the South Pole–Aitken basin on the Moon. Geophys. Res. Lett. 41 (8), 2738–2745. doi:10.1002/(ISSN)1944-8007.

Paige, D.A., Foote, M.C., Greenhagen, B.T., *et al.*, 2009. The Lunar Reconnaissance Orbiter Diviner Lunar Radiometer Experiment. Space Sci. Rev. 150 (1–4), 125– 160. doi:10.1007/s11214-009-9529-2.

Parker, T. J., Saunders, R. S., Schneeberger, D. M., 1989. Transitional morphology in west Deuteronilus Mensae, Mars: Implications for modification of the lowland/upland boundary. Icarus, 82, 111-145.

Pelkey, S. M., Jakosky, B. M., Christensen, P. R., 2004. Surficial properties in Gale Crater, Mars, from Mars Odyssey THEMIS data. Icarus, 167(2), 244–270. http://doi.org/10.1016/j.icarus.2003.09.013

Petro, N.E., Gaddis, L.R., Staid, M.I., 2001. Analysis of the Oppenheimer pyroclastic deposits using Clementine UVVIS data. LPSC 32 #1953.

Pieters, C.M., McCord, T.B., Charette, M.P., *et al.*, 1974. Lunar surface: Identification of the dark mantling material in the Apollo 17 soil samples. Science 183, 1191– 1194.

Pieters, C.M., Boardman, J., Buratti, B., *et al.*, 2009. The Moon mineralogy mapper (M3) on Chandrayaan-1. Curr. Sci 96 (4), 500–505.

Pike, R. J., 1980. Formation of complex impact craters: Evidence from Mars and other planets. Icarus, 43(1), 1–19.

Pollack, J. B., Haberle, R., Greeley, R., Iverson, J., 1976. Estimates of the Wind Speeds Required for Particle Motion on Mars. Icarus, 29, 395-417.

Quaide, W.L., Oberbeck, V.R., 1968. Thickness determinations of the lunar surface layer from lunar impact craters. J. Geophys. Res. 73 (16), 5247–5270.

Reiss, D., Hoekzema, N. M., Stenzel, O. J., 2014. Dust deflation by dust devils on Mars derived from optical depth measurements using the shadow method in HiRISE images. Planetary and Space Science, 93-94(C), 54–64. http://doi.org/10.1016/j.pss.2014.01.016

Rennó, N. O., Burkett, M. L., 1998. A simple thermodynamical theory for dust devils. Journal of the Atmospheric Sciences*,* 55, 3244-3252.

Robinson, M.S., Brylow, S.M., Tschimmel, M., *et al.*, 2010. Lunar Reconnaissance Orbiter Camera (LROC) instrument overview. Space Sci. Rev. 150 (1–4), 81–124.

Rossi, A. P., *et al.*, 2008. Large-scale spring deposits on Mars? J. Geophys. Res., 113(E8), E08016. doi:10.1029/2007JE003062

Ruff, S. W., P. R. Christensen, 2002 Bright and dark regions on Mars: Particle size and mineralogical characteristics based on Thermal Emission Spectrometer data, J. Geophys. Res., 107(E12), 5119, doi:10.1029/2001JE001580

Ryan, J. A., Lucich, R. D., 1983. Possible Dust Devils, Vortices on Mars. J. Geophys. Res., 88, no c15, pp 11,005-11,011.

Schultz, P.H., 1976. Floor-fractured lunar craters. Moon 15 (3–4), 241–273.

Shearer, C.K., Papike, J.J., 1993. Basaltic magmatism on the Moon: A perspective from volcanic picritic glass beads. Geochim. Cosmochim. Acta 57 (19), 4785– 4812. doi:10.1016/0016-7037(93)90200-G.

Silvestro, S., Fenton, L. K., Vaz, D. A., Bridges, N. T., Ori, G. G., 2010. Ripple migration and dune activity on Mars: Evidence for dynamic wind processes. Geophysical Research Letters, 37(20). http://doi.org/10.1029/2010GL044743

Silvestro, S., Vaz, D. A., Ewing, R. C., Rossi, A. P., Fenton, L. K., *et al.*, 2013. Pervasive aeolian activity along rover Curiosity's traverse in Gale Crater, Mars. Geology, 41(4), 483–486. http://doi.org/10.1130/G34162.1

Sinclair, P., 1969. General Characteristics of Dust Devils. Journal of Applied Meteorology. Vol 8, 32-45.

Smith, D. E., *et al.*, 2001. Mars Orbiter Laser Altimeter: Experiment summary after the first year of global mapping of Mars. J. Geophys. Res., 106(E10), 23689. doi:10.1029/2000JE001364

Smith, D.E., Zuber, M.T., Jackson, G.B., *et al.*, 2010. The Lunar Orbiter Laser Altimeter investigation on the Lunar Reconnaissance Orbiter Mission. Space Sci. Rev. 150 (1–4), 209–241. doi:10.1007/s11214-009-9512-y.

Soderblom, J.M., Evans, A.J., Johnson, B.C., *et al.*, 2015. The fractured Moon: Production and saturation of porosity in the lunar highlands from impact cratering. Geophys. Res. Lett. 42, 6939–6944.

Sullivan, R., *et al.*, 2008, Wind-driven particle mobility on Mars: Insights from Mars Exploration Rover observations at “El Dorado” and surroundings at Gusev Crater, J. Geophys. Res., 113, E06S07, doi:10.1029/2008JE003101.

Sunshine, J.M., Pieters, C.M., 1993. Estimating modal abundances from the spectra of natural and laboratory pyroxene mixtures using the modified Gaussian model. J. Geophys. Res. 98 (E5), 9075–9087.

Tanaka, K., 2000. Dust and Ice Deposition in the Martian Geologic Record. Icarus, 144(2), 254–266. doi:10.1006/icar.1999.6297

Tirsch, D. *et al.*, 2011. Dark aeolian sediments in Martian craters: Composition and sources. J. Geophys. Res., 116, E3. doi:10.1029/2009JE003562

Thomas P., Veverka, J., Lee, S., Bloom, A., 1981. Classification of Wind Streaks on Mars. Icarus. 45. 124-153.

Thomas, P., Weitz, C., 1989. Sand dune materials and polar layered deposits on Mars. Icarus. Vol 81 185-215.

Thomson, B. J., Bridges, N. T., Milliken, R., Baldridge, A., Hook, S. J., *et al.*, 2011. Constraints on the origin and evolution of the layered mound in Gale Crater, Mars using Mars Reconnaissance Orbiter data. Icarus, 214(2), 413–432. doi:10.1016/j.icarus.2011.05.002

Trang, D., Lucey, P.G., Gillis-Davis, J.J., *et al.*, 2013. Near-infrared optical constants of naturally occurring olivine and synthetic pyroxene as a function of mineral composition. J. Geophys. Res.: Planets 118, 708–732. doi:10.1002/jgre.20072.

Vasavada, A.R., Bandfield, J.L., Greenhagen, B.T., *et al.*, 2012. Lunar equatorial surface temperatures and regolith properties from the Diviner Lunar Radiometer Experiment. Journal of Geophysical Research 117, 1–12. doi:10.1029/2011JE003987, E00H18.

Verba, C. A., P. E. Geissler, T. N. Titus, D. Waller, 2010. Observations from the High Resolution Imaging Science Experiment (HiRISE): Martian dust devils in Gusev and Russell craters, J. Geophys. Res., 115, E09002, doi:10.1029/2009JE003498.

Wang, H., M. I. Richardson, 2015. The origin, evolution, and trajectory of large dust storms on Mars during Mars years 24-30 (1999-2011). Icarus, 251, 112–127, doi:10.1016/j.icarus.2013.10.033.

Watters, T. R., *et al.*, 2007. Radar Sounding of the Medusae Fossae Formation Mars: Equatorial Ice or Dry, Low-Density Deposits? Science, 318(5853), 1125–1128. doi:10.1126/science.1148112

Wieczorek, M.A., Neumann, G.A., Nimmo, F., *et al.*, 2013. The crust of the Moon as seen by GRAIL. Science 339, 671–675. doi:10.1126/science.1231530.

Wilhelms, D.E., 1987. The Geologic History of the Moon. United States Geological Survey Professional Paper 1348.

Williams, R., *et al.*, 2013. Martian Fluvial Conglomerates at Gale Crater. Science, 340(6136), 1068–1072.

Wilson, L., Head III, J.W., 1981. Ascent and eruption of basaltic magma on the Earth and Moon. J. Geophys. Res. 86 (B4), 2971–3001.

Wolff, M. J., R. T. Clancy, 2003. Constraints on the size of Martian aerosols from Thermal Emission Spectrometer observations, J. Geophys. Res., 108(E9, 5097), doi:10.1029/2003JE002057.

Zabrusky, K., Andrews-Hanna, J. C., Wiseman, S. M., 2012. Reconstructing the distribution and depositional history of the sedimentary deposits of Arabia Terra, Mars. Icarus, 220(2), 311–330. doi:10.1016/j.icarus.2012.05.007

Zimbelman, J. R., Scheidt, S. P., 2012. Hesperian Age for Western Medusae Fossae Formation, Mars. Science, 336(6089), 1683–1683. doi:10.1126/science.1221094

APPENDIX A

CENTRAL MOUND STATISTICS

Crater Latitude	Crater Longitude	Diameter (km)	Crater Name	Mound Area (km)	Mound Height (m)	Mound Offset (r)	Mound Offset (θ)
50.55	16.36	53	Micoud	344	951	0.13	109.82
24.43	217.83	28		66	715	0.29	215.91
23.73	12.34	35		332	657	0.18	293.96
21.84	352.07	164	Bequerel	941	1085	0.41	191.15
15.77	10.22	36		265	664	0.42	317.44
14.90	10.68	43		1055	726	0.32	205.61
14.45	15.32	31		307	341	0.33	341.12
14.07	14.66	39		794	759	0.21	221.92
13.73	11.64	42		533	973	0.31	263.07
13.55	20.98	36		650	800	0.04	353.91
12.77	14.59	26		129	259	0.24	225.37
11.59	15.44	28		118	594	0.12	223.23
10.98	15.63	37		458	815	0.32	359.19
10.84	23.50	168	Henry	6881	2040	0.28	262.92
9.41	7.13	26		295	575	0.11	265.73
8.94	141.28	50		309	1306	0.04	243.79
8.60	20.98	67		790	2659	0.16	245.53
8.01	352.92	59	Danielson	1795	1974	0.34	169.91
6.95	10.20	45		858	1502	0.19	339.38
6.66	11.86	73		2307	816	0.16	299.16
6.58	14.30	66	Capen	804	771	0.36	265.02
6.27	23.48	38		737	928	0.07	191.56
5.88	355.58	54	Vernal	1499	710	0.31	314.99
5.61	8.59	56		1263	1313	0.37	248.01
5.47	0.07	40		756	939	0.38	193.75
5.22	21.63	57		1274	1361	0.31	355.32
5.05	349.86	109	Crommelin	4122	2171	0.18	196.07
3.80	1.63	51		929	1225	0.59	206.68
3.65	24.82	35		762	1144	0.05	350.30
2.66	350.64	84	Firsoff	3060	1728	0.10	130.48
2.11	352.17	49		1054	687	0.04	105.32
1.58	26.66	90		1883	2317	0.23	274.76
0.16	195.56	89	Nicholson	1733	3918	0.14	245.60
-0.14	14.35	40		517	1208	0.28	156.18
-1.14	22.16	68		1224	960	0.52	260.76
-3.13	23.64	88		2709	1974	0.20	252.99
-4.27	222.30	31		178	698	0.04	329.07
-5.24	221.19	37		410	1036	0.14	248.95
-5.38	137.84	147	Gale	3602	5273	0.19	7.86
-13.60	119.64	42		275	1014	0.06	76.11
-35.33	325.77	30		351	1244	0.29	80.99
-38.12	210.91	79		1552	1860	0.47	93.73
-41.58	352.53	76		518	1397	0.04	217.43
-45.45	90.98	55		320	1110	0.07	214.94
-46.40	34.80	25		87	889	0.35	18.81
-48.97	312.15	25		132	755	0.16	21.00
-49.26	183.20	133	Very	3494	1024	0.23	97.05
-51.61	231.42	159		864	1091	0.10	285.59
-55.45	9.85	26		119	960	0.04	342.92
-58.02	86.46	73	Spallanzani	376	574	0.14	346.93

APPENDIX B

THEMIS-VIS ARTIFACTS AND ERRORS

Data products from the THEMIS-VIS instrument exhibit artifacts due to stray light from outside of the field of view that reaches the detector (McConnochie *et al.*, 2006). These artifacts are described in McConnochie *et al.* (2006). Here I give examples of these artifacts from the data used in this study. Figure B.1 shows a THEMIS-VIS band 3 mosaic of northwestern Gale crater and the area that the Curiosity rover is investigating. Figure B.2 shows seven THEMIS-VIS color images in this area. By looking at the same area in multiple images, it is easier to see what colors are instrument artifacts. These images have saturated pixels around their borders (primarily the right and left sides) which result in vibrant colors such as green, pink, white and yellow. In order to create the color mosaic over the Mars Science Laboratory (MSL) area in Chapter 3 (Figure 3.2) I removed all of these artifacts from the THEMIS-VIS images (V46072001, V47183002, V52340002; Figure B.2 c, e, j) before mosaicking the images together.

In addition to the instrument artifacts, there are other errors associated with this dataset. THEMIS-VIS has four usable bands which can be used to create four point spectra. I did not use any four point spectra in Chapter 3 because the variation in albedo between different images is large enough that drawing conclusions from the data is difficult. The error plotted for each spectra in this Appendix is the standard deviation of the average albedo measurement. Here I will describe the variations in the data that led me to not include them in Chapter 3. The first case I will show is a situation in which there are many images over the same area. The MSL landing site (Figure B.1) has been imaged consistently since Gale crater was selected. In each THEMIS-VIS color image shown in Figure B.2 I selected five regions of interest (roughly outlined in Figure B.1; lower mound, dune field, crater floor, fan, crater wall) and took the average albedo of

each. I did not use exactly the same areas in each image in an effort to avoid instrument artifacts. Figure B.2 also shows the four point spectra of each unit for each image. Figure B.3 shows the four point spectra of all the data, as well as the data grouped by unit.

The plots in Figure B.2 show that the four point spectra are generally consistent between the images. The dune unit has the lowest albedo and the fan unit has one of the highest albedos. These data products are trustworthy when comparing four point spectra within one image. However, Figure B.3 shows that the absolute albedo of each unit greatly varies between images. When all the data are plotted together, there is no difference between four of the units. The mound, crater floor, fan, and crater wall all exhibit similar ranges in albedo (between 0.40 and 0.47 in band 4). THEMIS-VIS cannot distinguish the small variations between these units in Gale crater. There are only two resolved units in this area: the low albedo dunes and the high albedo terrain.

Next I investigate the four point spectra of dunes within Gale crater. Figure B.3 shows that dunes in Gale crater have a distinct low albedo four point spectra and Figure B.4 shows that dunes vary from blue to purple in the THEMIS-VIS color mosaic. I investigate the four point spectra to determine whether there are differences in the spectra that correspond to differences in dune color.

The THEMIS-VIS R/G/B color mosaic is made with bands 4/2/1. Band 1 (the blue channel) does not vary much (see Figure B.3). Instead, bluer areas in the 4/2/1 mosaic likely have a low albedo in band 4 (the red channel) and it is predicted that the dunes with a lower band 4 albedo will be blue.

Figure B.4 shows the location of all the dunes used in this study and Figure B.5 shows the four point spectra of these dunes. The dunes that are visually purple in the

THEMIS-VIS color mosaic are plotted as purple lines and the dunes that are visually blue are plotted as blue lines. This plot shows that a dune field's THEMIS-VIS four point spectrum does not predict whether the dune will be purple or blue. All bands of purple and blue dunes exhibit the same albedo range. The hypothesis that the blue dunes should have a lower band 4 albedo is not true.

The color variation in the dunes could be related to band ratios, as opposed to absolute albedo. The THEMIS-VIS color mosaic was created by normalizing the images, whereas raw data was used (and no visual corrections like normalizing, stretching or removing streaks were applied) to derive the albedo values used for the four point spectra. I plotted different bands of the albedo of dunes against each other in Figure B.6 to identify trends. Dunes that are visually purple are plotted as circles in various shades of purple. Dunes that are visually blue are plotted as squares in various shades of blue. These plots illustrate that there are no quantitative trends that could distinguish purple dunes from blue dunes.

These results call into question the validity of the observation that there are purple dunes and blue dunes in Gale crater. If there is no resolvable spectral difference between purple dunes and blue dunes, why are some dunes purple and some dunes blue? The answer could lie in the mosaicking process. When the images are normalized, this could change how the color of an image is displayed. However, as noted in Chapter 3, the THEMIS-VIS color variations at the dunes match the variations in the THEMIS DCS mosaics. The most notable difference is between the Bagnold dunes (THEMIS-VIS color = blue; 8/7/5 THEMIS DCS=pink) and the western sand sea (THEMIS-VIS color = purple; 8/7/5 THEMIS DCS = gold).

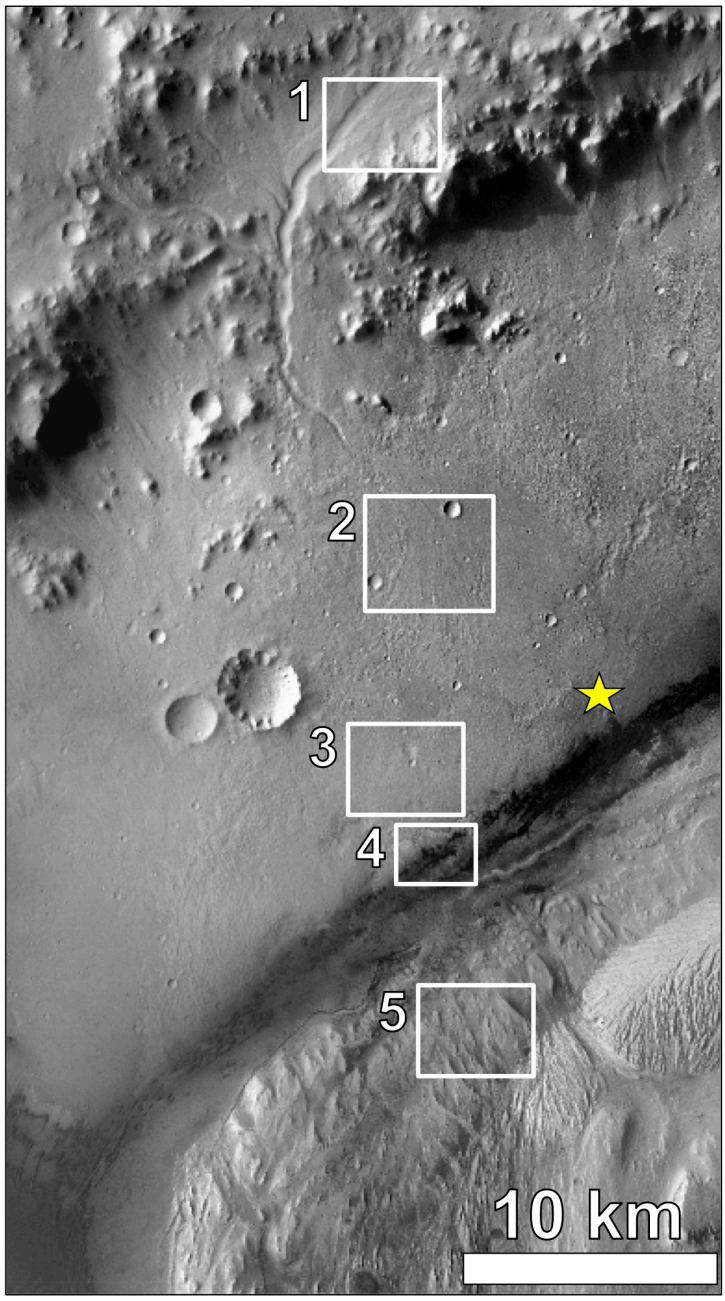

Figure B.1 THEMIS-VIS band 3 mosaic of Gale crater near the Curiosity rover. The white boxes show the locations of each unit sampled in Figure B.2: 1) crater wall, 2) fan, 3) crater floor, 4) dunes, 5) lower mound. The star represents the Curiosity rover's landing site.

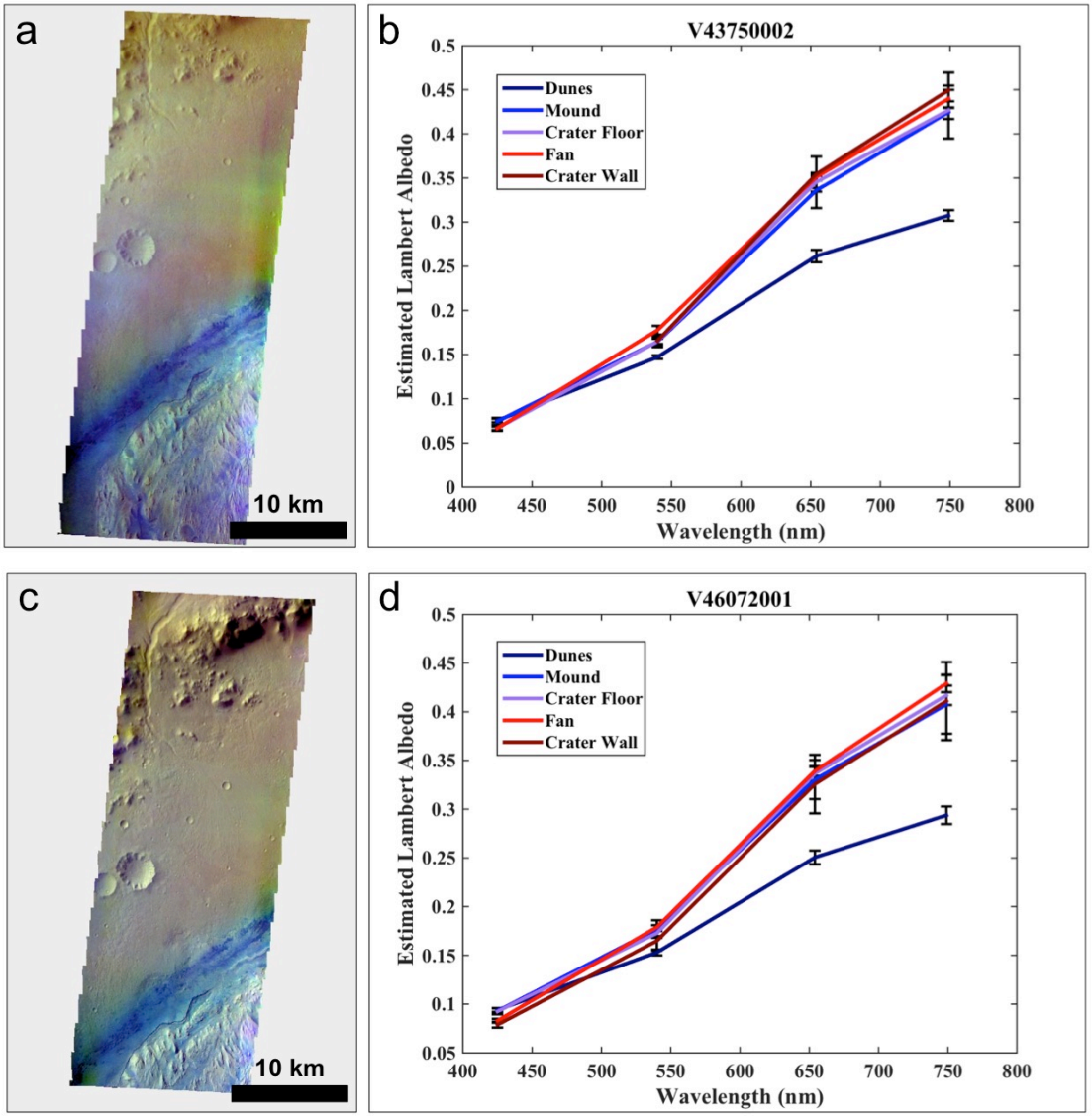
a
10 km
b
V43750002
Dunes
Mound
Crater Floor
Fan
Crater Wall
Estimated Lambert Albedo
Wavelength (nm)
c
10 km
d
V46072001
Dunes
Mound
Crater Floor
Fan
Crater Wall
Estimated Lambert Albedo
Wavelength (nm)

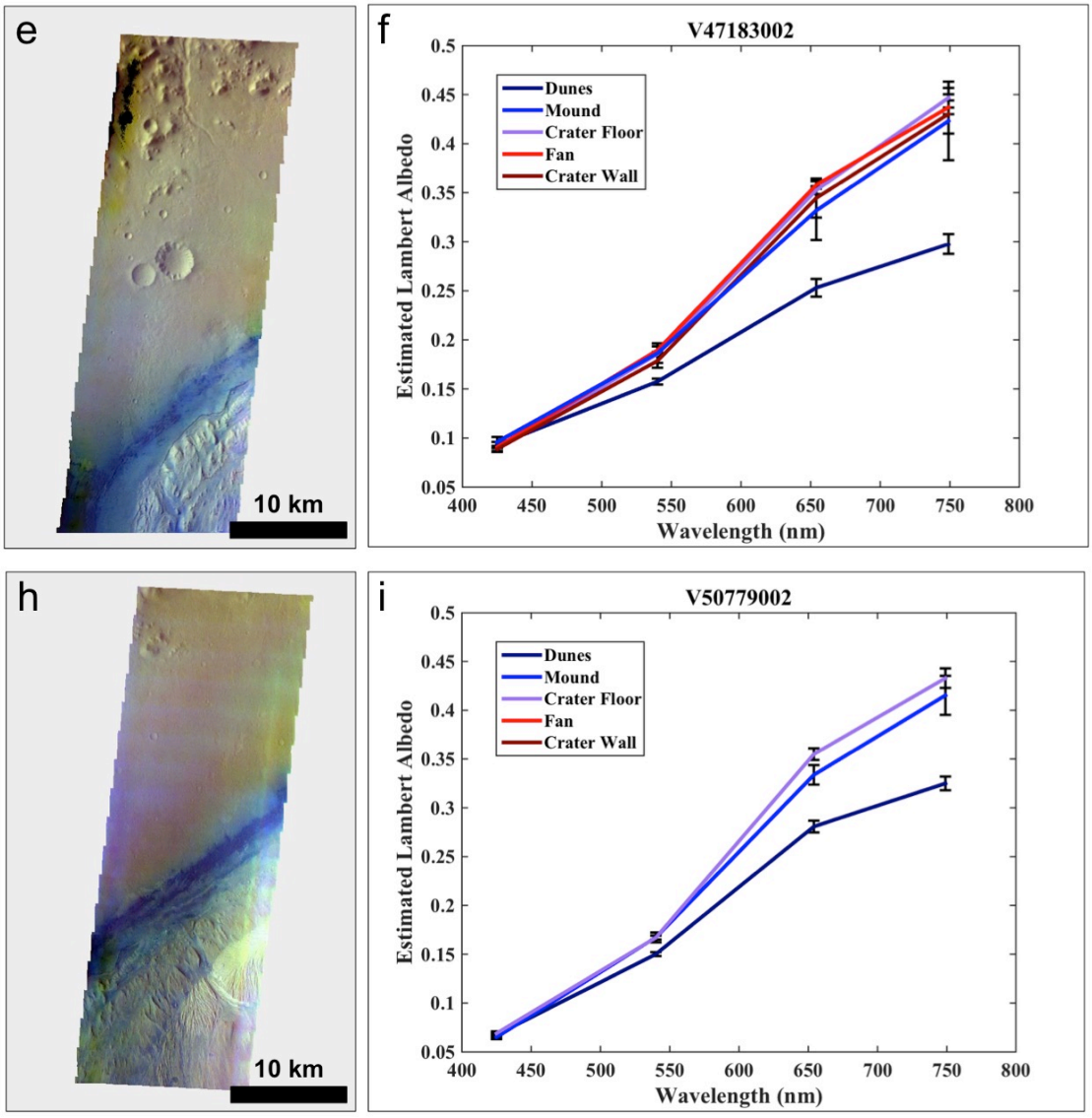
e
10 km
f
V47183002
Dunes
Mound
Crater Floor
Fan
Crater Wall
Estimated Lambert Albedo
Wavelength (nm)
h
10 km
i
V50779002
Dunes
Mound
Crater Floor
Fan
Crater Wall
Estimated Lambert Albedo
Wavelength (nm)

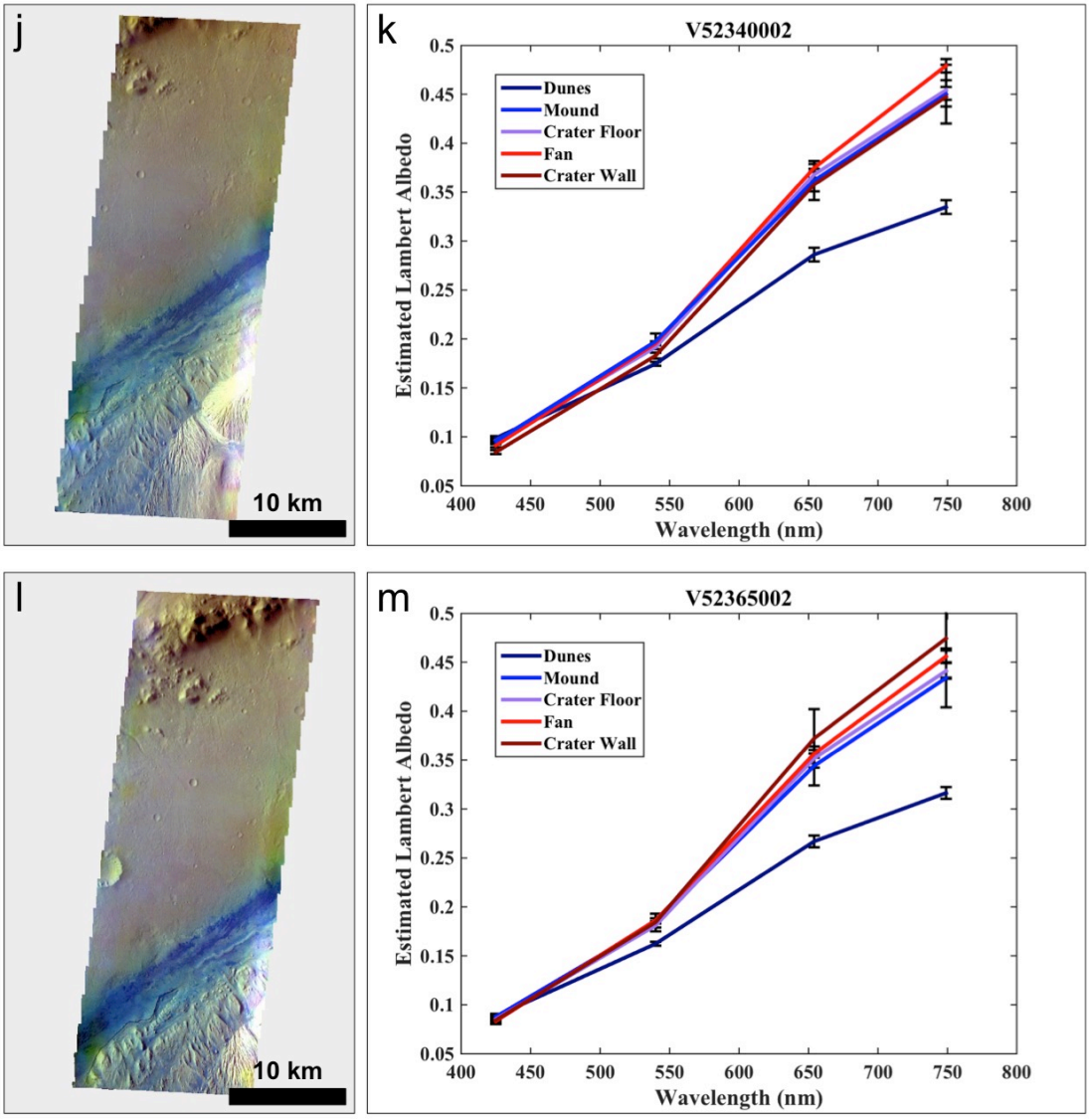
j
10 km
k
V52340002
Dunes
Mound
Crater Floor
Fan
Crater Wall
Estimated Lambert Albedo
Wavelength (nm)
l
10 km
m
V52365002
Dunes
Mound
Crater Floor
Fan
Crater Wall
Estimated Lambert Albedo
Wavelength (nm)

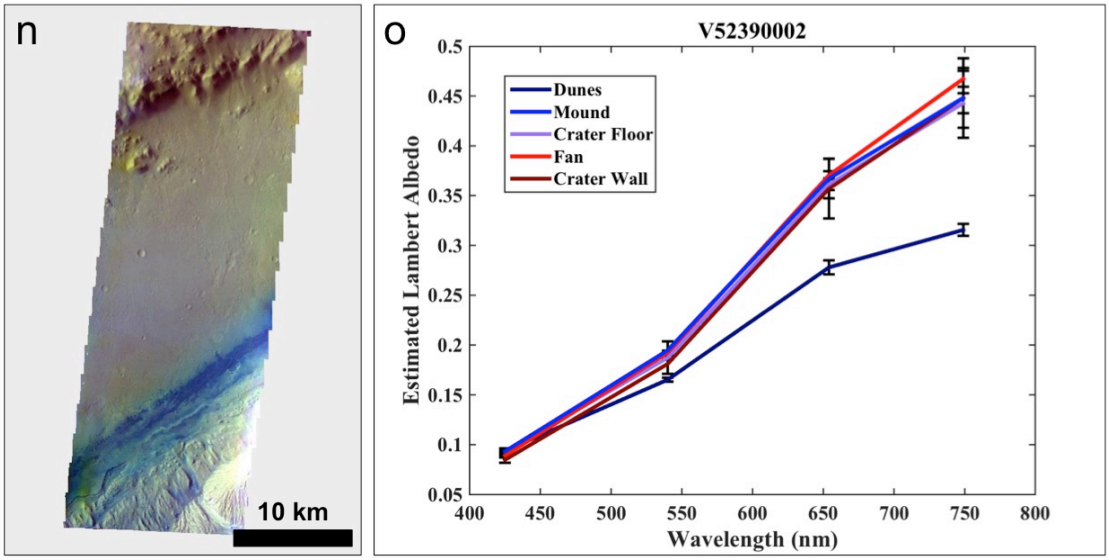

Figure B.2 THEMIS-VIS color images (V43750002, V46072001, V47183002, V50779002, V52340002, V52365002, and V52390002) over the Curiosity rover landing site and the associated four point spectra of five units (dunes, mound, crater floor, fan, and crater wall).

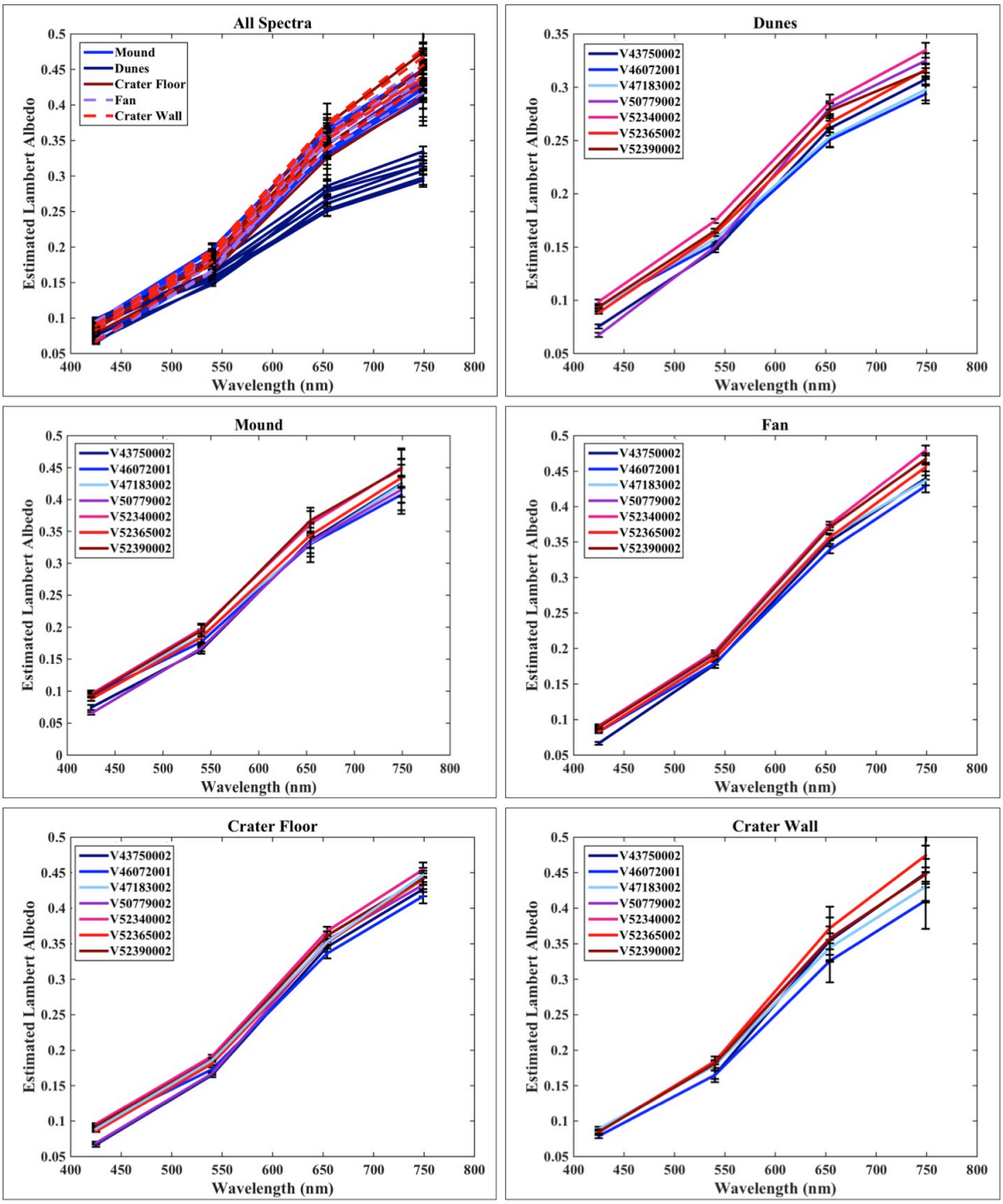

Figure B.3 The THEMIS-VIS four point spectra over the area near MSL from Figure B.2, organized by unit.

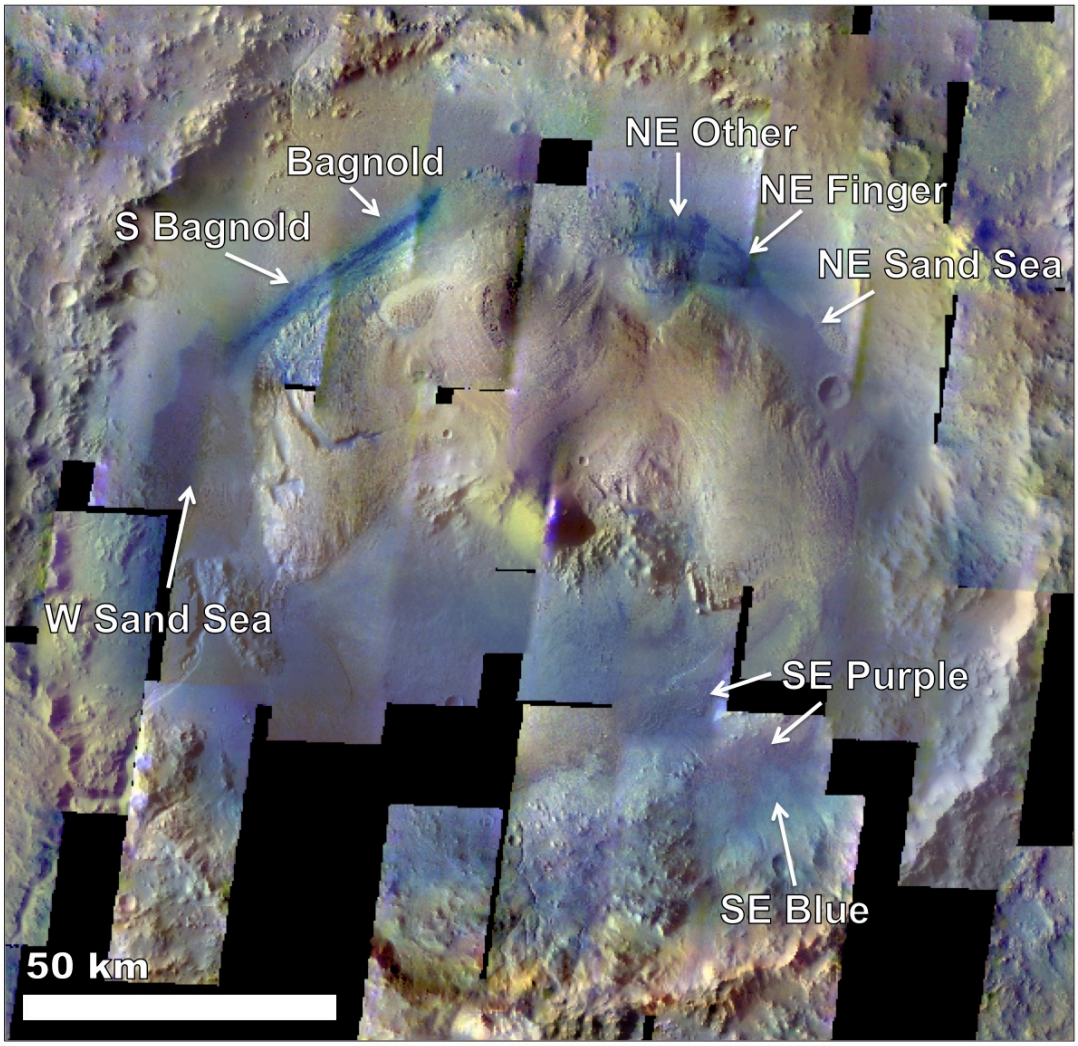

Figure B.4 THEMIS-VIS color mosaic of Gale crater showing the location of the dunes sampled in Figure B.5.

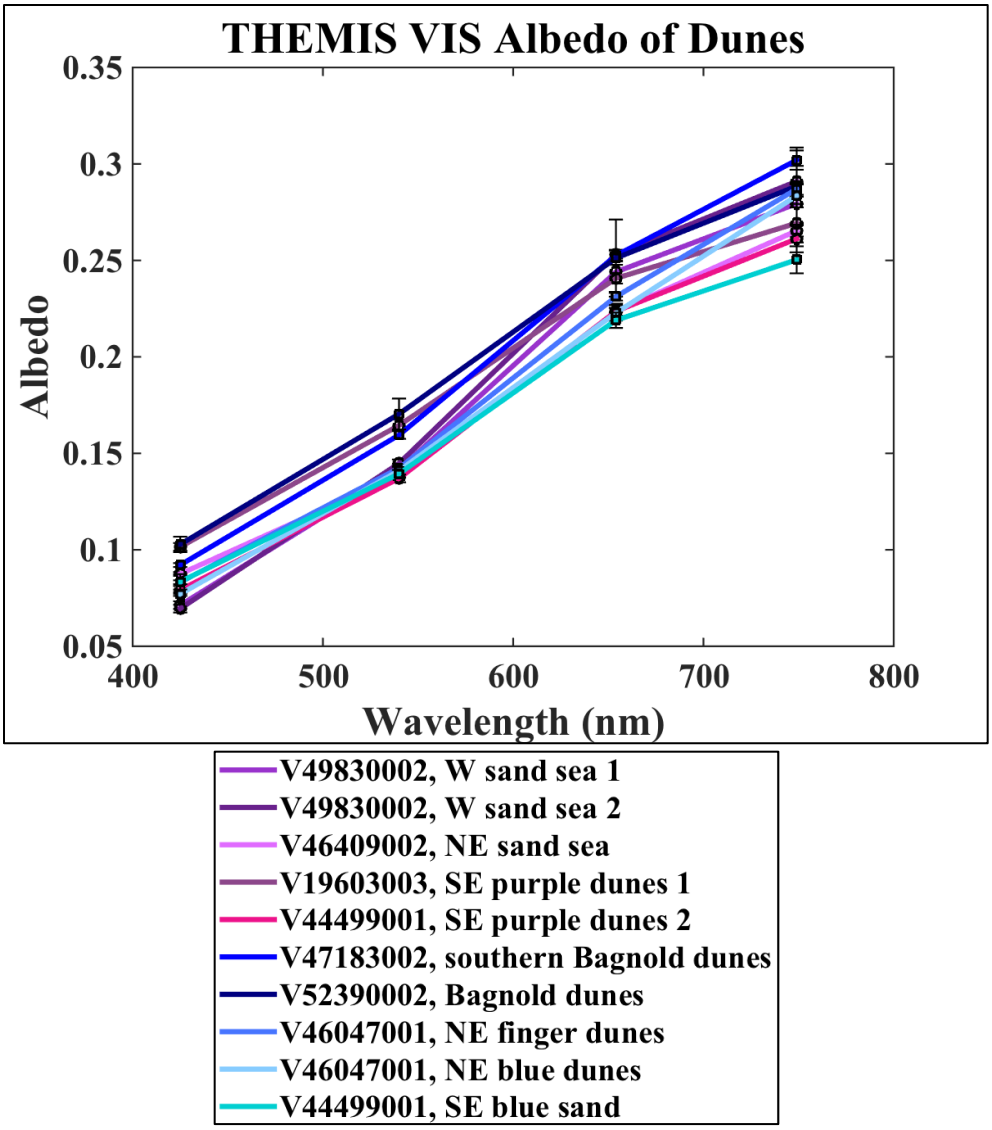

Figure B.5 THEMIS-VIS four point spectra of various dunes in Gale crater, organized by color. Visually purple dunes are plotted with purple lines and visually blue dunes are plotted with blue lines.

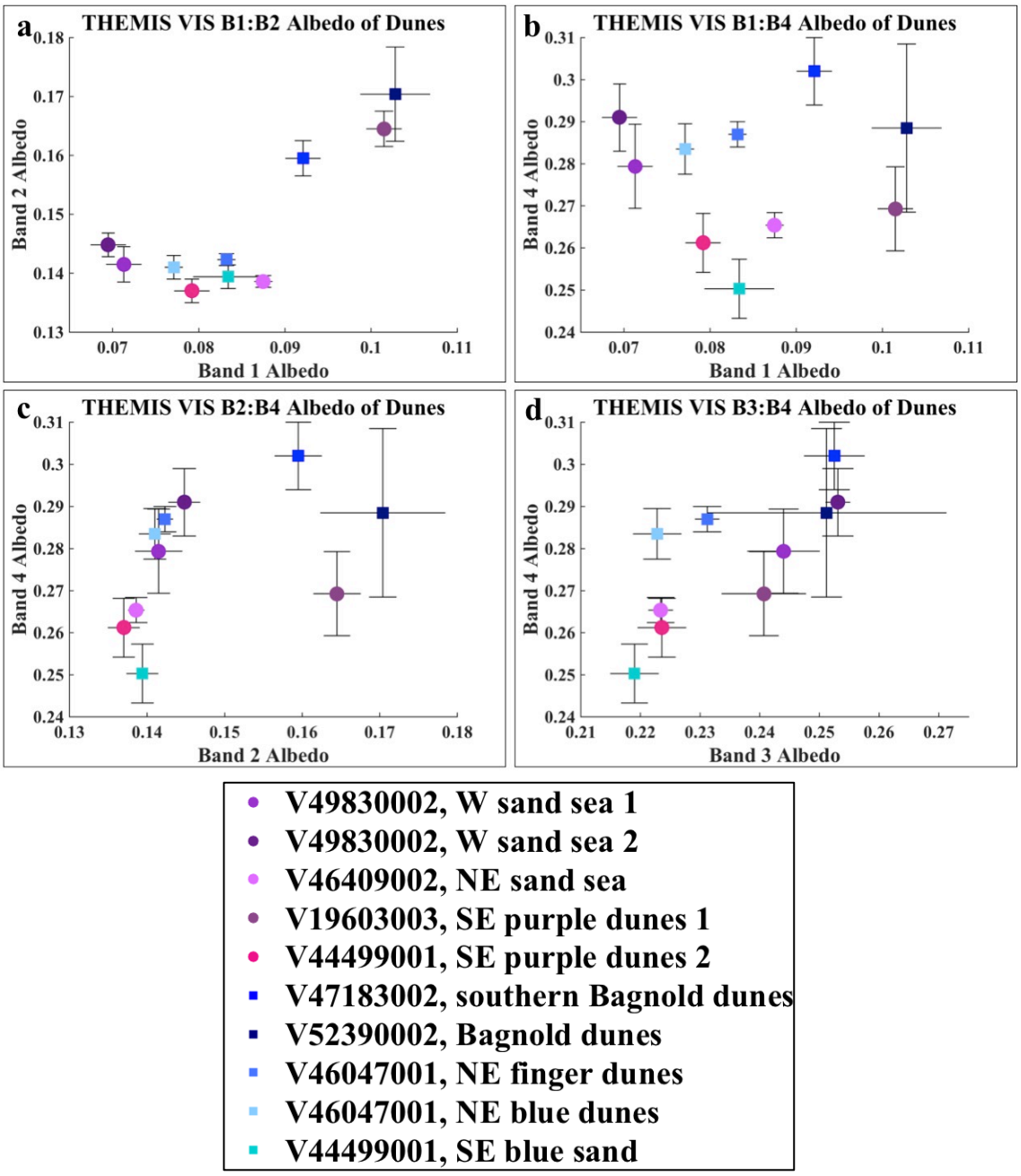

Figure B.6 THEMIS-VIS albedo of various dunes in Gale crater, organized by color. Visually purple dunes are plotted as purple circles and visually blue dunes are plotted as blue squares.

APPENDIX C

STATEMENT OF PUBLICATION COAUTHOR APPROVALS

Chapter 2 has been peer-reviewed and published in *Icarus*, volume 264, pages 331-341. Chapter 4 has been submitted for publication and is under peer review at the time of dissertation submission. Chapter 5 has been peer-reviewed and published in an *Icarus* special issue (Lunar Reconnaissance Orbiter), volume 273, pages 296-314. I, Kristen Bennett, affirm that I am the principal author and that all subsequent coauthors approve of the publication of these works.